

赤外線天文観測衛星『あかり』 による太陽系科学

Observational study of Solar system studies with AKARI infrared astronomical satellite

上野 宗孝
宇宙科学研究所

Munetaka UENO

ueno@stp.isas.jaxa.jp
Institute of Space and Astronautical Science (ISAS)
Japan Aerospace Exploration Agency (JAXA)



赤外線天文観測衛星『あかり』 による太陽系科学

Observational study of Solar system studies with AKARI infrared astronomical satellite

上野 宗孝
宇宙科学研究所

Munetaka UENO

ueno@stp.isas.jaxa.jp
Institute of Space and Astronautical Science (ISAS)
Japan Aerospace Exploration Agency (JAXA)



本日の要旨



『あかり』は2006年2月22日に打上げられ、4年弱の科学観測を行った赤外線天文観測衛星である。あかり衛星は液体ヘリウムによる冷却が維持された当初の16ヶ月弱を用いて、全天サーベイ観測(スキャン観測)を行うとともに、波長2~200umの広い波長範囲で指向観測を行った。また、冷媒である液体ヘリウムの消失後は、冷凍機による冷却のみで5umまでの波長域での撮像・分光観測を行った。

あかり衛星は、望遠鏡の運用の制約が強く、観測時間を有効に使う事を目指して、その指向観測については公募観測だけでは無く、小~大規模のプログラム観測がプロジェクトにおいて公募され評価選定後実行した。これらの中で太陽系科学に密に関連する内容として太陽系天体の観測プログラム(SOSOS)、星惑星領域の観測プログラム(AFSAS)の2課題が実行された。本講演では、あかりのサーベイ観測とこれらのプログラム観測で目指したサイエンスとその観測結果を概括する形で報告する。また、これらの結果を受けて、地球周回衛星からの太陽系天体の赤外線観測の今後についても議論する。

AKARI infrared astronomical satellite is put into orbit around the earth by M-V launching vehicle on February 22, 2006, and conducted scientific operations until February 2010. AKARI, which was originally designed for whole-sky survey mission, also carried out pointed observations at infrared wavelength (2-200um) in the early 16 months' phase, in which period the telescope and the instrument were cooled by liquid Helium (170 liter of superfluid helium). AKARI continued scientific observations only in 2-5um range for 900days, after the liquid Helium ran out.

AKARI's machine time was allocated into several legacy scientific programs as well as open time observations, to maximize its scientific outcomes, since its satellite operation has less flexibility and hard constraints. Two of the legacy program are important for solar system studies;

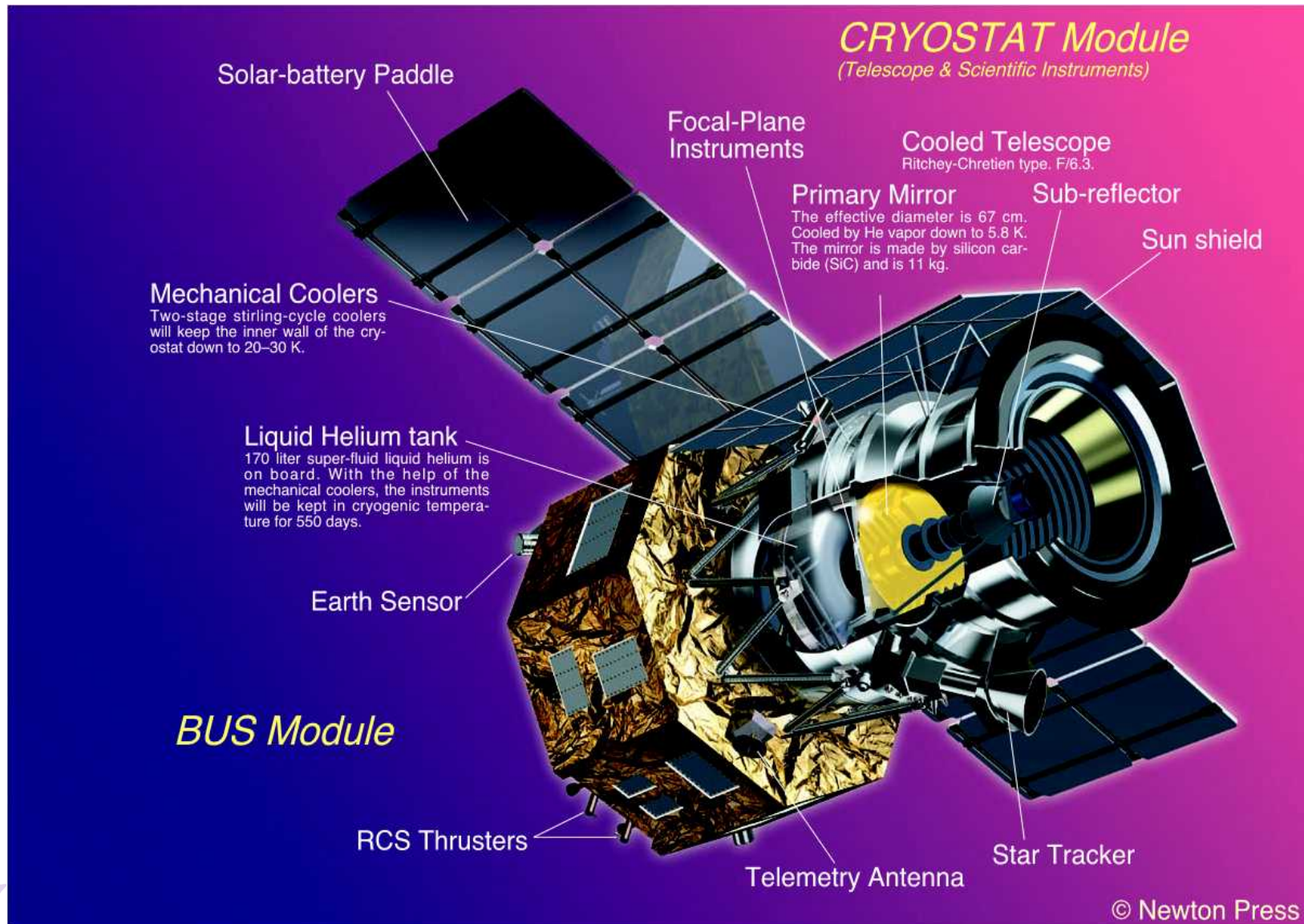
SOSOS (program on solar system studies), AFSAS (observations of star-forming regions).

This talk summarizes observational results of solar system science with AKARI mission, and will discuss the future prospect.

●キーワード(keywords): 赤外線観測、天文観測衛星、全天サーベイ観測、小惑星、彗星、惑星間塵、Tタウリ型星

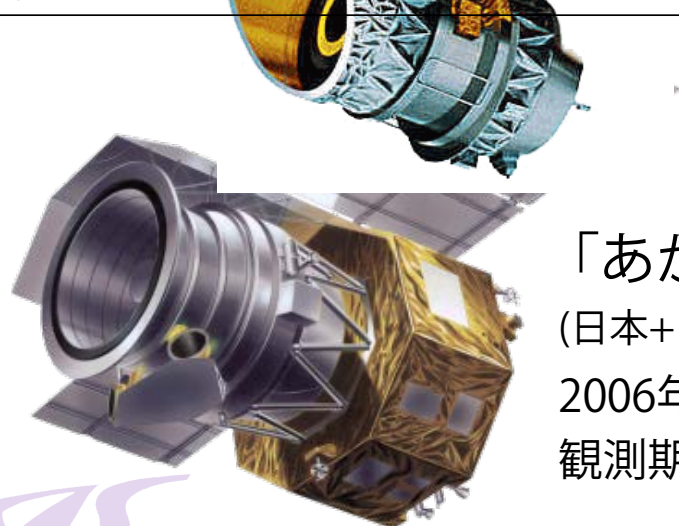
Infrared observations, Astronomical satellite, All-sky survey, Asteroid, Comet, Interplanetary dust, T-Tauri type star

AKARI "A next generation infrared sky survey" launched on February 22, 2006



3つの赤外線サーベイ衛星

	IRAS*	AKARI†	WISE‡
Size [m]	3.6 × 3.2 × 2.1	5.5 × 1.9 × 3.7	2.9 × 2.0 × 1.7
Weight [kg]	1083	952	750
Telescope	57 cm, <i>f</i> /9.56 Ritchey–Chrétien	68.5 cm, <i>f</i> /6 Ritchey–Chrétien	40 cm, <i>f</i> /3.375 Mirror complex§
Cryogen	LHe (480 ℓ)	LHe (179 ℓ) with 2-stage Stirling coolers	Solid hydrogen (15.7 kg)
Altitude of orbit	900 km	750 km	525 km
Launch [UT]	1983/01/26 02:17:00	2006/02/21 21:28:00	2009/12/14 14:09:00
End of operation [UT]	1983/11/23	2011/11/24 08:23:00	2011/02/17 20:00:00
Period of survey‡	1983/02/09–1983/11/22 287 days	2006/04/26–2007/08/26 488 days	2010/01/07–2010/08/05 211 days
Wavelengths [μm]	12, 25, 50, 100	9, 18, 65, 90, 140, 160**	3.4, 4.6, 12, 22
5σ sensitivity [mJy]	350, 330, 430, 1500*	50, 90,†† 3200, 550, 3800, 7500‡‡	0.08, 0.1, 0.85, 5.5§§
FOV [°]	4.5~5.0	~10	47
Sky coverage	> 96%	> 96%	> 99%

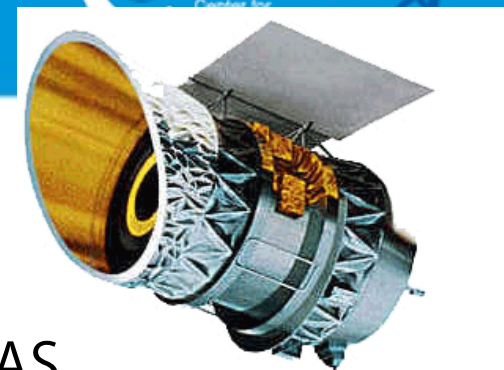


「あかり」

(日本+ヨーロッパ)

2006年打ち上げ、高度 750km

観測期間：16ヶ月

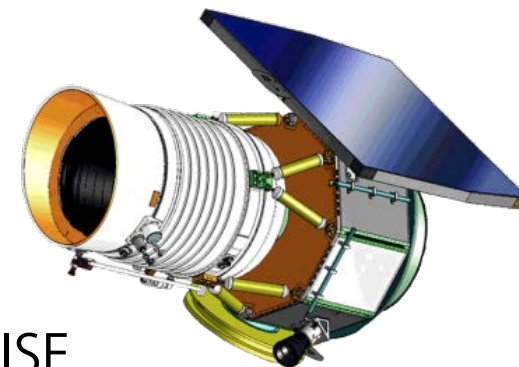


IRAS

Infrared Astronomical Satellite
(アメリカ, オランダ, イギリス)

1983年打ち上げ、高度 900km

観測期間：9ヶ月半



WISE

Wide-field Infrared Survey Explorer
(アメリカ)

2009年打ち上げ、高度 525km

観測期間：9ヶ月

白井さんの資料より

あかりで目指したサイエンス



● 星形成領域の観測

● 原始惑星系円盤におけるダストディスク消失のタイムスケール

● Molecular cloud のサーベイに基づく WTTS の頻度分布(以下は正しいの?)

● PS phase $\sim 10^5$ year, CTTS phase $\sim 10^6$ year, WTTS phase $\sim 10^7$ year

● 原始惑星系円盤における、ダストの進化

● 多様な星形成プロセスの観測的研究

● 太陽系天体

● 惑星間塵

● 起源, 空間分布・構造, 軌道進化, Composition, COBE-DIRBE モデルからの脱却

● 小惑星

● 含水鉱物という切り口で、小惑星を系統的に調べる

● 彗星

● ダスト組成、Crystalline silicate はどこから?



個人的な問題意識



● 原始惑星系円盤におけるダストディスク消失のタイムスケール

● 赤外線で見えている原始惑星系円盤のダストは primordial?

● Photon/stellar wind driven の Poynting-Robertson effect は大きいはず

● 特に初期の低質量星は stellar wind が桁違いに大きい

● 何かに守られている or 再供給されないとダスト円盤は見えないだろう

● 原始惑星系円盤の分光観測で、大きな粒子では見えない feature が見える事から、小さなサイズのダストが支配的である事は確かである：上記の事実と相反する

● 但し、大きな粒子の存在を否定する物では無い：但し、mass estimation には配慮が要

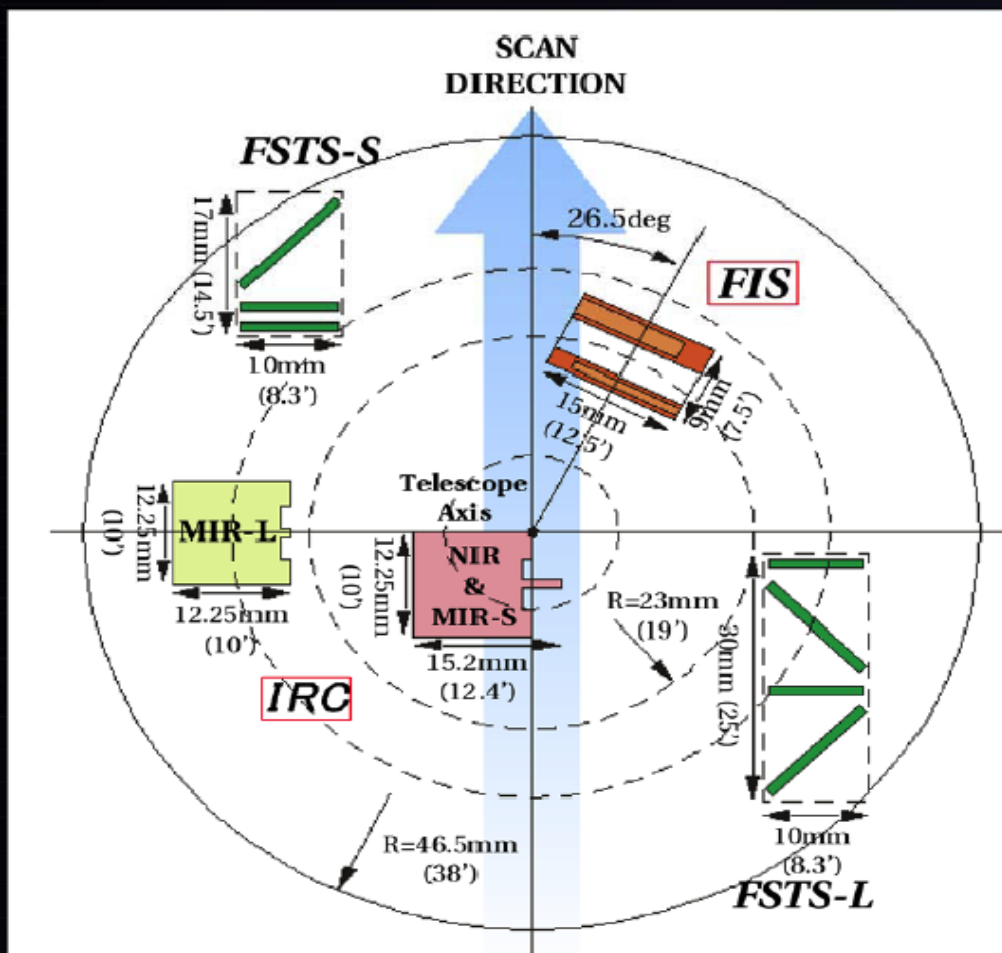
● 我々の太陽系の黄道光は、当然ながら primordial では無く、太陽系で見ると短期的に時間積分した供給源の賜物である

● このため、現在の起源比(彗星：小惑星)がユニバーサルである必要は無い

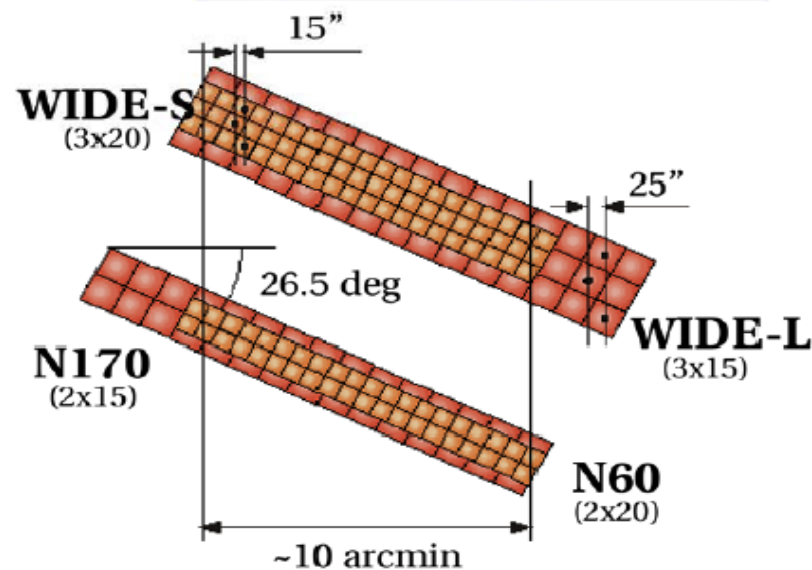
● ただし、太陽系内でのダストの軌道進化は、十分には理解されていない

● その分布も、ユニフォームな成分の理解が十分であるかどうかは誰も知らない

Focal Plane Configuration



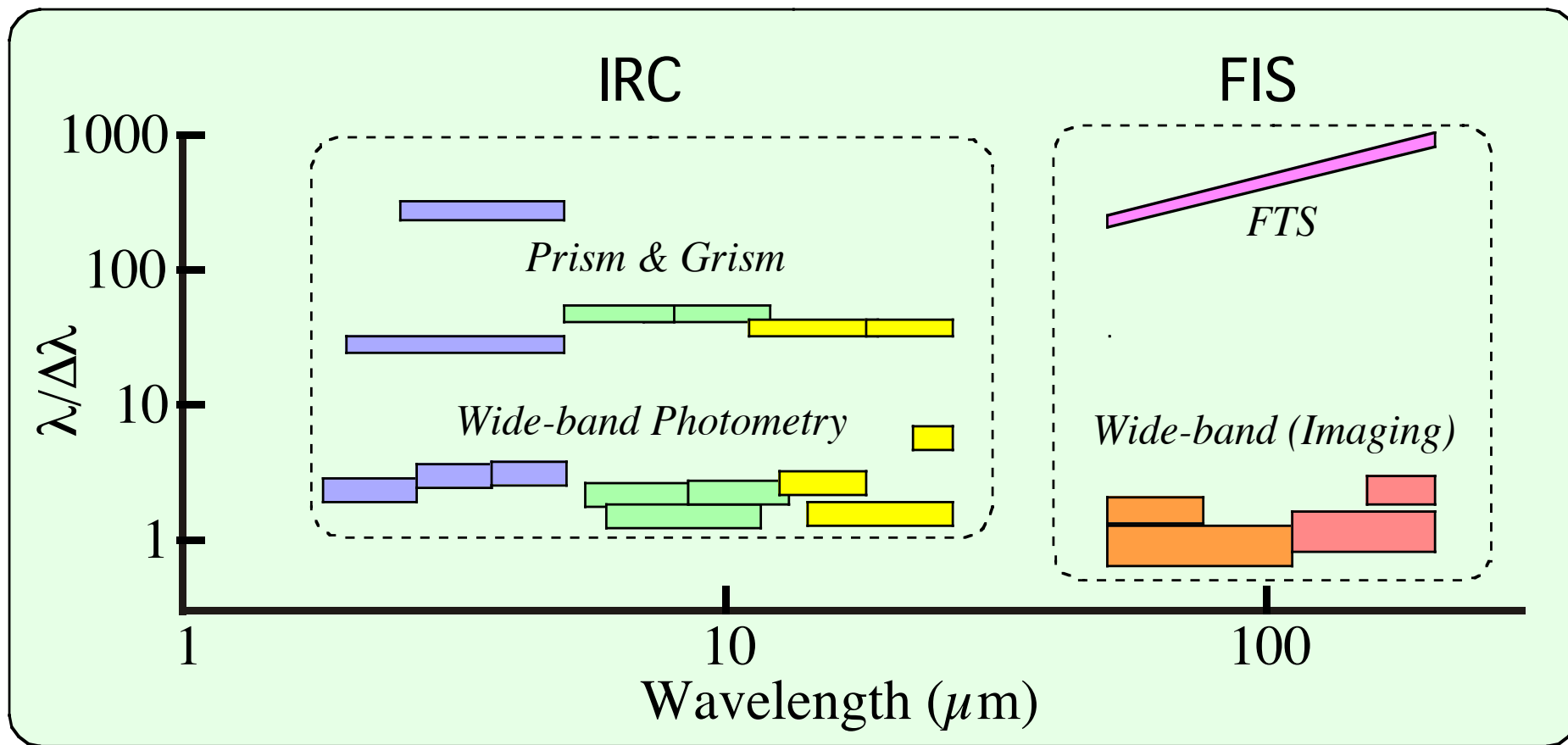
Focal Plane Configuration



- 50" x 50" / pixel
- 30" x 30" / pixel

FIS Detector Configuration

AKARI/ASTRO-F Spectral coverage



Survey coverage 9 18 65 90 140 160 (micron)
 Pixel size (arcsec) 4.8 4.8 30 30 50 50
 + Imaging (13 bands in 2 - 170 micron) + Spectroscopy

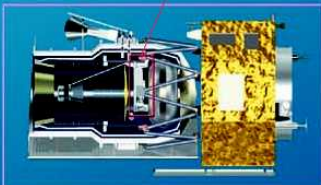


あかり の観測装置

ASTRO-F Focal-Plane Instruments

FIS (Far-Infrared Surveyor)

FPI in the cryostat



Fourier Transform Spectrometer (FTS)
Mirror driving mechanism

Rooftop mirror

FTS beam splitter

Filter wheel

Scanning mode and FTS mode are switched by rotating this wheel.



Long-Wavelength (LW) detector array

15x5 pixels array of stressed Ge:Ga detector elements. The detectors and the cryogenic readout circuits (CRE) will work at 1.8 K. The detectors cover the wavelength range of 110–200 μm .

Short-Wavelength (SW) detector array

20x5 pixels array of Ge:Ga. The detector elements and the CREs are in the monolithic structure. The detectors observe in the wavelength of 50–110 μm .



IRC-MIR-S

The camera observes in the mid-IR wavelengths (5–13 μm) with a spatial resolution of about 5 arcsec and field of view of 10 arcmin square.

IRC-NIR

The camera observes in the near-IR wavelengths (2–5 μm) with a spatial resolution of about 3 arcsec and field of view of 10 arcmin square.

Lenses

Made of Silicon and Germanium.

Detector Array

InSb 512x412 pixels for NIR camera.
Si:As 256x256 pixels for MIR cameras.

Light from the telescope



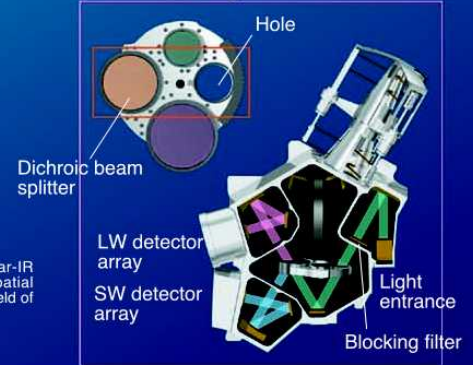
Filter wheel

Three broadband filters, two dispersion elements, and a blind mask are switched.

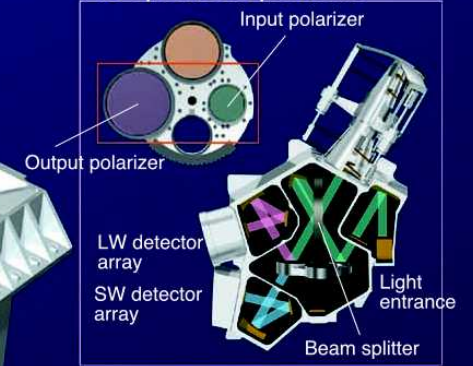
IRC-MIR-L

The camera observes in the mid-IR wavelengths (12–26 μm) with a spatial resolution of about 5 arcsec and field of view of 10 arcmin square.

FIS Scanning mode

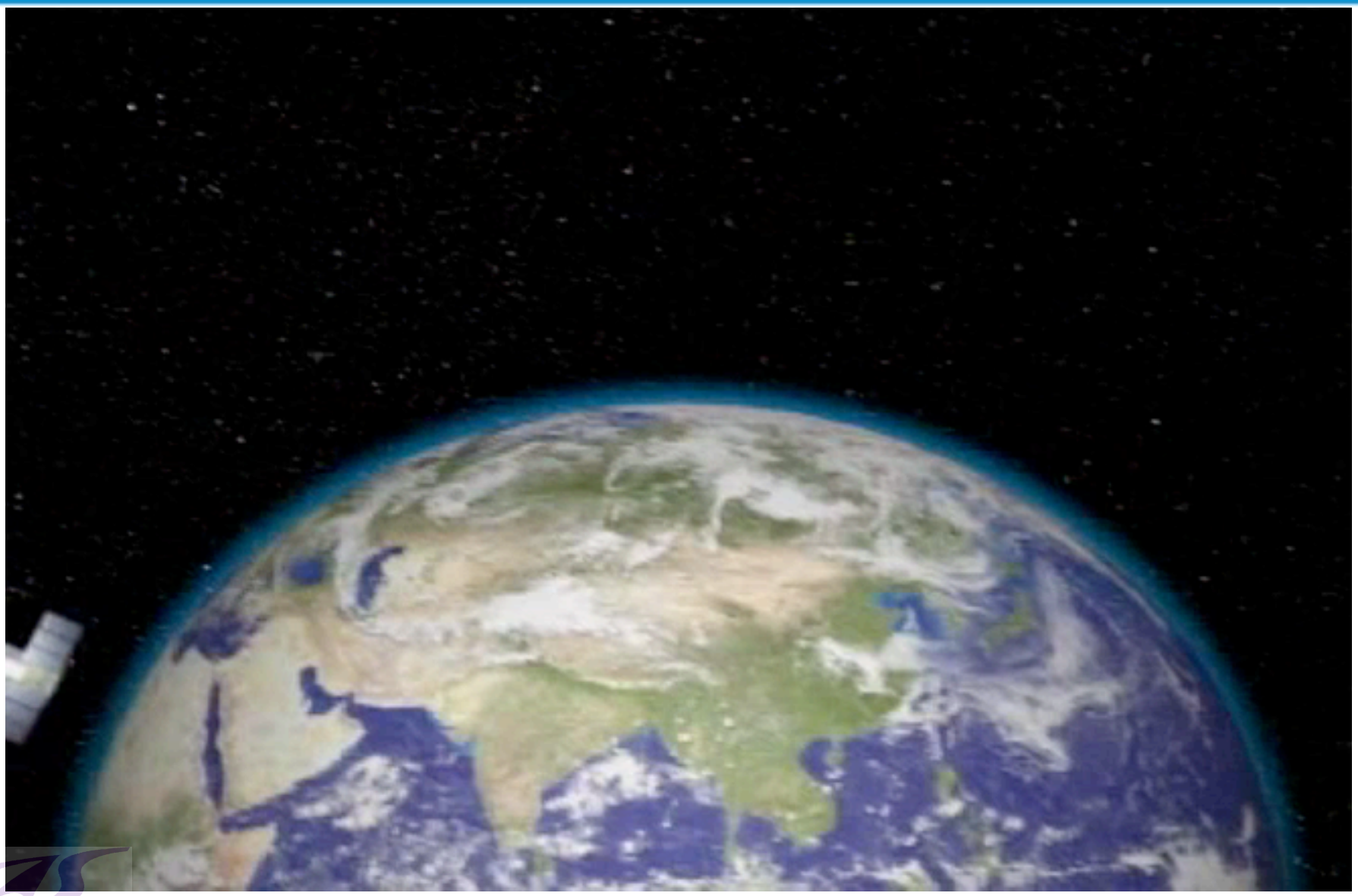


FIS Spectroscopic mode

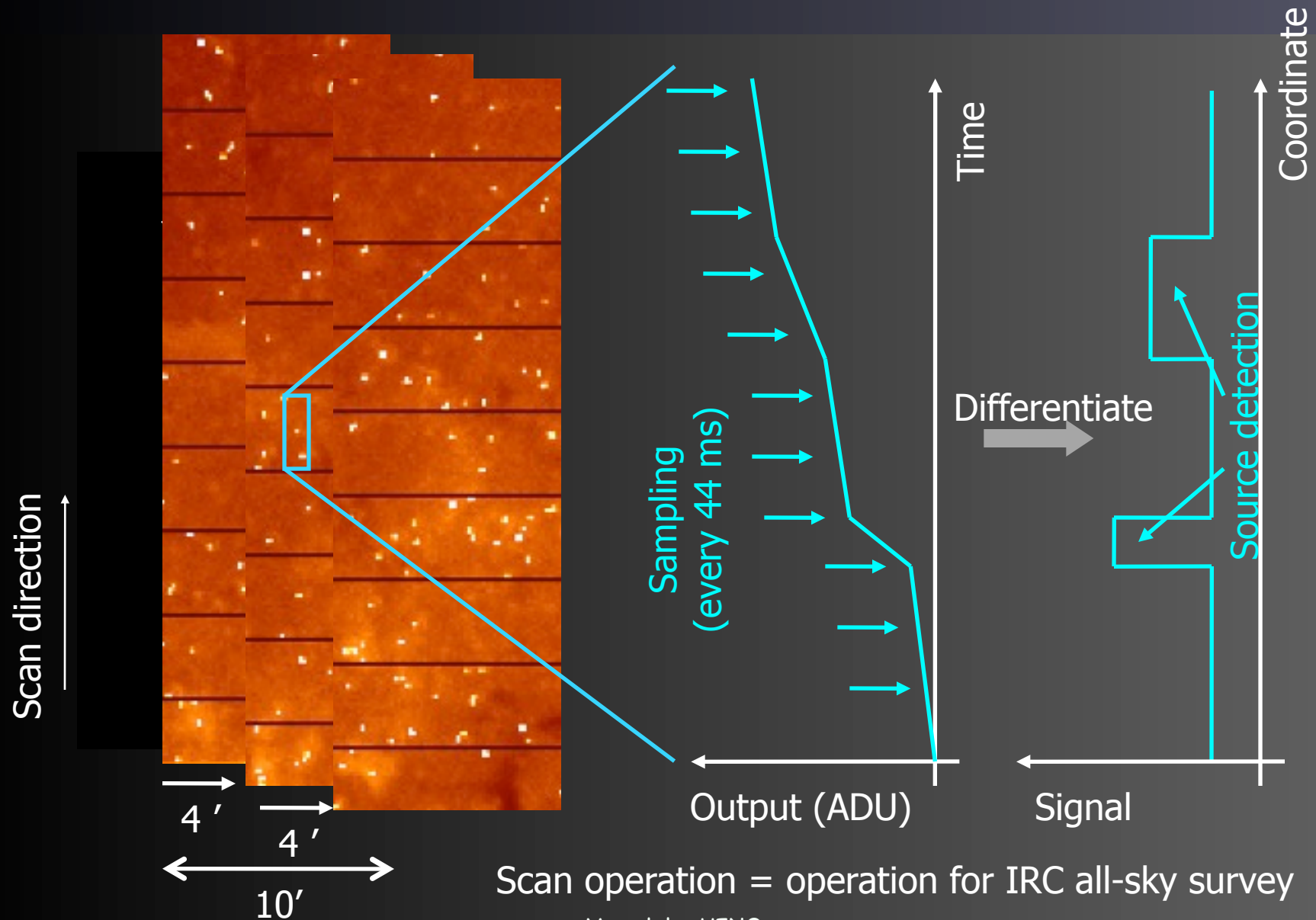


IRC (Near- & Mid-Infrared Cameras/Spectrometers)

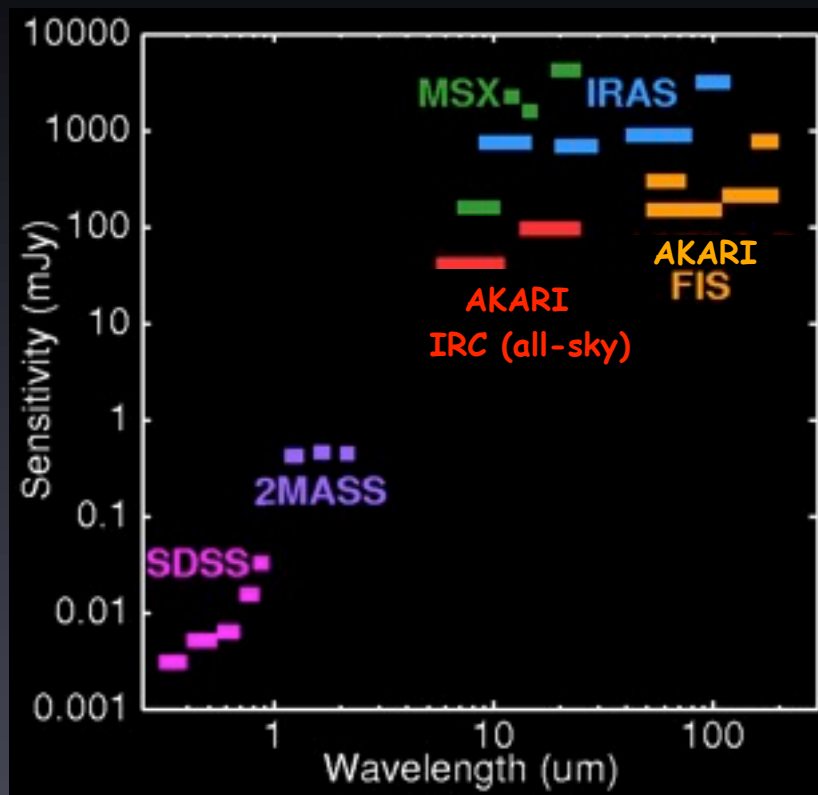
あかり による観測



Seconds, Hours, and years confirmation

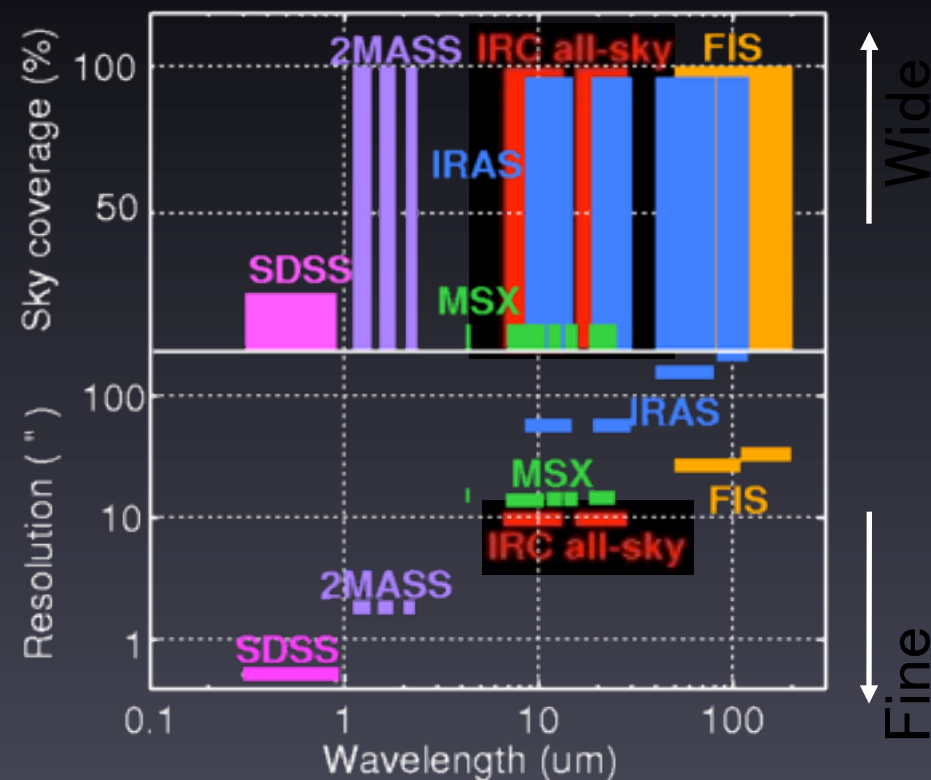


Sensitivities, Spatial resolution, Sky coverage



Sensitivity for point sources

⇒ One order of magnitude deeper than IRAS survey

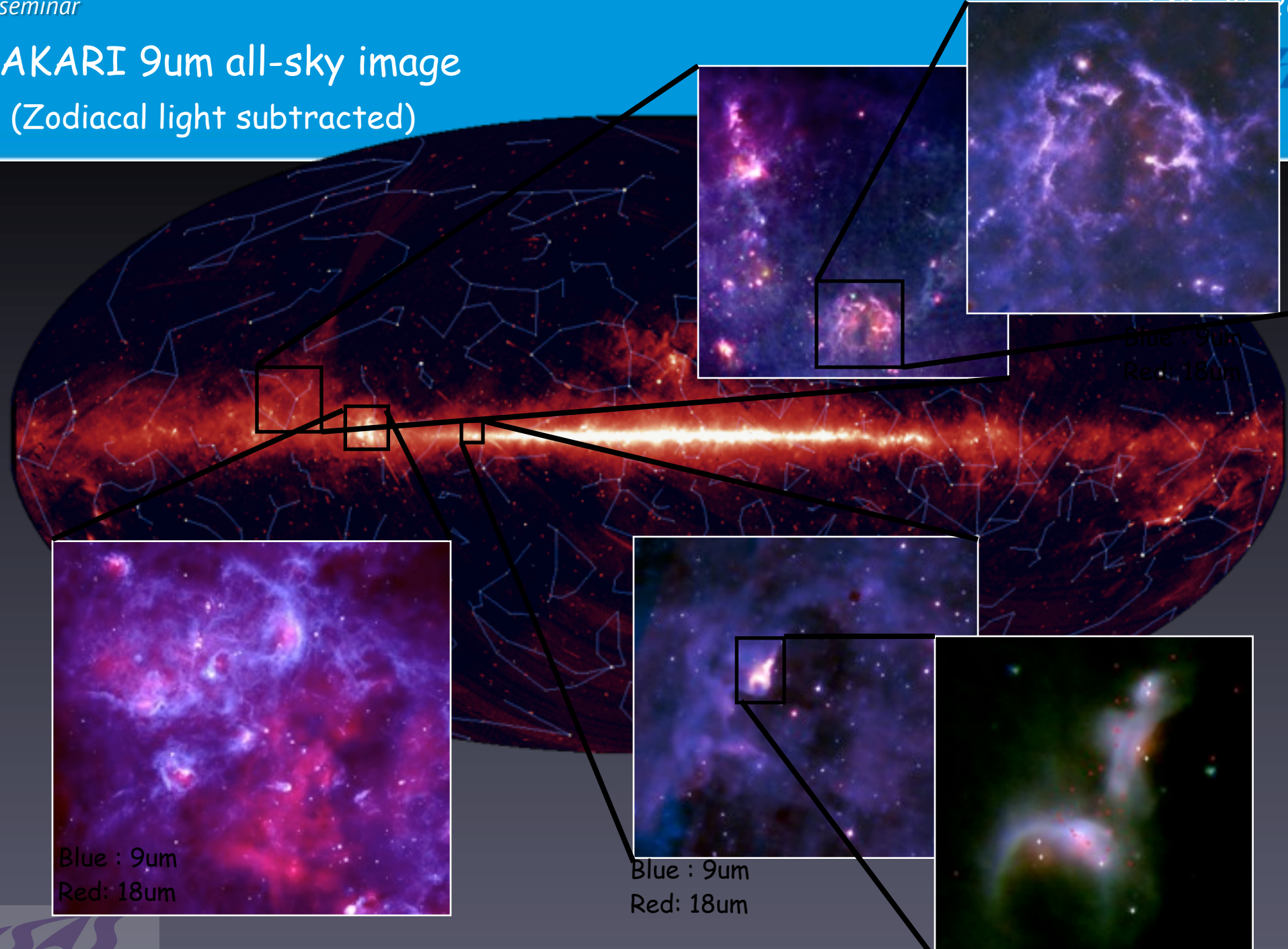


(Top) Sky coverage

(Bottom) Spatial resolution

⇒ One order of magnitude finer than IRAS survey

AKARI 9um all-sky image (Zodiacal light subtracted)



Blue : 9um
Red : 18um

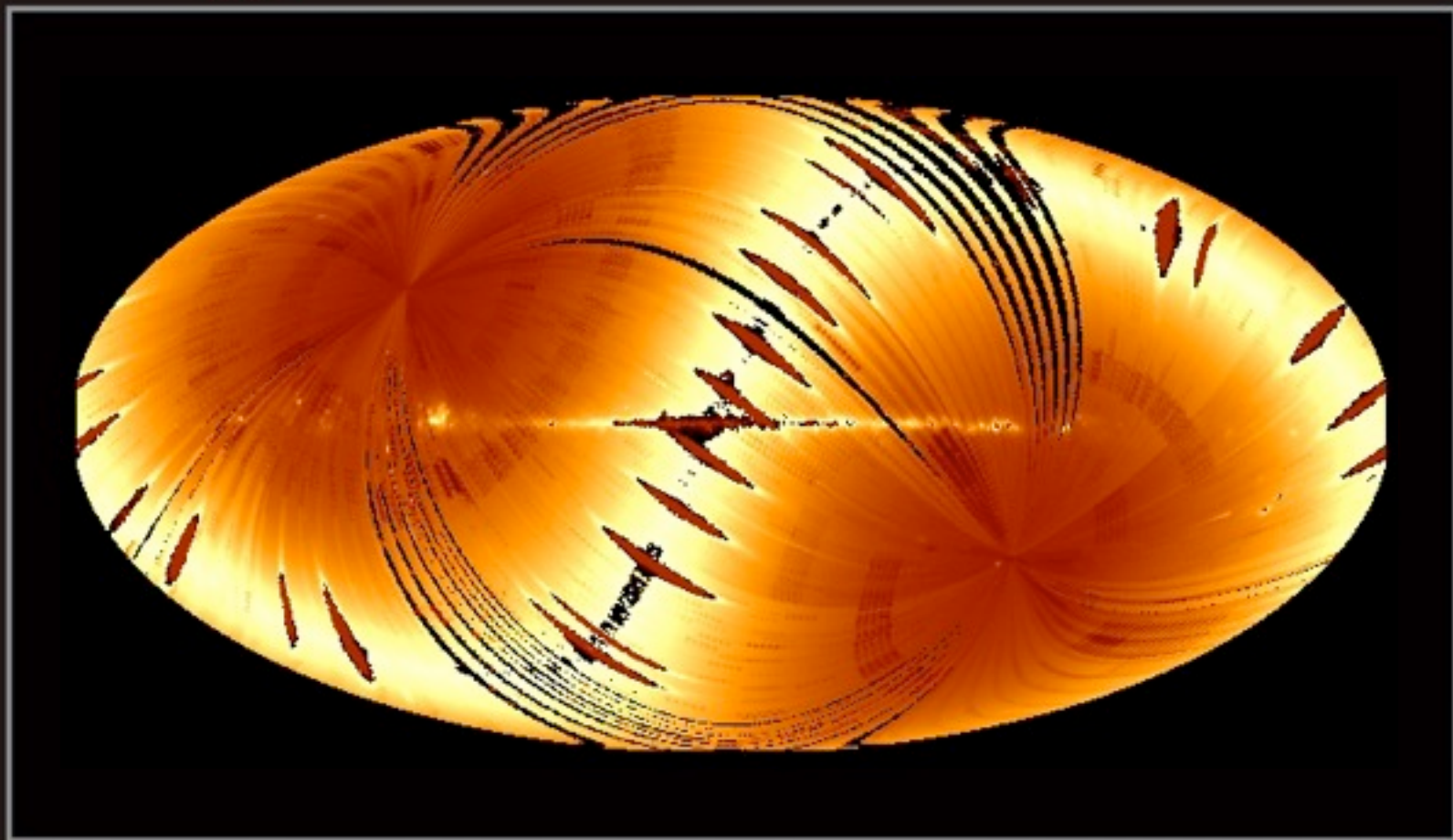
Blue : 9um
Red : 18um

Blue : 9um
Red : 18um





「あかり」による中間赤外線全天画像

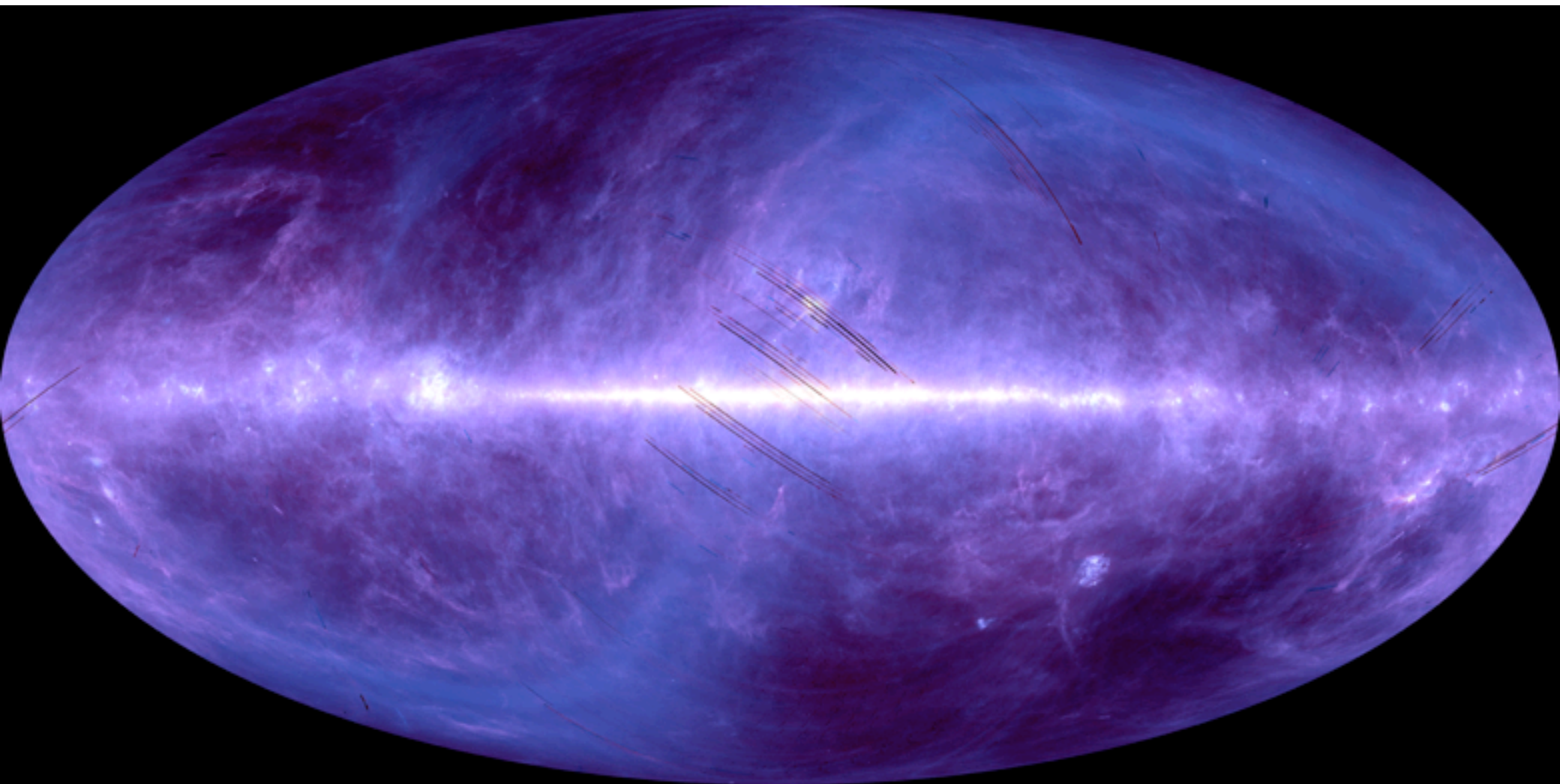


「あかり」近・中間赤外線カメラ（観測波長 $9\mu\text{m}$ ）



2007年7月11日

ALL Sky Map (AKARI/FIS)



Number of Refereed Papers



Satellite	Objective	Start of Operation	End of Operation	Counting Period	Number
AKATSUKI	Venus Atmospheric Obs.	2010	operating	2011-2012	8
KAGUYA	Lunar Exploration	2007	2009	2008-2012	190
HINODE	Solar Obs.	2006	operating	2007-2012	844
AKARI	Infrared Astronomical Obs.	2006	2011	2007-2012	222
SUZAKU	X-ray Astronomical Obs.	2005	operating	2006-2012	681
HAYABUSA	Asteroid Sample Return	2003	2010	2004-2012	129
NOZOMI	Mars Scientific Obs.	1998	2003	1999-2012	26
HALCA	Space VLBI	1997	2005	1998-2012	44
ASCA	X-ray Astronomical Obs.	1993	2002	1994-2012	2287
GEOTAIL	Geo-Magnetospheric Obs.	1992	operating	1993-2012	1236
YOHKOH	Solar Obs.	1991	2000	1992-2012	1089
<reference>					
Subaru Telescope	The Ground based optical&infrared Observatory	1999	operating	2000-2012	1031

星形成領域の観測



● 星形成領域の観測

● 原始惑星系円盤におけるダストディスク消失のタイムスケール

- Molecular cloud のサーベイに基づく WTTS の頻度分布(以下は正しいの?)
 - PS phase $\sim 10^5$ year, CTTS phase $\sim 10^6$ year, WTTS phase $\sim 10^7$ year
- ある星形成領域を、WTTS を検出できる深さで complete にサーベイする
 - 星形成レートが長期的に大きく変わらないと仮定すると、頻度分布から phase の duration を求められる
- 赤外線波長での WTTS のサーベイが行われてきていなかった

● 原始惑星系円盤における、ダストの進化

- 円盤の分光学的観測
- 多様な星形成プロセスの観測的研究
 - 星形成の場のアトラス



星惑星領域の観測プログラム(AFSAS)



PI: Munetaka UENO (Univ. Tokyo)

Akiko KAWAMURA (Nagoya Univ.)

Yoshimi KITAMURA (ISAS) Motohide TAMURA, Ryo KANDORI (NAOJ)

Satoshi R. Takita (TITECH), Hirokazu KATAZA (ISAS),

Yoshiko OKAMOTO (Ibaragi Univ.)

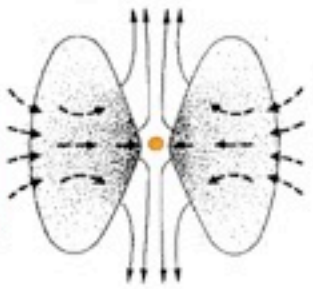
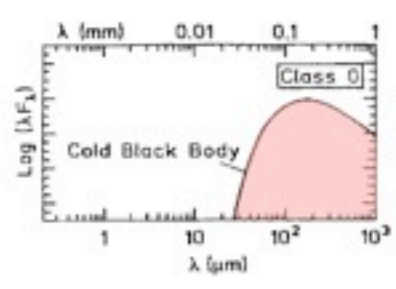
Misato FUKAGAWA, Toshikazu Ohnishi (Nagoya Univ.),

Mitsuhiko HONDA (Kanagawa Univ.)

Yuri AIKAWA (Kobe Univ.), Viktor L TOTTH(ELTE), Glenn White (Open Univ.)

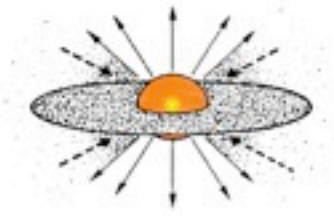
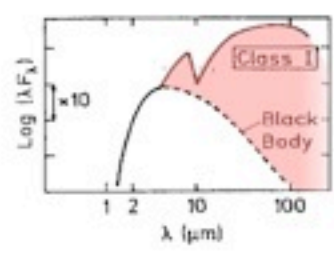
(所属は当時)





Class 0
10⁴ yr

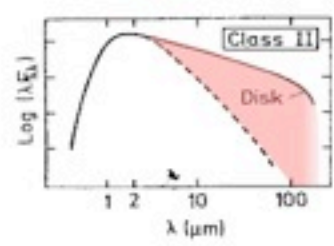
Central Star
(M ~ 1 M_⊙)
~0.5 M_⊙
Main Accretion Phase



Class I
10⁵ yr

Late Accretion Phase

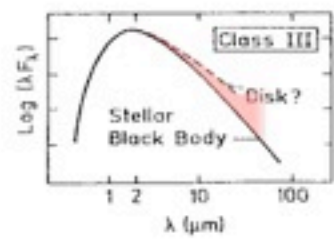
Disk



Class II
10⁶ yr

Classical T Tau Stars

Protoplanetary Disk
M_{disk} ~ 0.1 M_⊙, ~200 AU
Disk dispersal starts
Still Optically Thick
M_{disk} ~ 0.01 M_⊙
Planetesimals
2nd-Generation Dust



Class III
10⁷ yr

Weak-line T Tau Stars
End of Hayashi-Phase

Protoplanets
Optically Thin
M_{disk} ~ 0.001 M_⊙

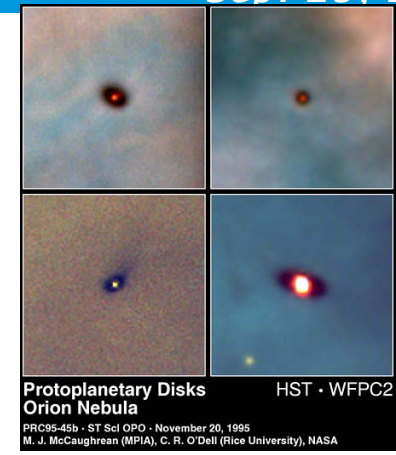
Disk dispersal completed



10⁸ yr

Main Sequence Stars

Planets & Kuiper Belt



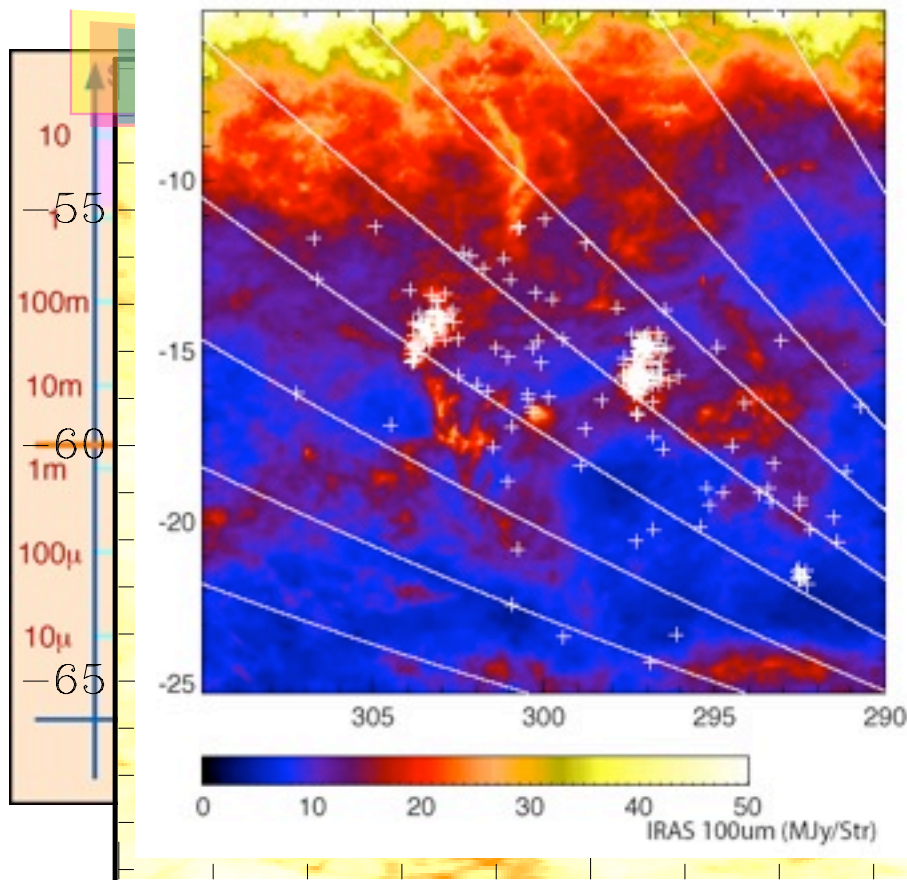
Chamaeleon survey



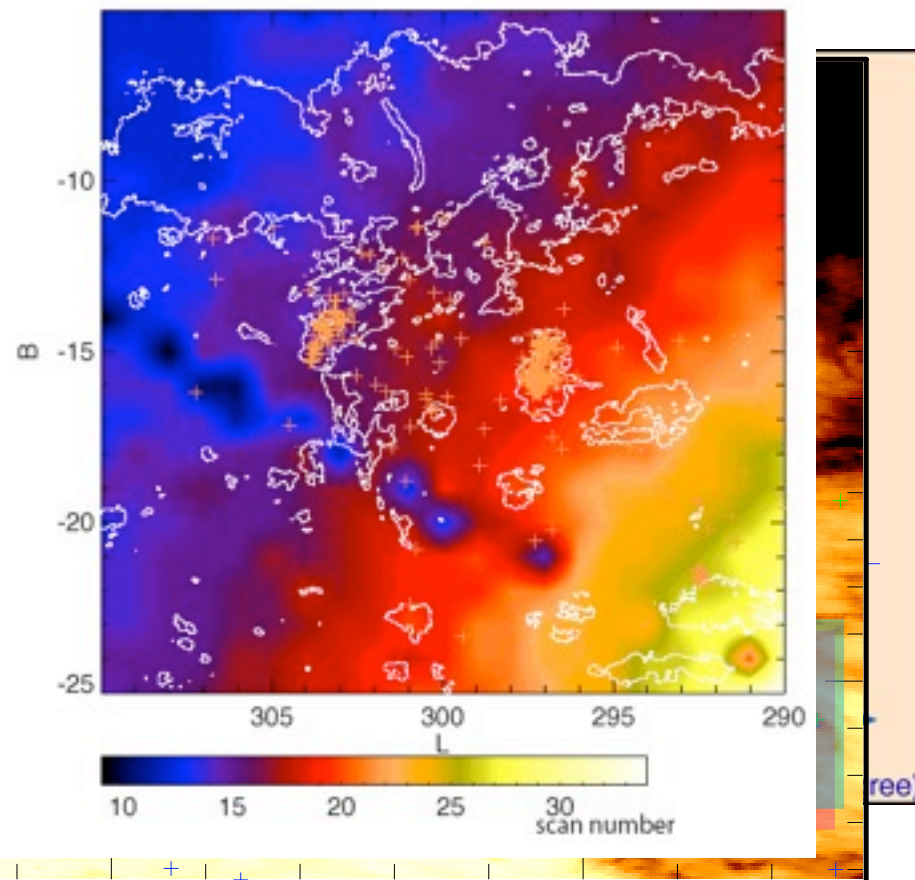
30"/sec scan

Chamaeleon (100um) in Ecliptic Coordinates

IRAS 100um & T Tau stars
Ecliptic Longitude



Visibility & T Tau stars
IRAS 100um (contour; 5, 15, 25, MJy/Str)



FIS

30"/sec scan

-90

-100

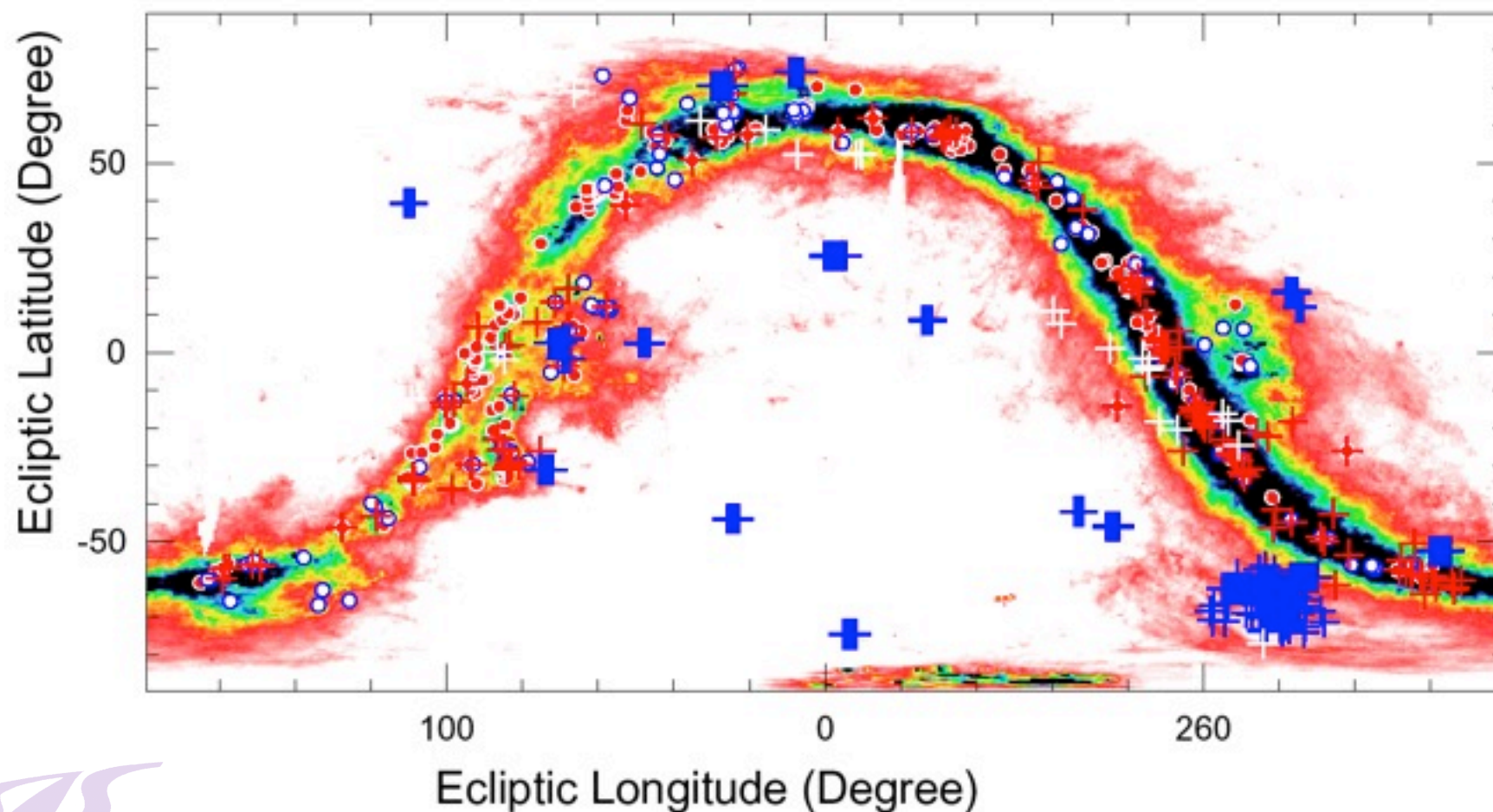
-110

-120

Observations of Star forming regions

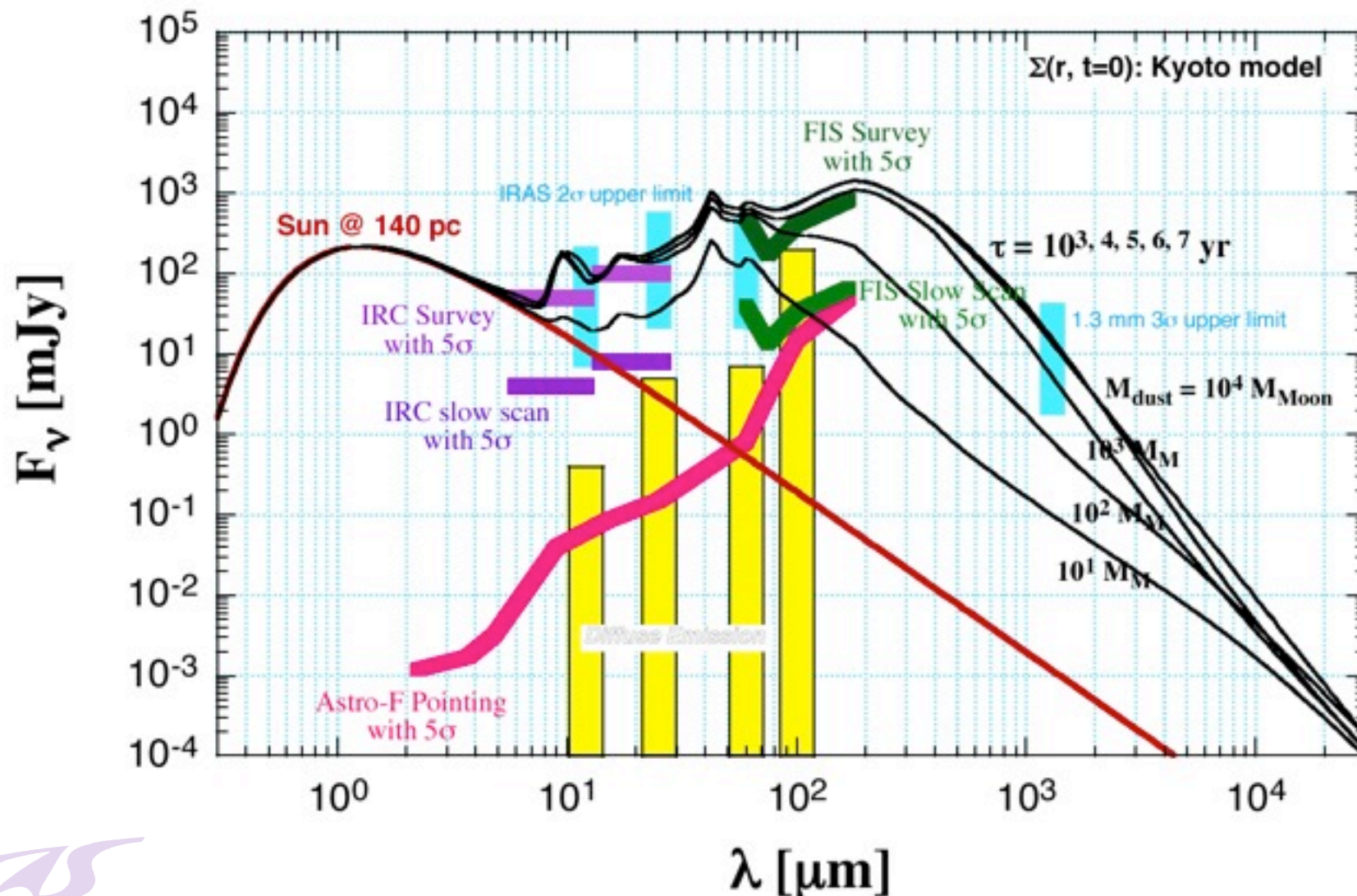
- + Cha & cloud survey
- o atlas
- + TTSS
- + star count (cross in white)

ASTRO-F SF MP target



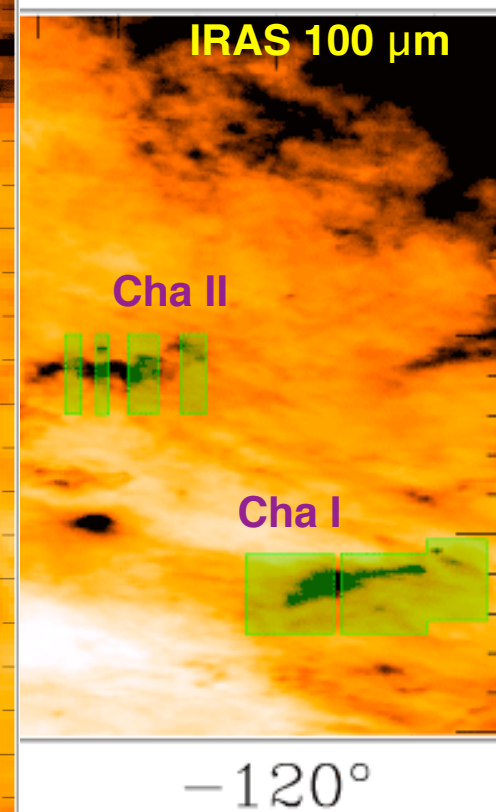
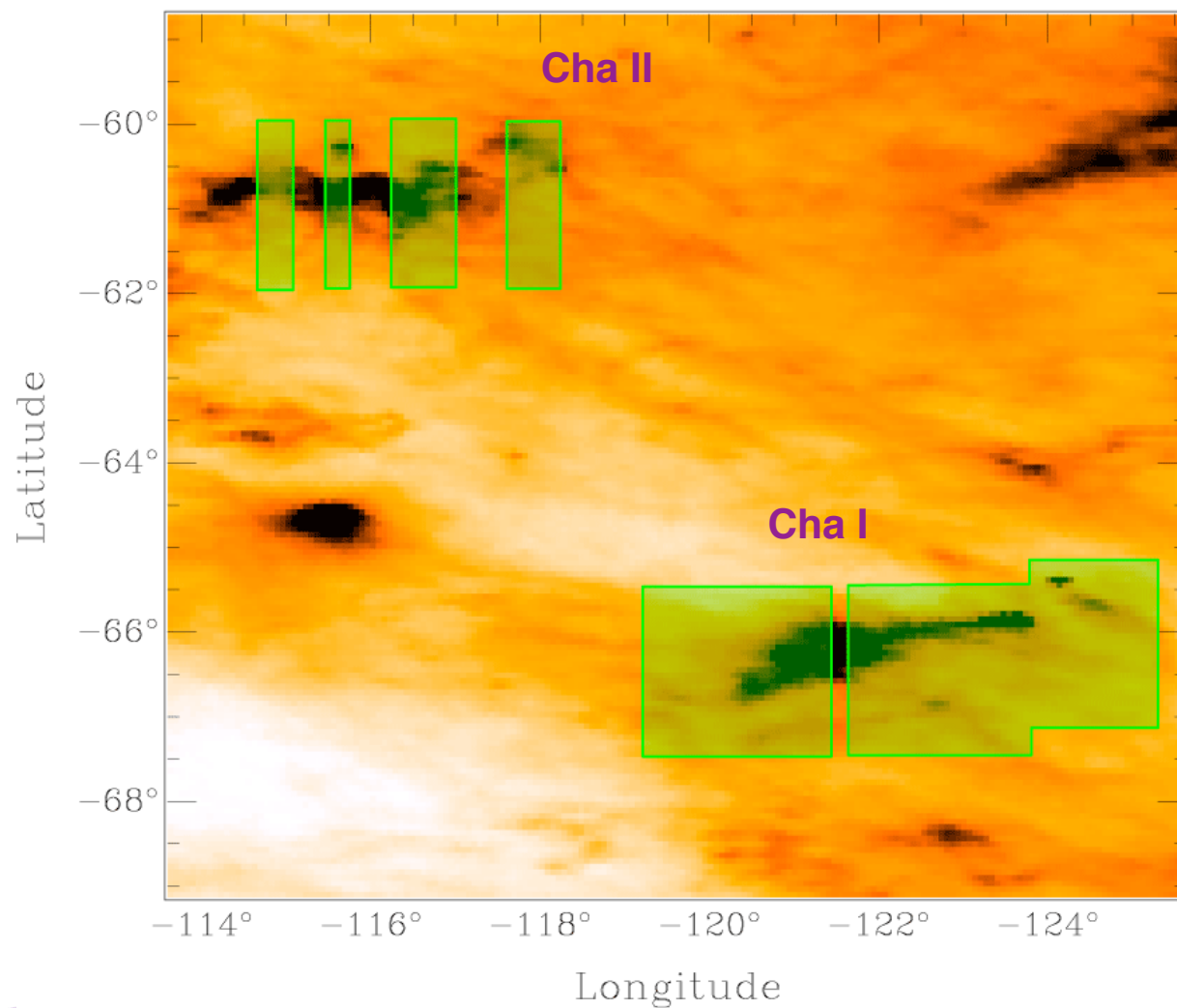
Detection limits of the survey

SED of a WTTS disk with 130 AU radius



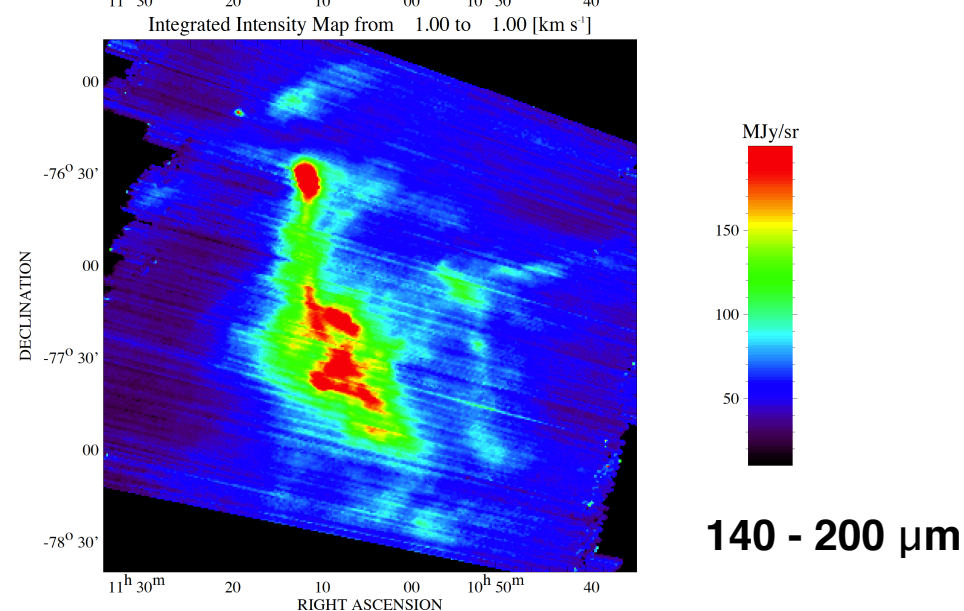
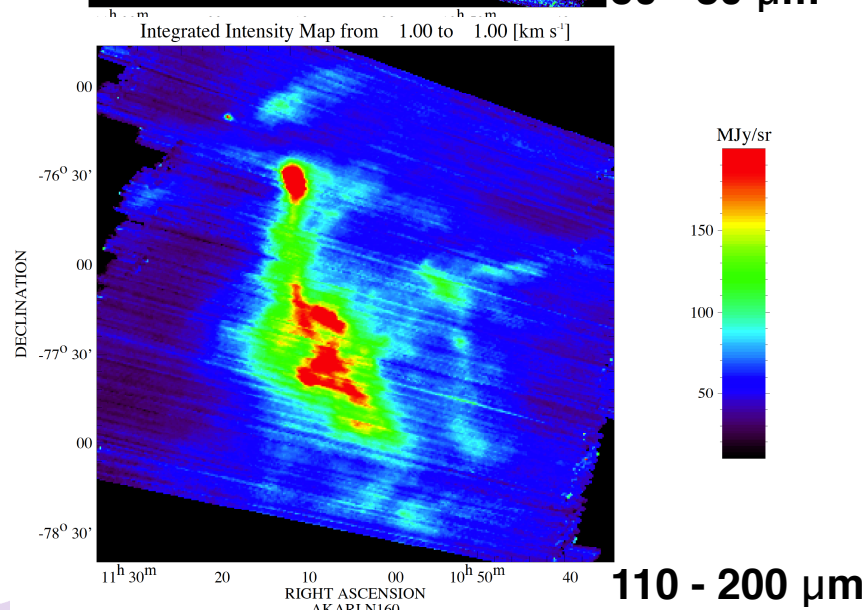
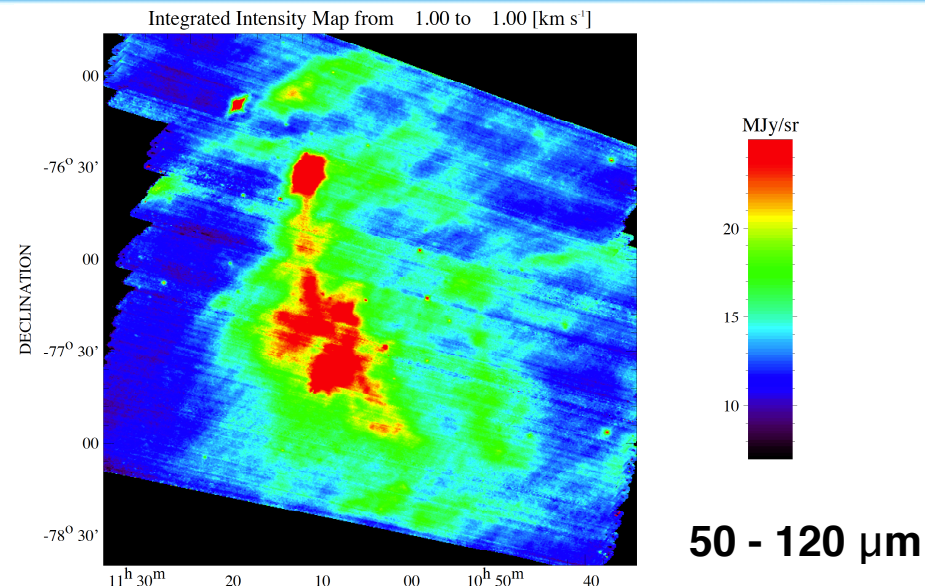
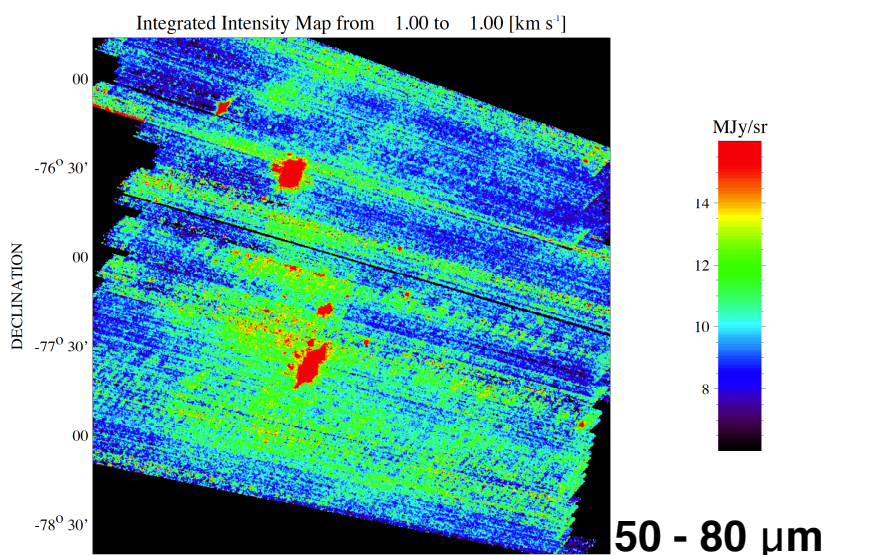
カメレオン分子雲での

広域・高感度マッピング観測領域



by Kawamura

FIR map of Chamaeleon I



YSO detected in the WIDE-S map



* 36 objects

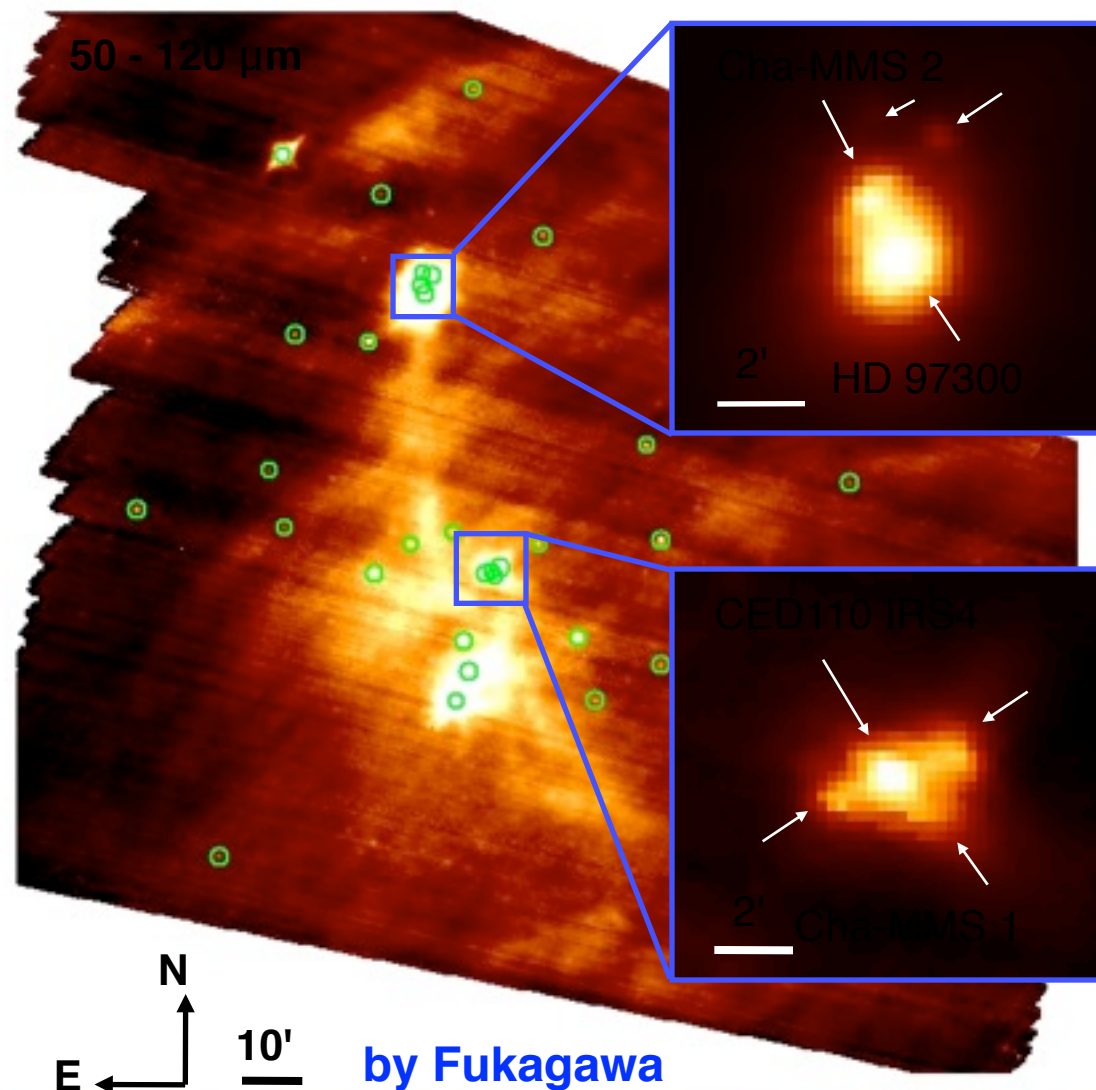
peak $> 3\sigma$, FWHM $\sim 40''$

- Known YSO : 25
- galaxies : 6
- Unknown : 5

* Position accuracy

versus 2MASS

- $\langle \Delta r \rangle = 9''$
- No systematic error



YSO detected in the WIDE-L map

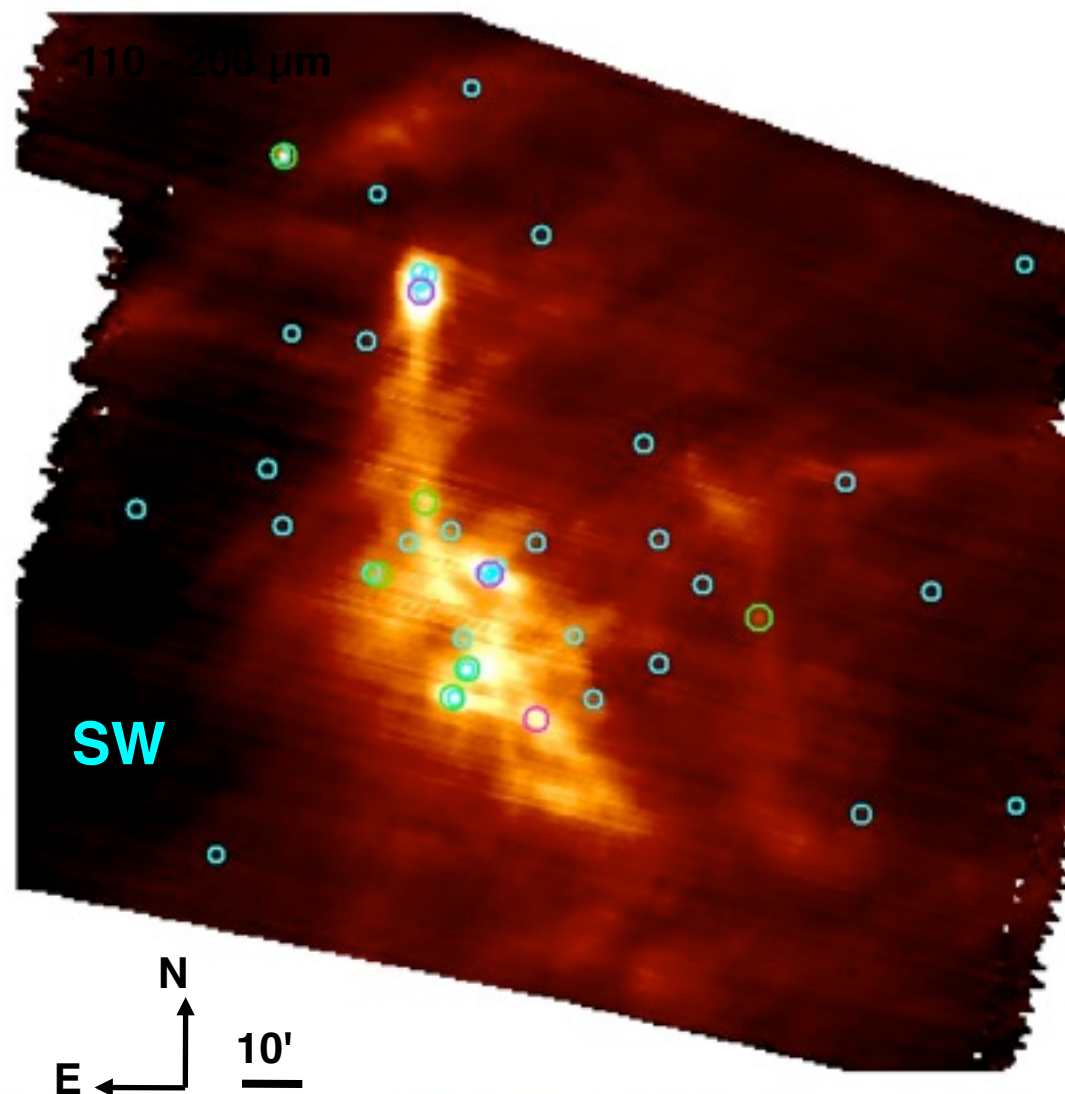
* 9 Objects

peak $> 3\sigma$, FWHM $\sim 60''$

- 3 $C^{18}O$ cores

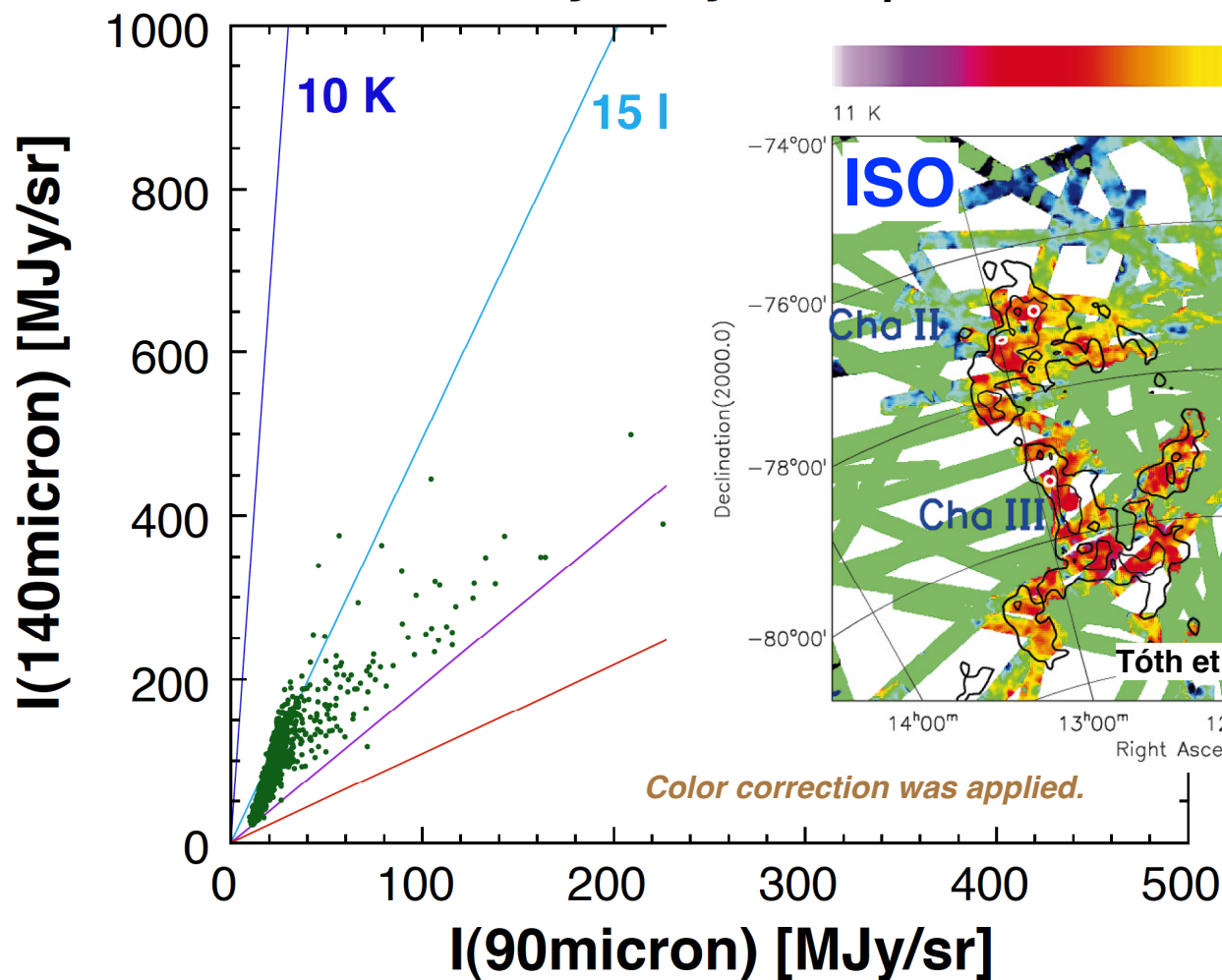
Mizuno et al. 1999

- 6 objects detected both of SW and LW maps

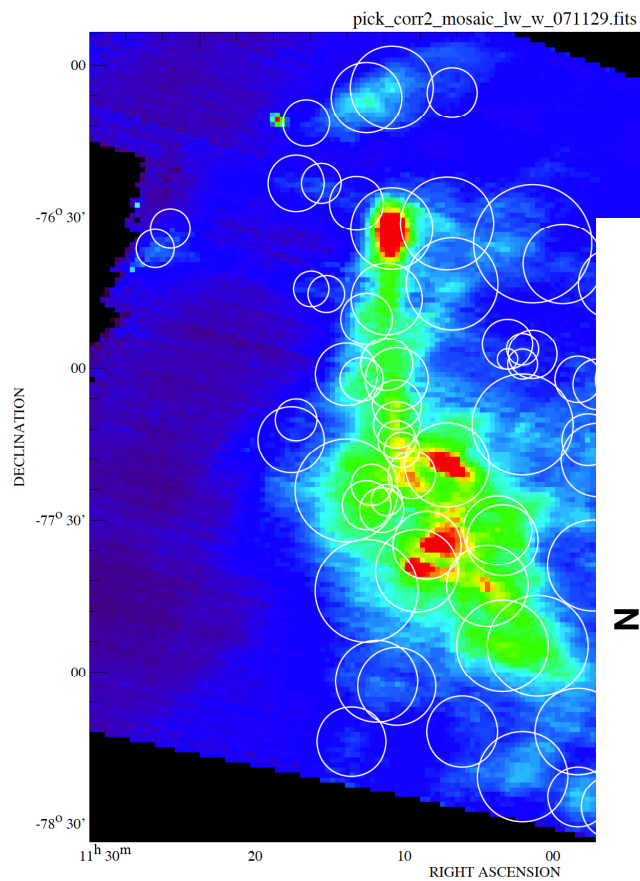


Color temperature of the dust

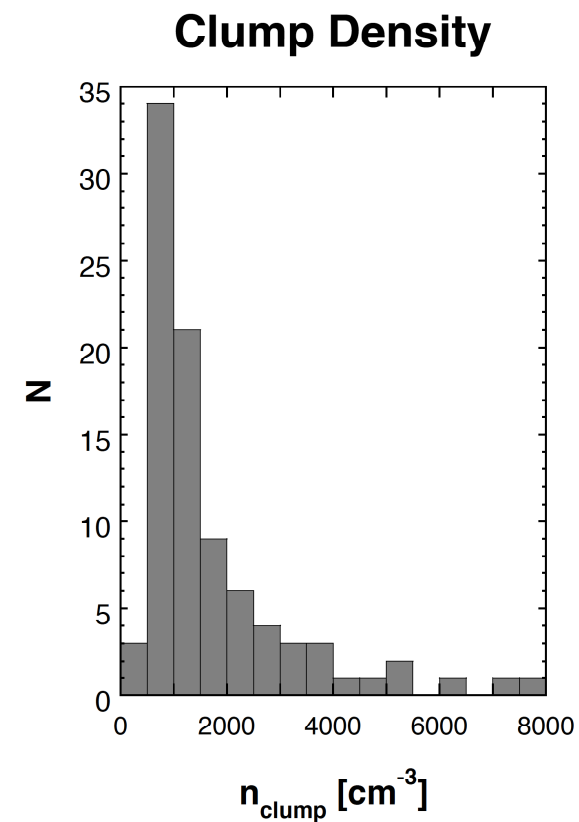
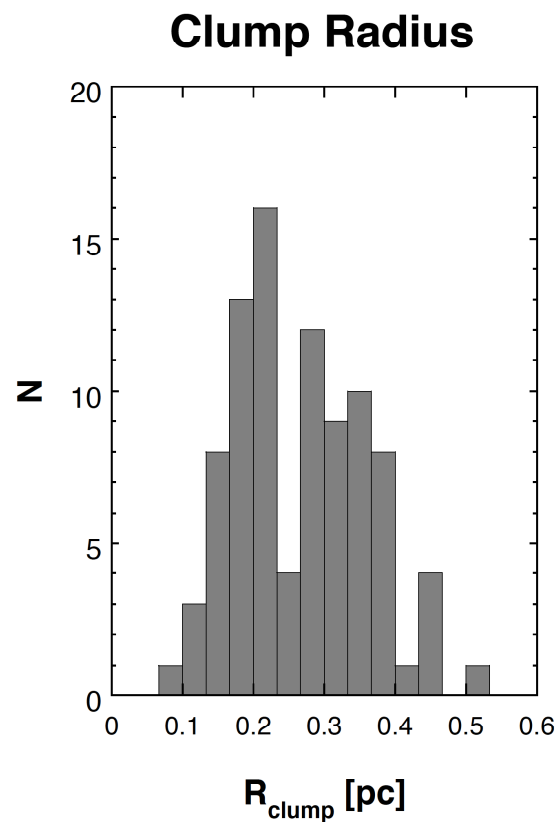
Color Temperature for Greybody with $\beta = 2$



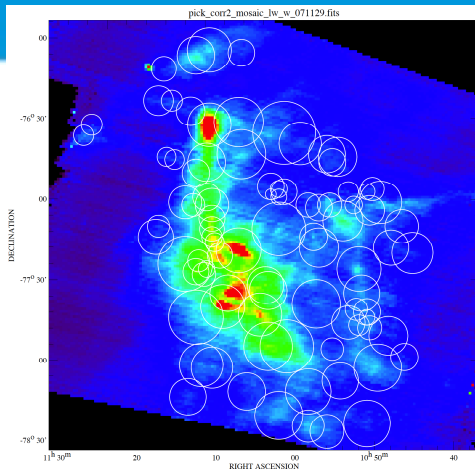
Mass function of the dust clumps



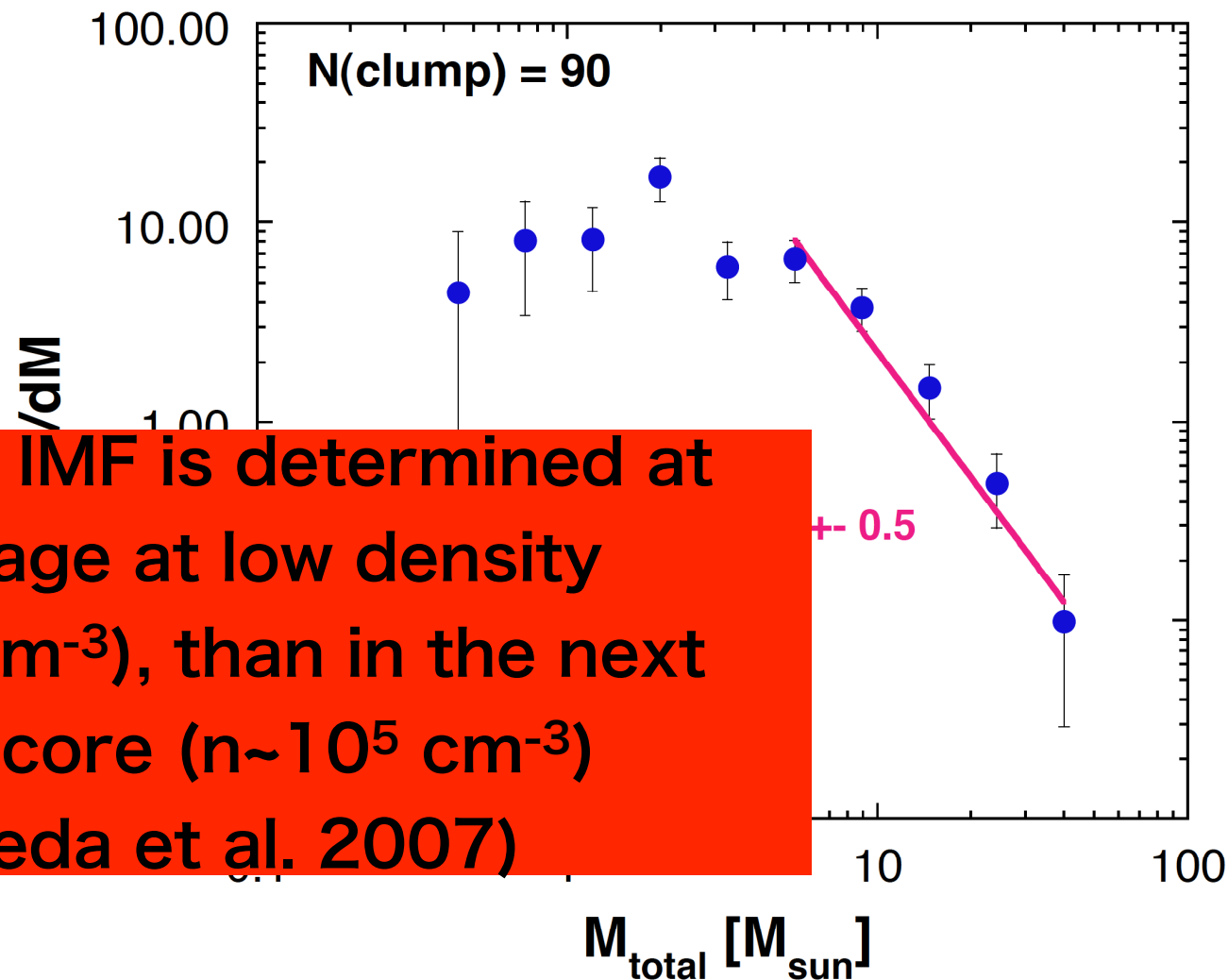
$N(\text{clump}) = 90$
by Clumpfind (Williams et al. 1994)



Mass function of the dust clumps



Dust Clump Mass Function in Chamaeleon I



γ -slope of the IMF is determined at rather early stage at low density cores ($n \sim 10^3 \text{ cm}^{-3}$), than in the next stage (H^{13}CO^+ core ($n \sim 10^5 \text{ cm}^{-3}$) reported by Ikeda et al. 2007)

Far-IR imaging observations of the Chamaeleon region



- 1. The observations have covered 210 pc² (33.79 deg²) in Chamaeleon with an effective spatial resolution of 69". The observed region includes not only the bright and major star-forming molecular clouds Cha I and II but also the relatively diffuse regions, Cha III, Major filament, and Cha East.*
- 2. The observed signals were converted to the brightness in MJysr⁻¹ by directly comparing with the DIRBE ZSMA data and the flux uncertainty results in ~20%. The positional calibration was also applied by using the near-infrared data obtained with AKARI/IRC and we achieved the pointing accuracy better than 4".*
- 3. The far-infrared images show that the brightness in the 90–160 μm bands becomes the strongest toward the Cha I sub-region and tends to decrease toward the east. Brightness in the 65 μm band does not have such a distinct trend. These features indicate that a warm dust component with temperature of ~20 K is uniformly distributed over the whole Chamaeleon region, while a cold dust component with temperature of ~10 K is prevailing particularly in the Cha I, II, and III sub-regions.*



Far-IR imaging observations of the Chamaeleon region



4. Assuming that the warm and cold dust components exist toward the Chamaeleon region, as inferred from the four band FIS images, we estimated the temperatures of the two components from the FIS images in conjunction with the DIRBE data. The temperature of the warm component is 22.1 ± 0.5 K and that of the cold component is 11.7 ± 2.5 K. Using these temperatures, we further derived the column density maps of the two components. The column density maps confirm that the warm component is uniformly distributed at a large spatial scale of ~ 50 pc, much larger than that of the cold component of \sim several pc. Note that both the components have numerous internal structures with sizes of 0.1–1 pc.

5. It is most likely that the cold component corresponds to the molecular clouds because the spatial correlation between the cold component and the molecular clouds is fairly good. In addition, the mean size and density of the cold component are estimated to be 1 pc and 3×10^3 cm⁻³, respectively, which are quite consistent with those of the molecular clouds. The size and density of the warm component are estimated to be ~ 50 pc and 0.9–15 cm⁻³, respectively, and therefore we believe that the warm component traces the cold H I clouds.

6. The distribution of the cold H I gas traced by the warm component extending into a large scale of ~ 50 pc can be well explained in the formation scenario of the CNM (cold neutral medium) through the thermal instability of the WNM (warm neutral medium) caused by an SN (super nova) shell with 100 pc size. The scenario, however, cannot describe the several pc-scale distribution of the cold component (formation of the molecular clouds). One might require the gravitational fragmentation of the cold H I gas or some external triggers, for example, the collision between the CNM and a high-velocity cloud with size of ~ 10 pc, previously proposed for the origin of the Chamaeleon molecular clouds.



Observed region

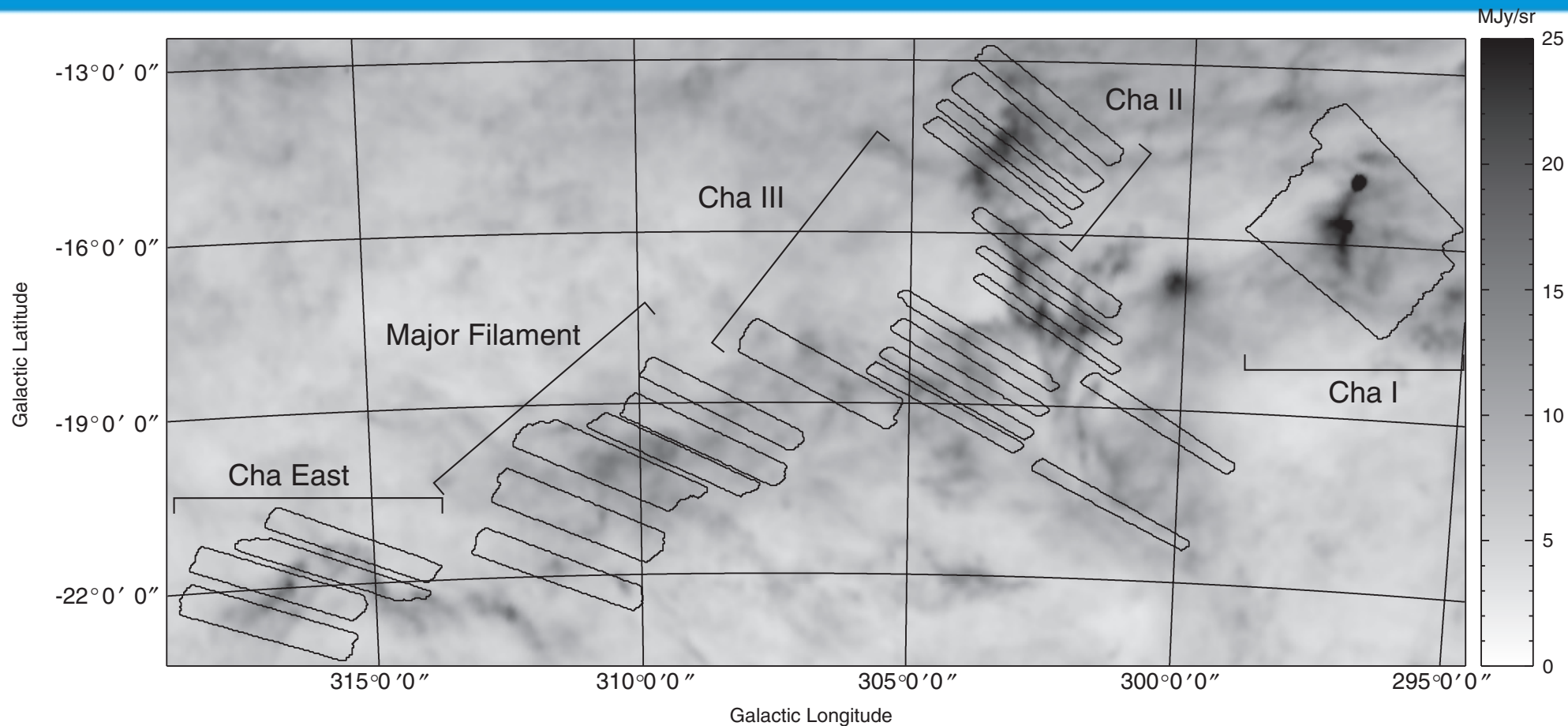


Figure 1. Observed regions are indicated by the black polygons on the 100 μm brightness map created by Schlegel et al. (1998). The gray-scale range is from 0 to 25 MJy sr^{-1} . Following Mizuno et al. (2001), the subregions of Cha I, Cha II, Cha III, Major Filament, and Cha East are indicated.

SED of Chamaeleon region

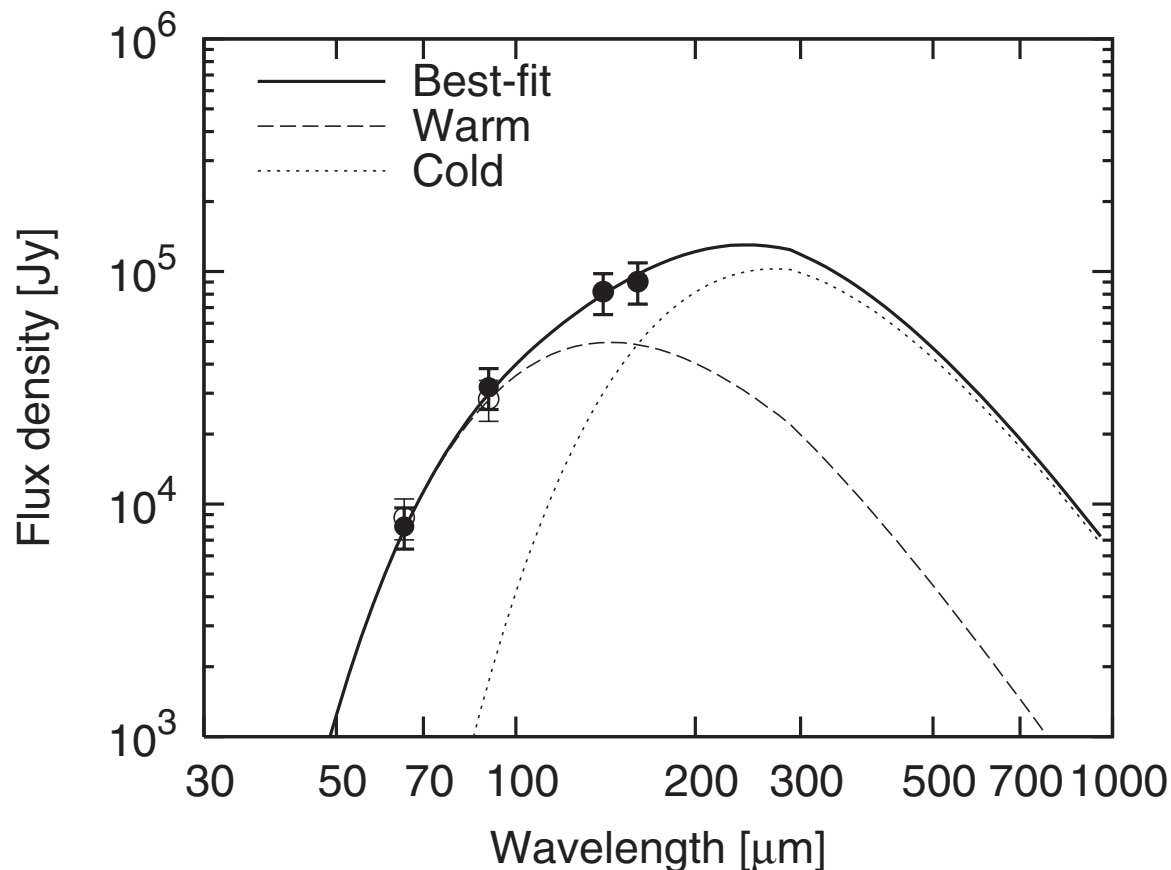
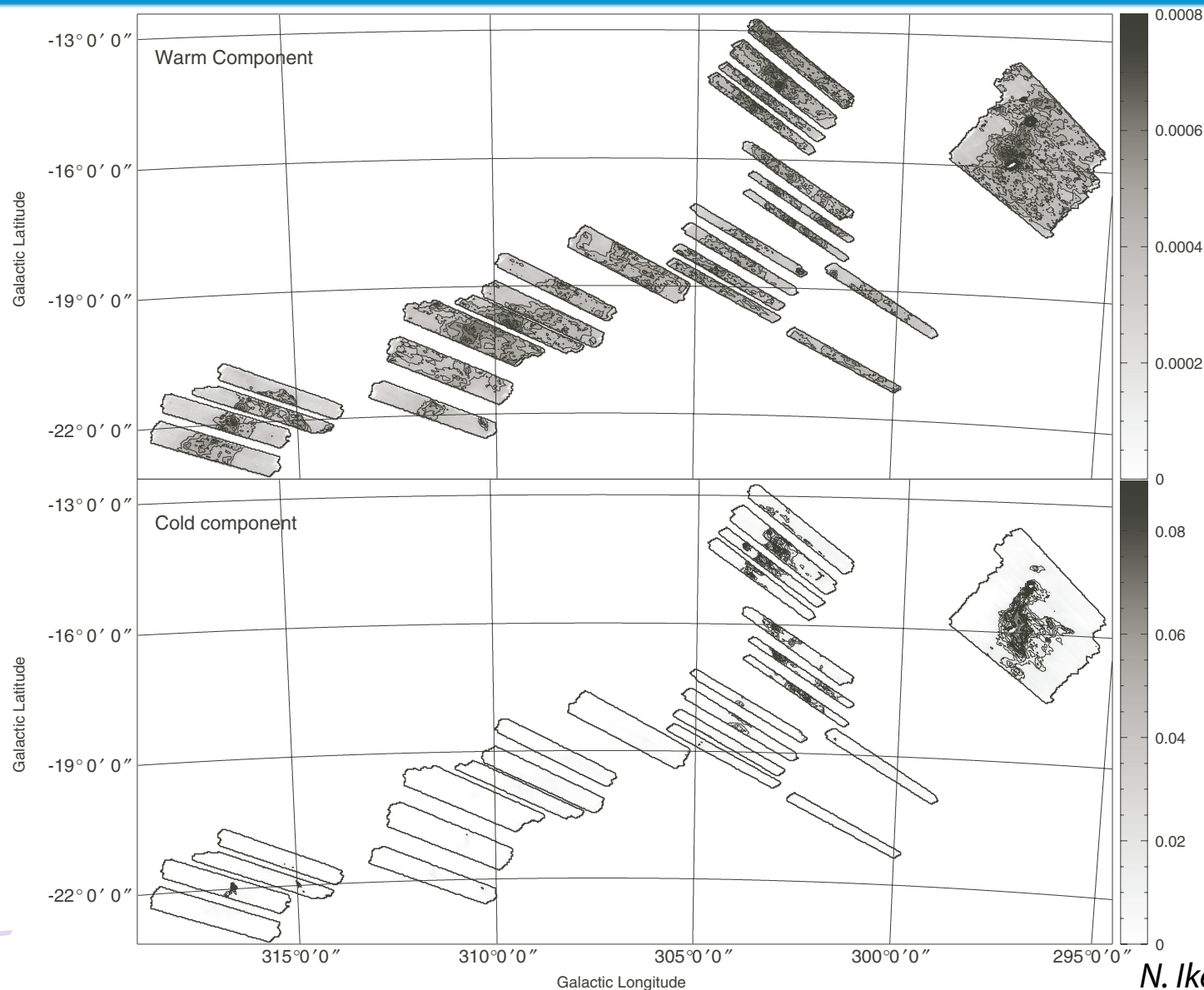


Figure 6. Total flux densities in the FIS bands toward the Chamaeleon region. The open and filled circles indicate the observed and color-corrected flux densities, respectively, and the error bars represent the uncertainties. The thick solid curve shows the best-fit two-component graybody function with $T_{\text{warm}} = 22.1$ K and $T_{\text{cold}} = 11.7$ K. The dashed and dotted curves show the warm and cold components of the best-fit function, respectively.

Column density map of the Chamaeleon region



Masses of the warm and cold components

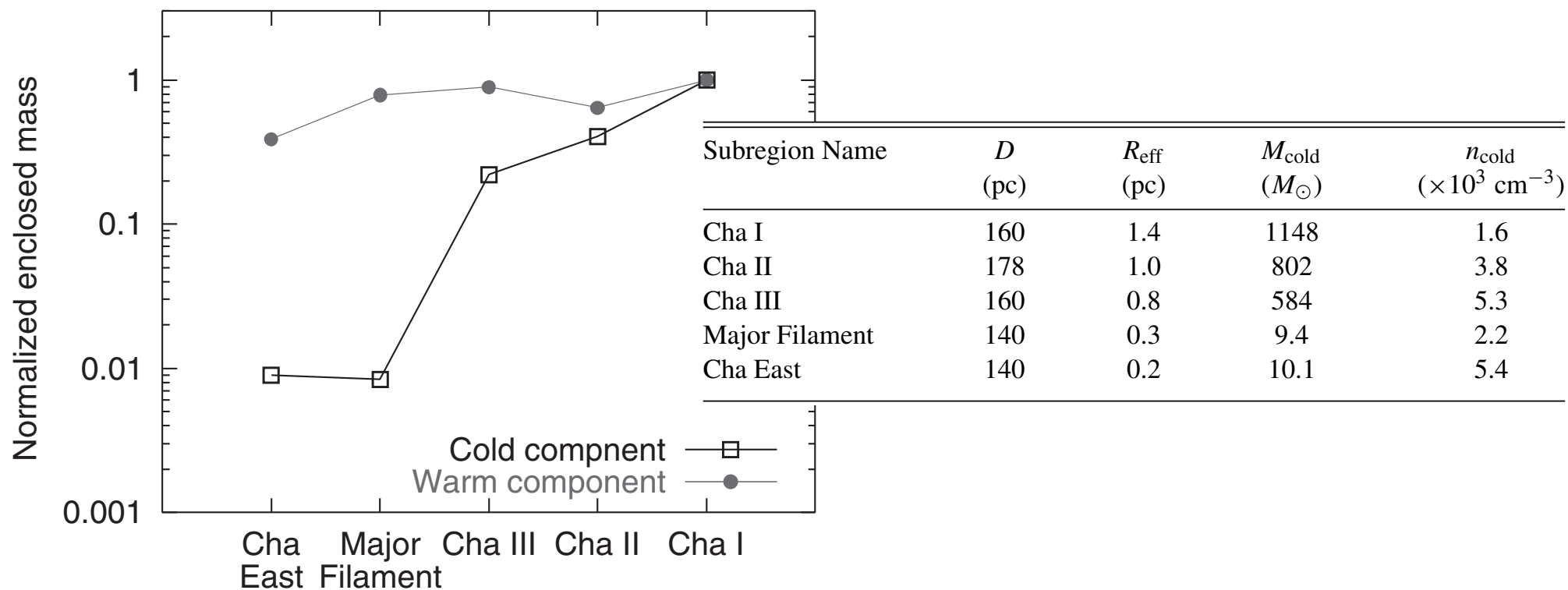


Figure 17. Masses of the warm and cold components enclosed in the observed area of each subregion, normalized by those of the Cha I subregion, are indicated by the thin-color filled circles and the thick-color open squares, respectively (see Section 6.2).



A survey of T Tauri stars with AKARI towards the Taurus-Auriga region



*Of the 517 known TTSs, 133 sources are detected by AKARI:
46 sources were not detected by IRAS.*

*Based on the colour-colour and colour-magnitude diagrams made from the AKARI, 2MASS, and UCAC surveys, the criteria to extract TTS candidates from the AKARI All-Sky data are proposed
68/133 AKARI detected TTSs have passed these criteria.*

On the basis of our criteria, we selected 176/14725 AKARI sources as TTS candidates that are located around the Taurus-Auriga region.

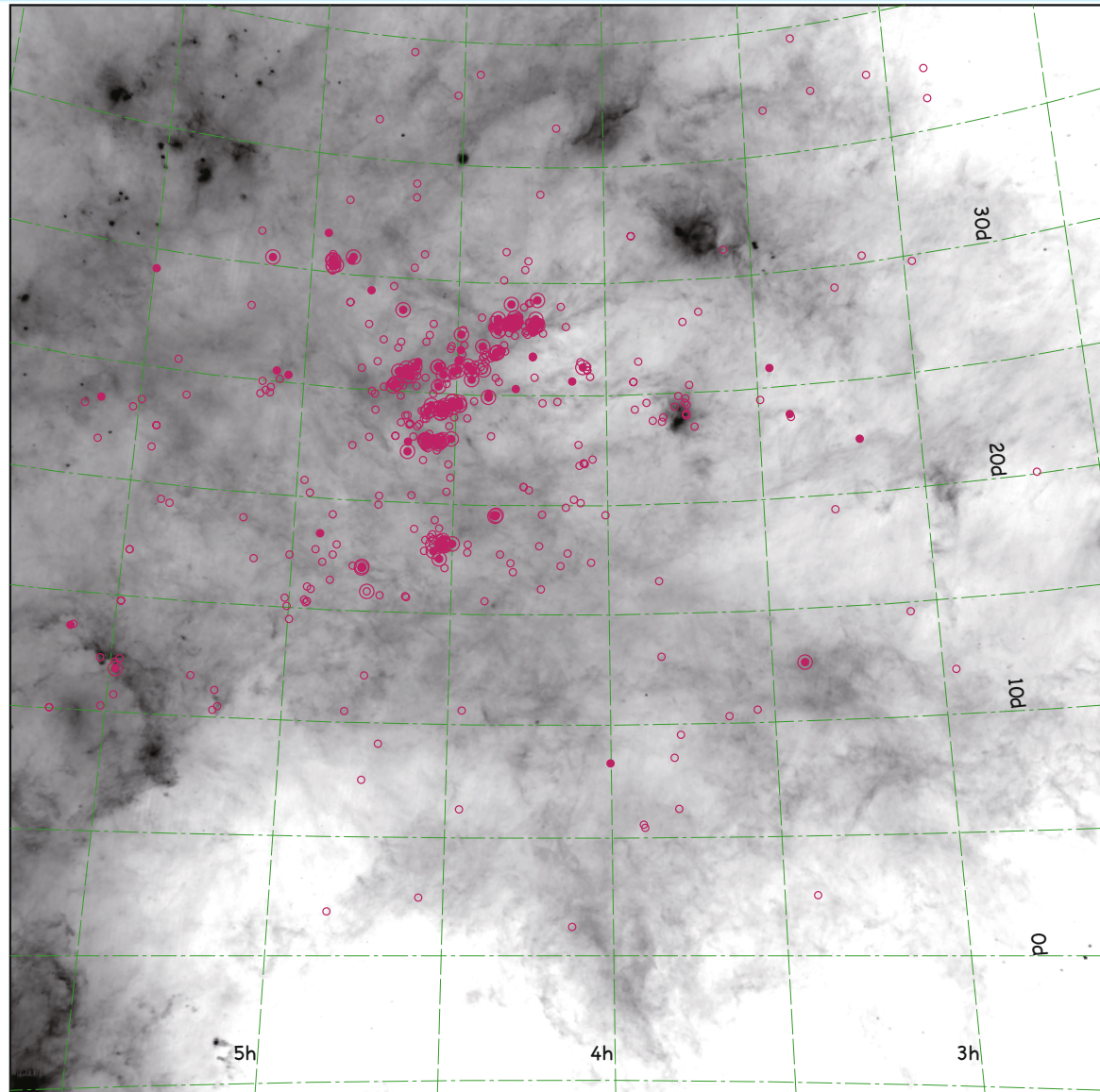
Based on SIMBAD identifications, we infer the TTS-identification probability using our criteria to be ~75%. We find 28 TTS candidates, of which we expect ~21 to be confirmed once follow-up observations can be obtained. Although the probability of ~75% is not so high, it is affected by the completeness of the SIMBAD database, and we can search for TTSs over the whole sky, and all star-forming regions.



Distribution of the target TTSs

Distribution of the target TTSs (small open circles). The small filled circles indicate the TTSs detected with AKARI and the large open ones represent the IRAS detection, on the IRAS 100 μm map.

S. Takita et.al., A&A 2010



Colour-colour diagram

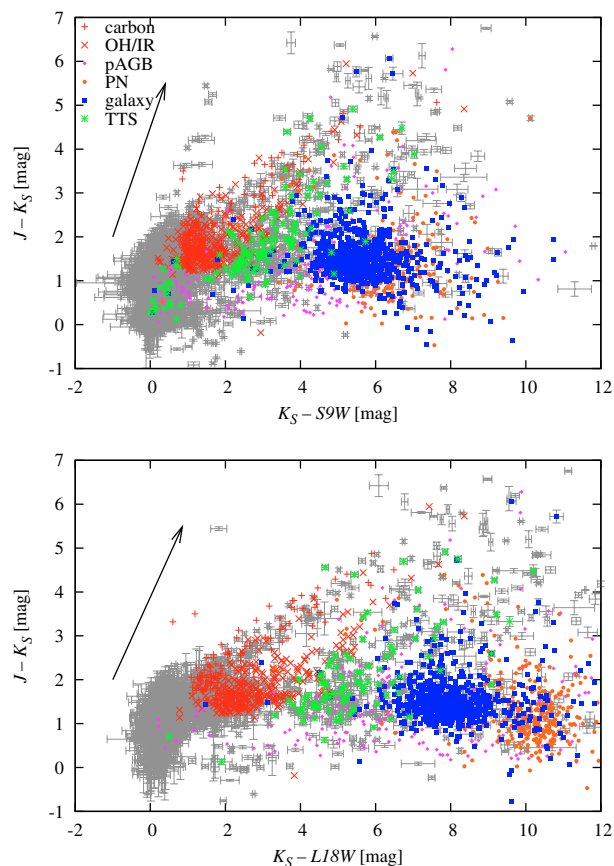


Fig. 6. *Top:* $(K_S - S9W)$ vs. $(J - K_S)$ colour-colour diagram. The grey dots with error bars indicate all the AKARI point sources in the selected Taurus-Auriga region. The red plus and cross symbols show carbon and OH/IR stars in the whole sky, respectively. The magenta diamonds, the orange circles, and the blue squares are post-AGB stars, PNe, and extragalactic objects in the whole sky, respectively. The green stars mean the TTSs in the Taurus-Auriga region. The arrow shows the interstellar extinction vector of $A_V = 20$ mag, estimated from the Weingartner & Draine (2001) Milky Way model of $R_V = 3.1$. *Bottom:* $(K_S - L18W)$ vs. $(J - K_S)$ colour-colour diagram. The symbols and arrow are the same as in the top panel.

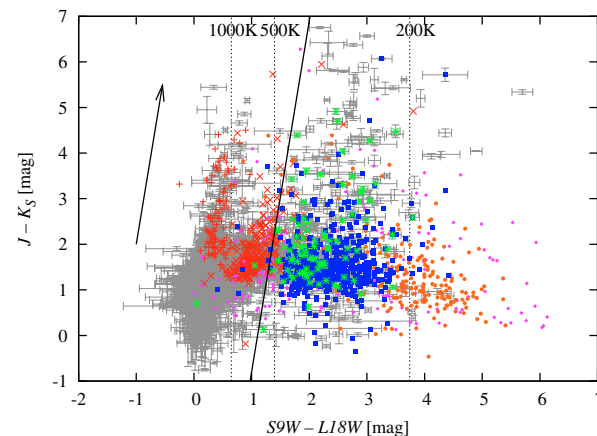


Fig. 7. $(S9W - L18W)$ vs. $(J - K_S)$ colour-colour diagram. The symbols and arrow are the same as in Fig. 6. The black solid line indicates our criterion (1). The black broken lines indicate $S9W - L18W$ colours of 200, 500, and 1000 K blackbody.

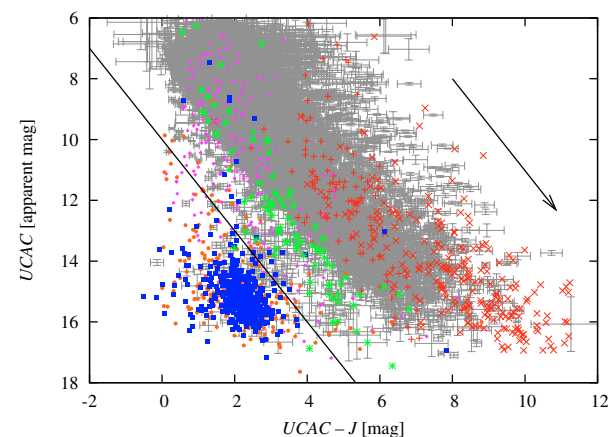


Fig. 8. $(UCAC - J)$ vs. $(UCAC)$ colour-magnitude diagram. The symbols are the same as in Fig. 6. The arrow shows the interstellar extinction vector of $A_V = 5$ mag, estimated from the Weingartner & Draine (2001) Milky Way model of $R_V = 3.1$. The black line indicates our criterion (2).

Ice absorption bands towards edge-on young stellar objects



Ice absorption bands at 2.5–5 μm towards eight low-mass YSOs were observed;
three class 0-I protostellar cores with edge-on geometry
two edge-on class II objects
two multiple systems with edge-on class II
one not-edge-on class II object.

Towards the class 0-I objects, L1527, IRC-L1041-2, and IRAS 04302
Abundant H₂O, CO₂, and CO ice in the envelope.
The column density ratio of CO₂ to H₂O ice is 21–28%
(coincides with the ratio observed by SST towards YSOs with various inclinations.)
The weak absorption at ~4.1 μm can be fitted by HDO ice
(HDO/H₂O ratio ranges from 2% to 22%).
The absorption in the vicinity of the CO band (4.76 μm) is double-peaked
fitted by combining CO ice, OCN–, and CO gas.

Towards the edge-on class II objects, ASR41 and 2MASS J1628137-243139,
H₂O band was detected.
low optical depth of the water feature is due to geometrical effects (Pontoppidan et al. 2005).
The detected water ice mainly originates in the disk.
HK Tau B and HV Tau C are edge-on class II objects in multiple systems.
detected the absorption of H₂O ice and CO₂ ice.



Target list



Name	Coordinates (J2000) ^a	Class	Note
L1527(IRAS 04368+2557)	04:39:53.6 +26:03:05.5	0-I	WCCC, $i \sim 85^\circ$ ^b
IRC-L1041-2	20:37:21, +57:44:13	0-I ^c	nearly edge-on ^c
IRAS 04302+2247	04:33:16.45, +22:53:20.7	0-I	$i \sim 90^\circ$ ^d
ASR 41	03:28:51.291, +31:17:39.79	II	$i \sim 80^\circ$ ^e
2MASSJ 1628137-243139	16:28:13.7, -24:31:39.00	II	$i \sim 86^\circ$ ^f
HV Tau	04:38:35.280, +26:10:39.88	II	multiple system ($i \sim 84^\circ$ ^g)
HK Tau	04:31:50.900, +24:24:17.00	II	binary ($i \sim 85^\circ$ ^h)
UY Aur	04:51:47.31, +30:47:13.9	II	$i \sim 42^\circ$



Absorption results



Name	Coordinates (J2000) ^a	Class	Note
L1527(IRAS 04368+2557)	04:39:53.6 +26:03:05.5	0-I	WCCC, $i \sim 85^\circ$ ^b
IRC-L1041-2	20:37:21, +57:44:13	0-I ^c	nearly edge-on ^c
IRAS 04302+2247	04:33:16.45, +22:53:20.7	0-I	$i \sim 90^\circ$ ^d
ASR 41	03:28:51.291, +31:17:39.79	II	$i \sim 80^\circ$ ^e
2MASSJ 1628137-243139	16:28:13.7, -24:31:39.00	II	$i \sim 86^\circ$ ^f
HV Tau	04:38:35.280, +26:10:39.88	II	multiple system ($i \sim 84^\circ$ ^g)
HK Tau	04:31:50.900, +24:24:17.00	II	binary ($i \sim 85^\circ$ ^h)
UY Aur	04:51:47.31, +30:47:13.9	II	$i \sim 42^\circ$

	H ₂ O	HDO	¹² CO ₂	CO	XCN
Absorption peak [μ m]	3.05	4.07	4.27	4.67	4.62
Band strength 10^{-17} cm molecule ⁻¹	20	4.3	7.6	see text	5.0
Column density	10^{17} [cm ⁻²]				
L1527(04368+2557)	47 ± 13	0.96 (2.0%) ^a	10 ± 1.1 (21%)	18 ± 2.6 (38%)	1.5 ± 0.22 (3.2%)
IRC-L1041-2	39 ± 6.6	3.7 (9.5%)	9.4 ± 1.6 (24%)	18 ± 4.0 (46%)	2.5 ± 0.48 (6.4%)
IRAS 04302+2247	24 ± 0.82	5.3 (22%)	6.8 ± 0.64 (28%)	3.1 ± 0.55 (13%)	0.53 ± 0.064 (2.2%)
ASR 41	7.8 ± 2.2	–	–	–	–
2MASSJ 1628137-243139	6.7 ± 2.6	–	–	–	–
HV Tau	5.4 ± 0.23	1.0 (19%)	0.72 ± 0.11 (13%)	–	–
HK Tau	2.1 ± 0.23 ^b	–	0.9 ± 0.11 (43%)	–	–
UY Aur	0.61 ± 0.20	–	0.54 ± 0.086 (89%)	–	–

太陽系における観測



惑星間塵

- 起源, 空間分布・構造, 軌道進化, Composition, COBE-DIRBE モデルからの脱却
 - 大局的な構造の観測: 起源、軌道進化
 - 微細構造: 起源
 - 分光学的観測: ダストの組成、起源

小惑星

- 含水鉱物という切り口で、小惑星を系統的に調べる
 - Albedo の大規模データ
 - 分光学的観測による、含水鉱物の吸収スペクトルの系統的観測

彗星

- ダスト組成、Crystalline silicate はどこから?
 - 分光学的観測: ダストの組成、起源



太陽系天体の観測プログラム(SOSOS)



PI: Munetaka UENO (Univ. Tokyo)

Masateru ISHIGURO, Jeonghyun PYO, SeungSoo HONG

(Seoul National University)

Sunao HASEGAWA, Fumihiko USUI (ISAS/JAXA)

Takafumi OOTSUBO (Nagoya Univ.), SukMinn KWON (Kwangwon Univ.)

Daisuke KINOSHITA (Nat'l Central Univ.), Yuki SARUGAKU (Univ. of Tokyo)

Hideyo KAWAKITA (Kyoto Sangyo Univ.), Tadashi MUKAI (Kobe University)

Thomas G. MÜLLER (Max-Planck-Institut, Garching)

(所属は当時)



Albedo, Size, and Surface Characteristics of Hayabusa-2 Sample-Return Target 162173 1999 JU3 from AKARI and Subaru Observations

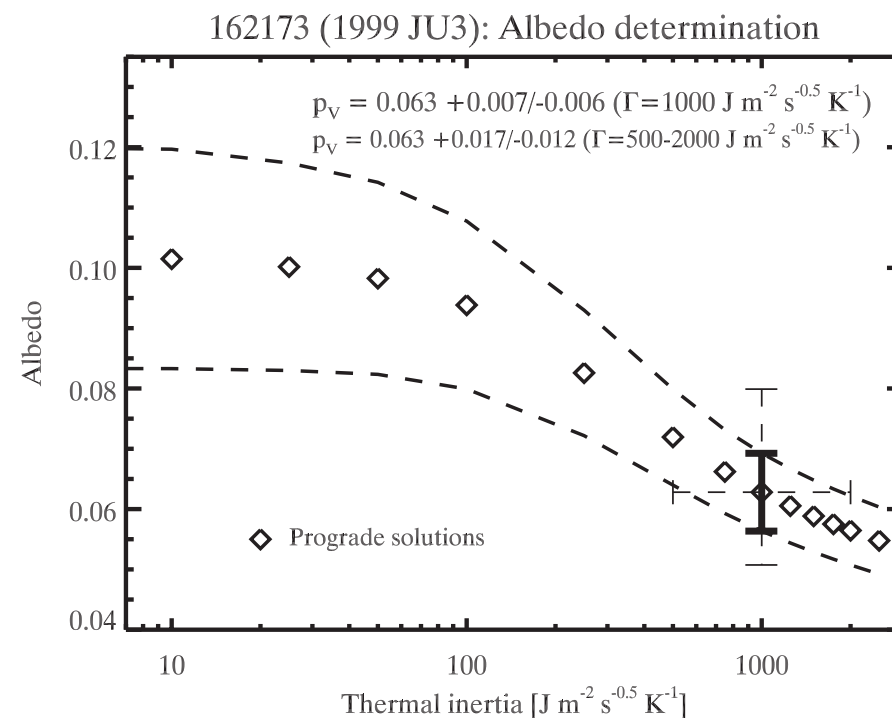
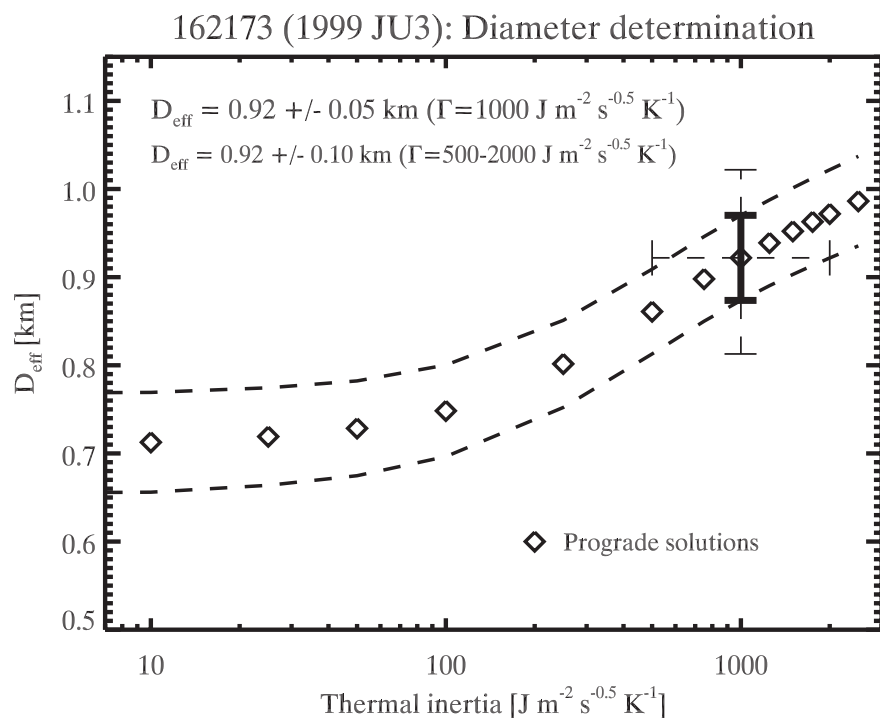
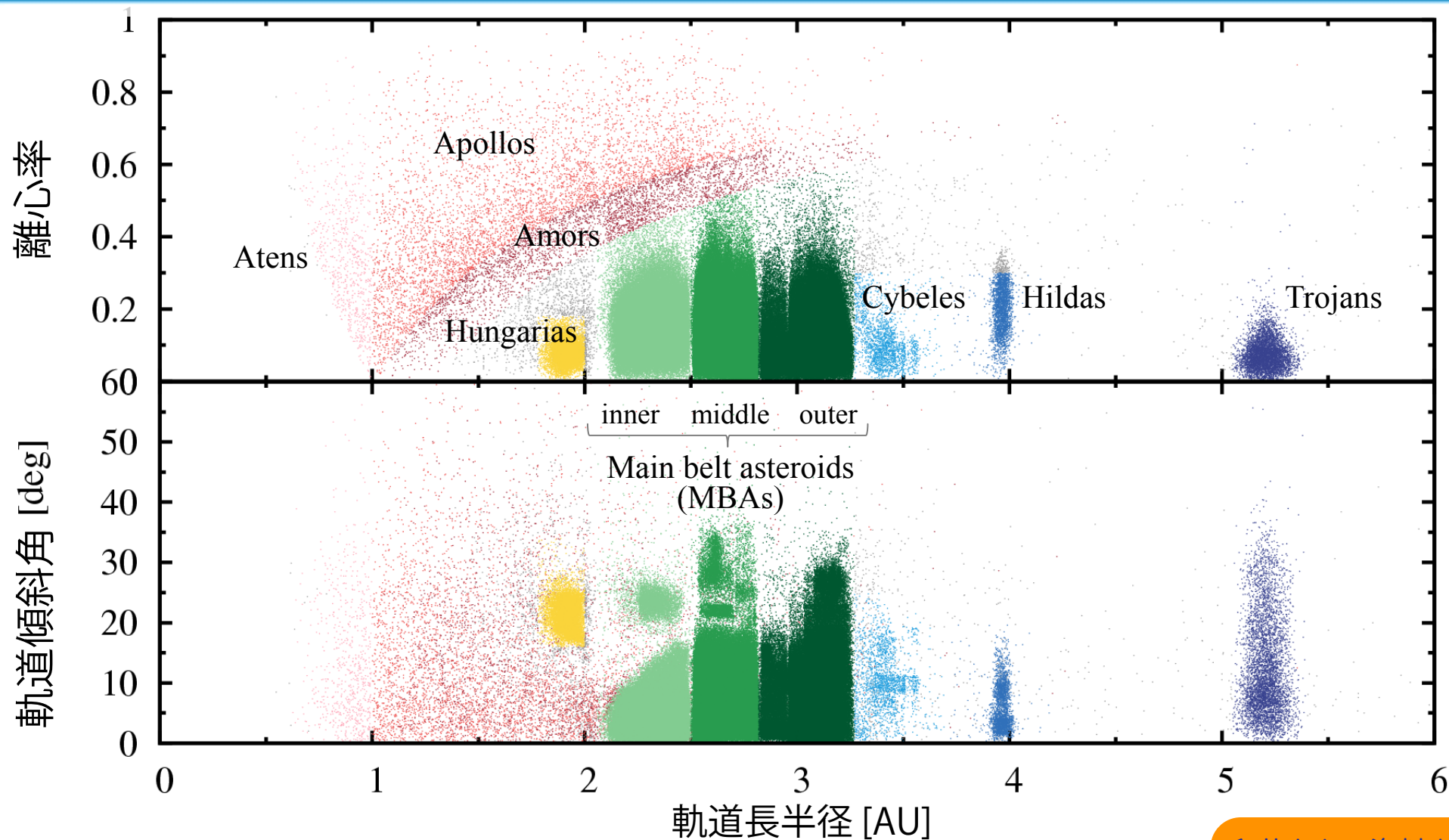


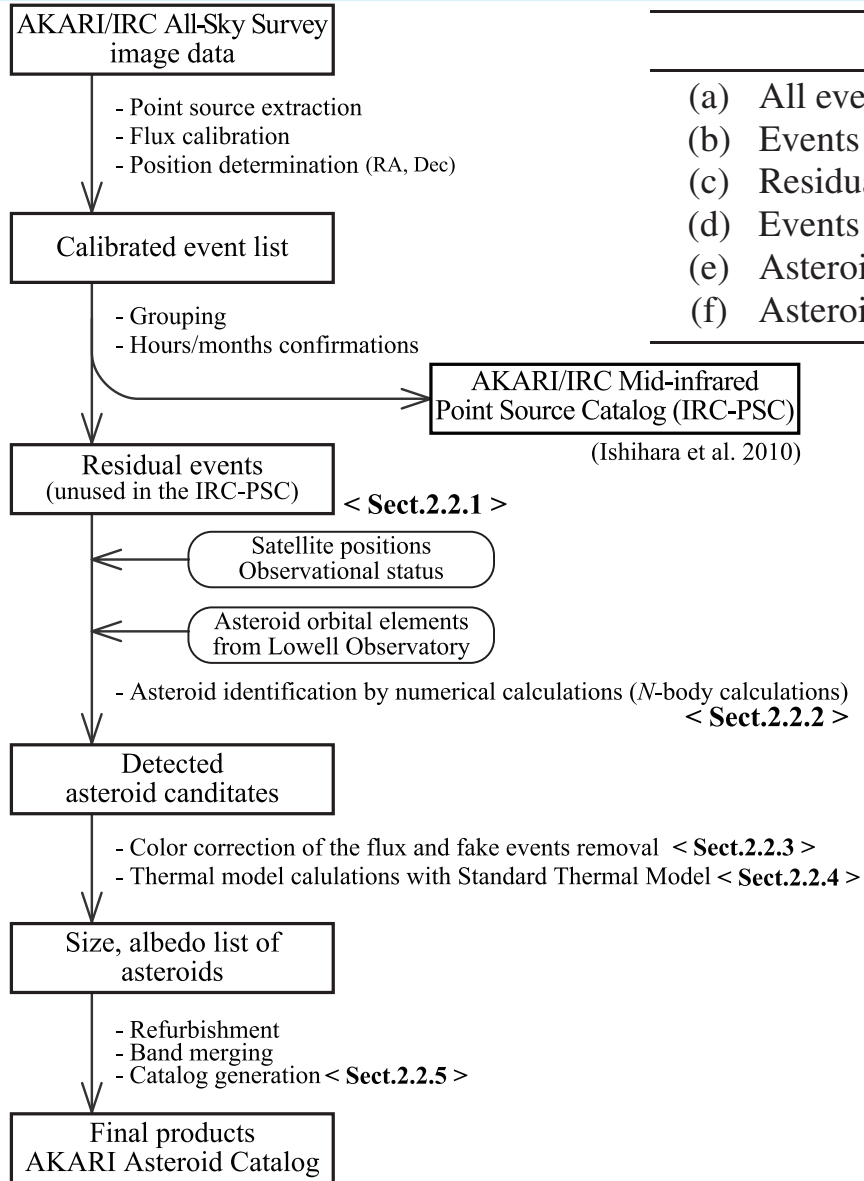
Fig. 5. Overall diameter and albedo solutions as a function of the thermal inertia assuming a prograde ellipsoidal shape model. The dashed lines reflect only the observational uncertainties.



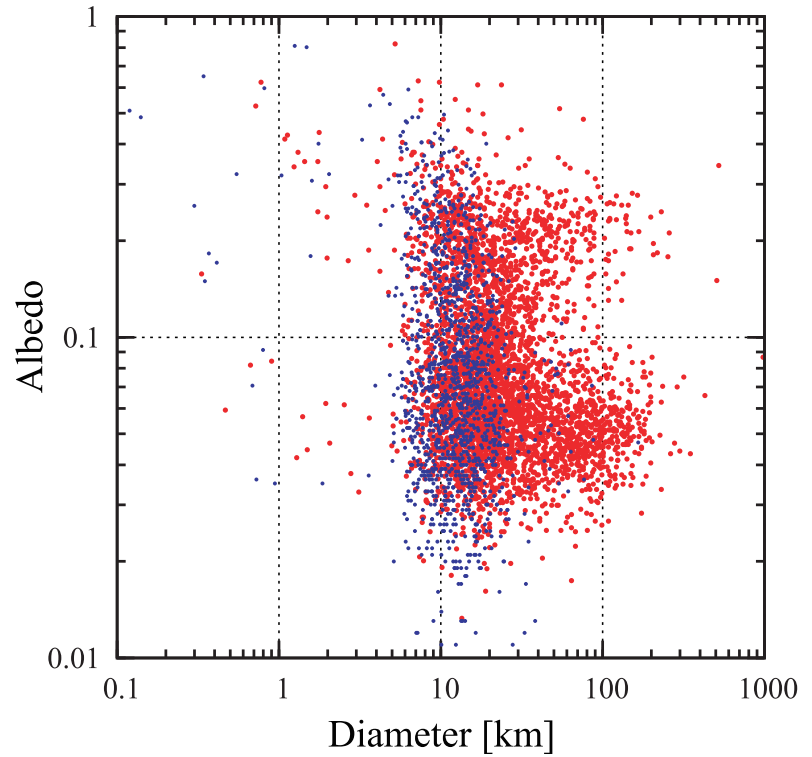
小惑星の軌道分布



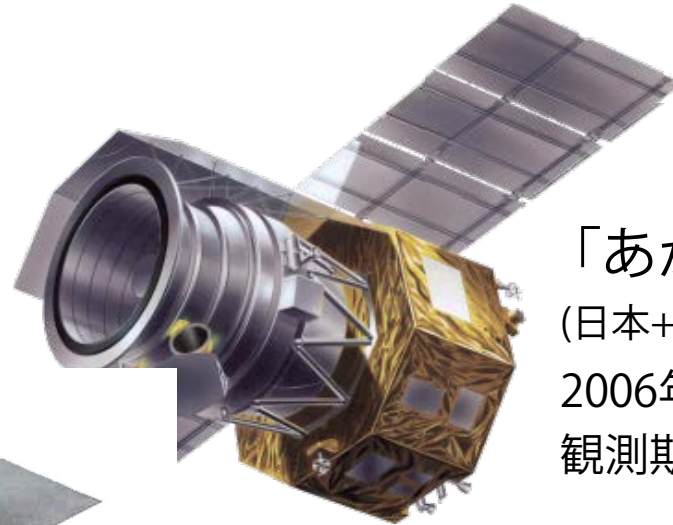
Asteroid Catalog Using AKARI: AKARI/IRC Mid-Infrared Asteroid Survey



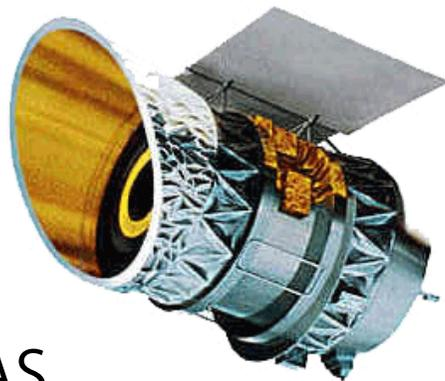
Event	S9W	L18W
(a) All events	4762074	1244249
(b) Events employed in the IRC-PSC	3882122	936231
(c) Residual events	879952	308018
(d) Events identified as asteroids	6924	13760
(e) Asteroids in the final catalog	2507	5010
(f) Asteroids detected overall	5120	



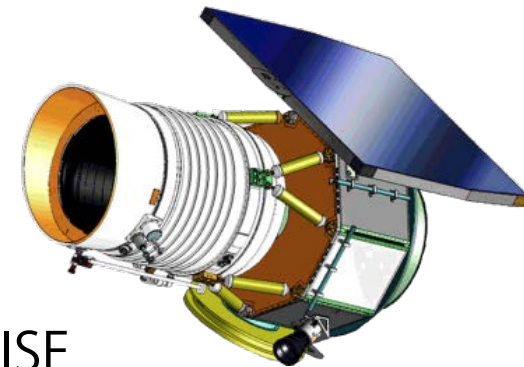
3つの赤外線サーベイ衛星



「あかり」
(日本+ヨーロッパ)
2006年打ち上げ、高度 750km
観測期間：16ヶ月

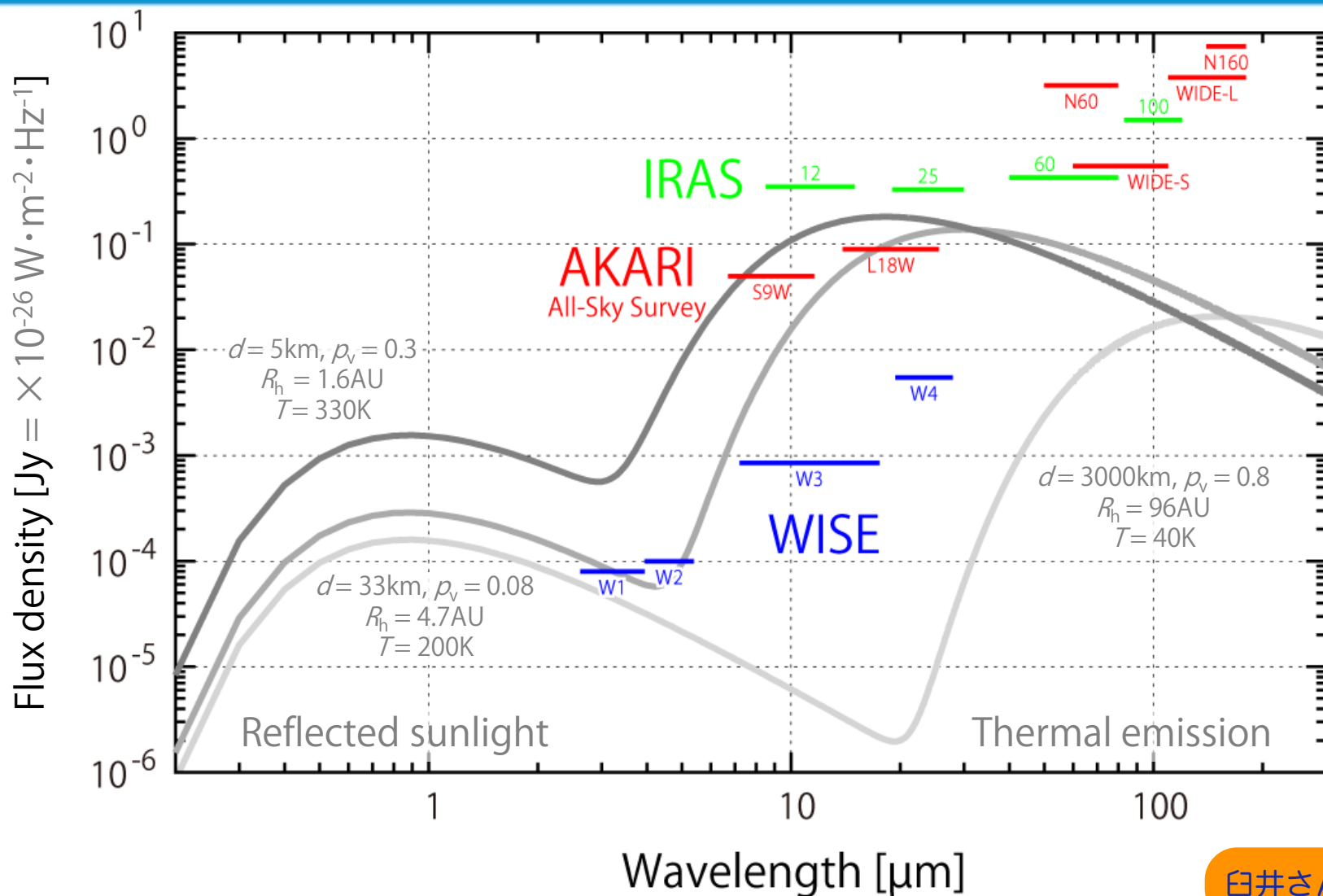


IRAS
Infrared Astronomical Satellite
(アメリカ, オランダ, イギリス)
1983年打ち上げ、高度 900km
観測期間：9ヶ月半



WISE
Wide-field Infrared Survey Explorer
(アメリカ)
2009年打ち上げ、高度 525km
観測期間：9ヶ月

3ミッションの検出限界比較

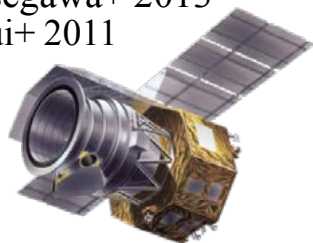


白井さんの資料より

3ミッションの小惑星カタログ



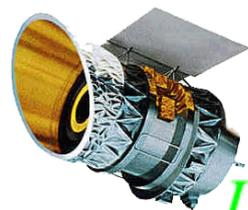
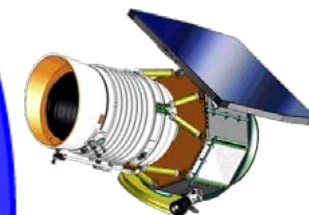
Hasegawa+ 2013
Usui+ 2011



AKARI
(5199)

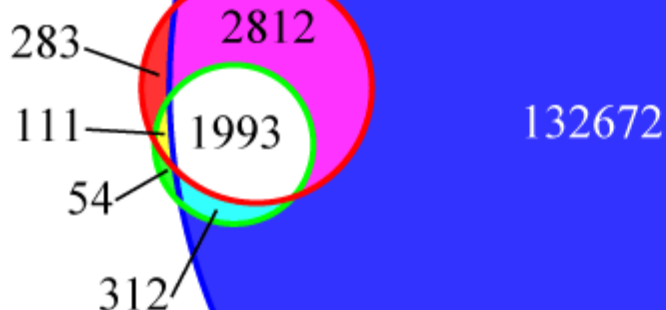
WISE
(137789)

Mainzer+ 2011, 2012
Masiero+ 2011, 2012
Grav+ 2011, 2012a, b
(ただしいずれも暫定版)



IRAS
(2470)

Tedesco+ 2004

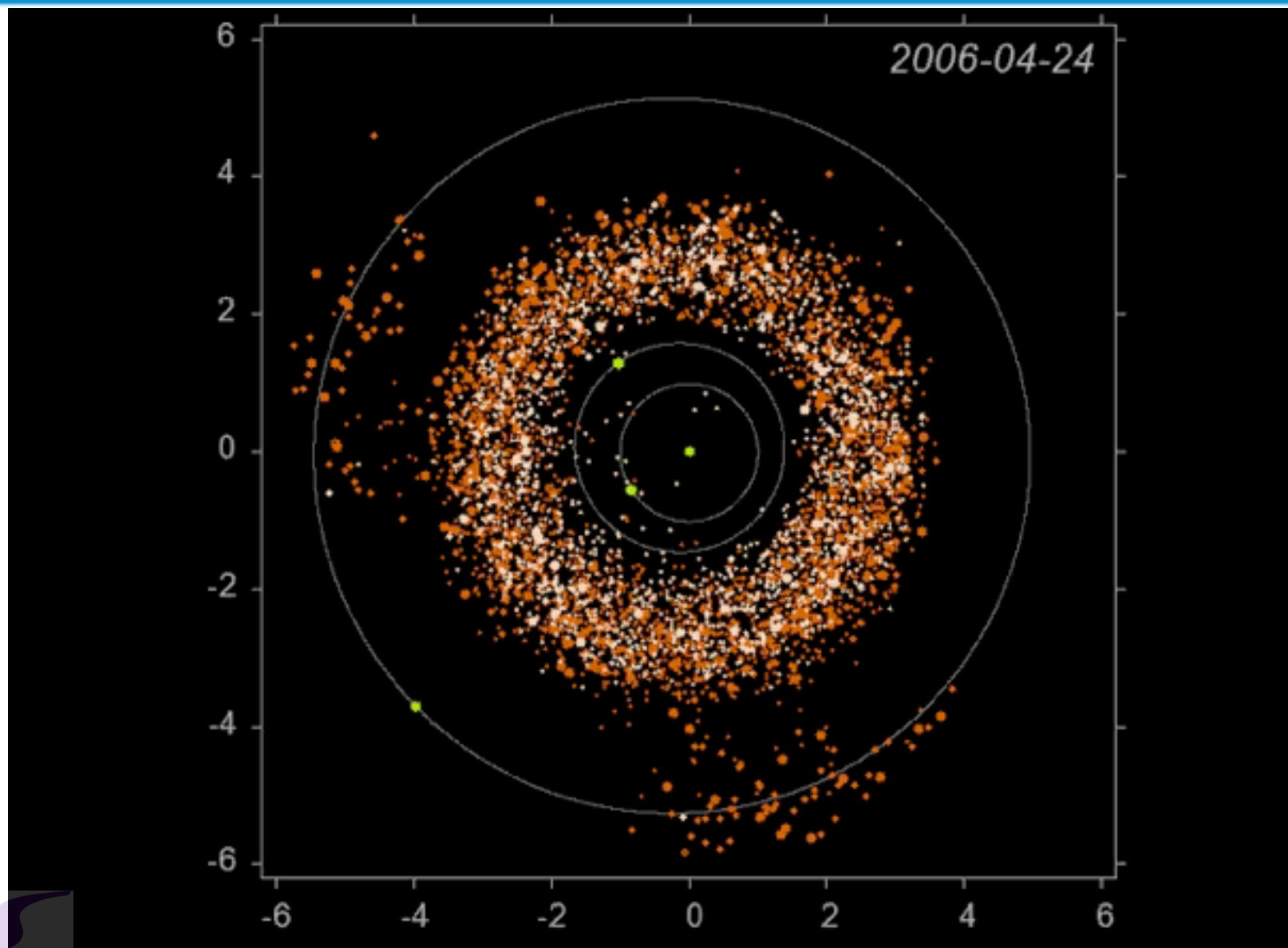


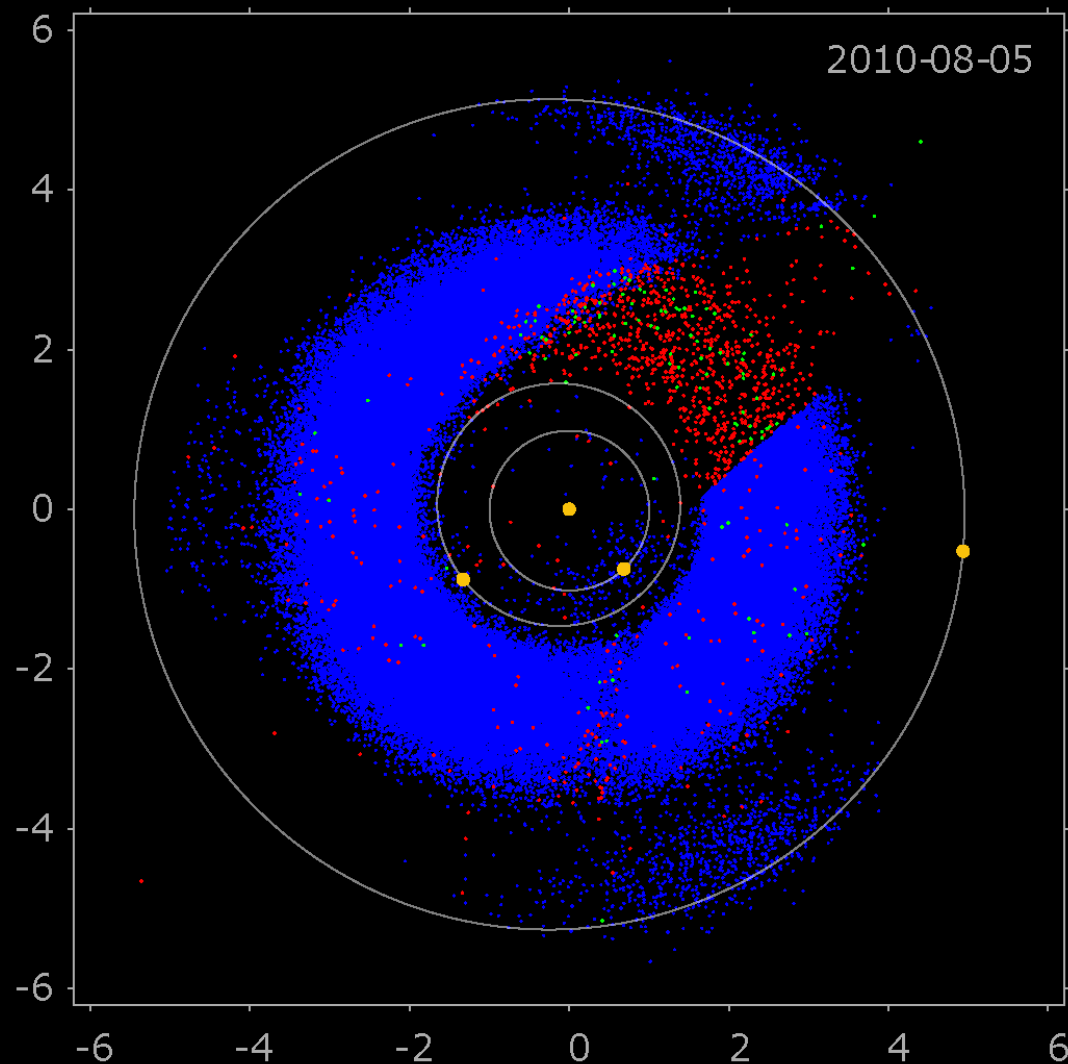
白井さんの資料より

total: 138237



あかりで観測された小惑星





IRAS: 2,470

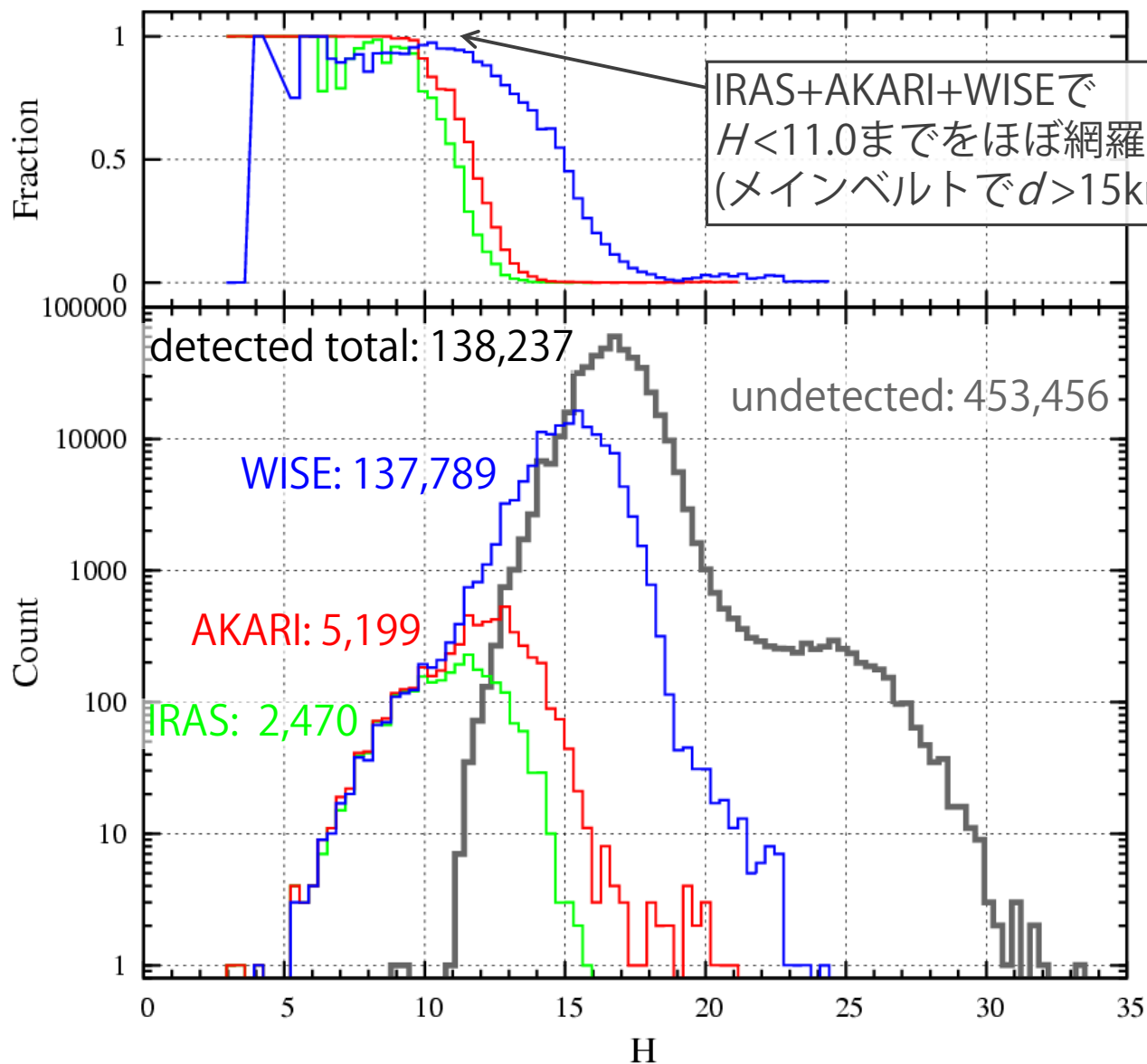
AKARI: 5,120

WISE: 131,563

total: 132,774



絶対等級に対するヒストグラム



絶対等級に対するヒストグラム

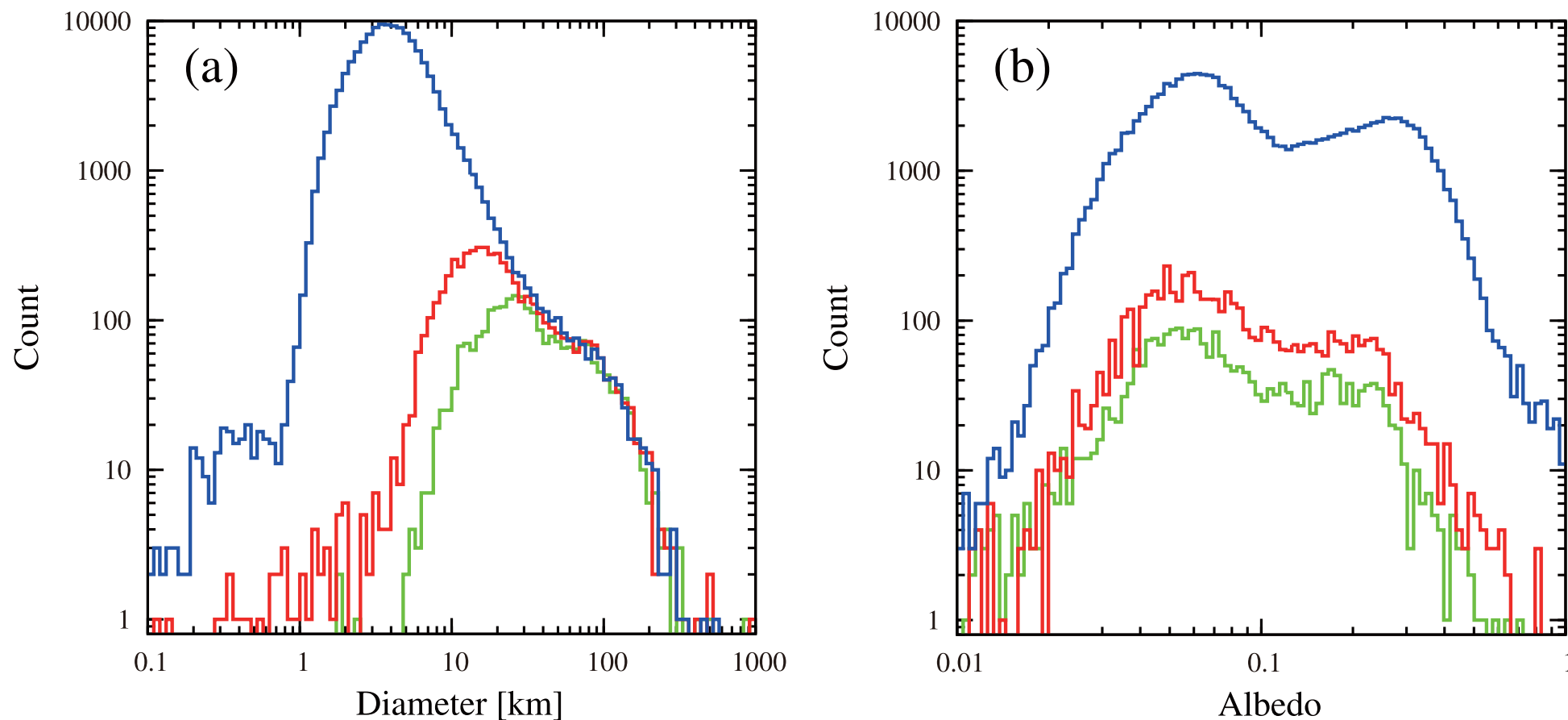


Fig. 3. Distribution of (a) diameter and (b) albedo of asteroids detected by IRAS (green), AKARI (red), and WISE (blue). The bin size is set at 100 segments for the range of 0.1 to 1000 km in the logarithmic scale for (a) and 100 segments for the range of 0.01 to 1.0 in the logarithmic scale for (b). (Color online)



Asteroids: Fraction/Semimajor axis



Analysis of the albedo properties of MBAs detected by AKARI.

Of the 5120 AcuA asteroids, 4722 are MBAs, and 1974 are provided as a complete data set of MBAs larger than $d > 20$ km.

Albedo distribution of MBAs is strongly bimodal; this trend is present not only in the distribution of the total population, but also in the distributions of inner, middle, and outer MBAs. The bimodal distributions are separated into two major groups at an albedo value of $p_v = 0.1$, which demarcates low-albedo C-type and high-albedo S-type asteroids.

Albedo distribution is size-dependent, and the variation in albedo values is greater at smaller sizes.

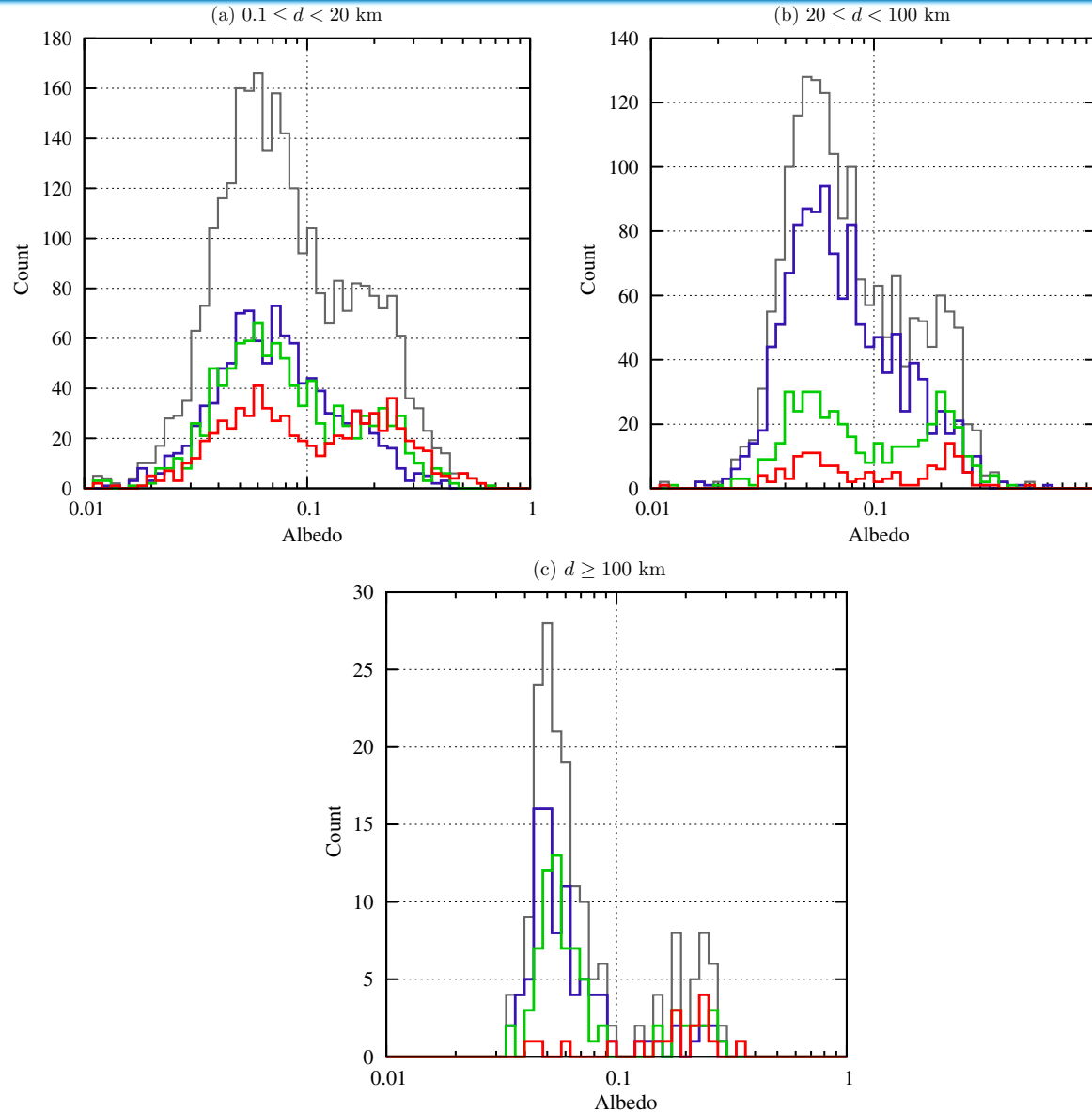
For smaller asteroids, the effects of surface heterogeneities on albedo are relatively large, while such local heterogeneities are averaged out and seemingly homogenized for larger asteroids.

Albedo distributions in S-type asteroids appear to be affected by the space weathering, whereas the albedo distributions in C-type asteroids are partially explained by the effects of metamorphism.

Mean albedo is nearly constant and independent of heliocentric distance throughout the entire main belt region, irrespective of taxonomic type. In the total distribution, on the other hand, the mean albedo value gradually decreases with increasing the semimajor axis, presumably due to the compositional mixing ratios of taxonomic types.

Almost 90% of the X-type MBAs in the AcuA data set can now be subdivided into E-, M-, and P-types based on the AKARI-derived albedos. The distribution of P-types, which have lower albedos among the X-types, are spread through-out the main belt regions, and increases beyond 3 AU, while the proportion of medium-albedo M-types decreases. P-type asteroids are considered to have similar origin or similar evolutionary process, to C- or D-types.

Asteroids: Fraction/Albedo



Asteroids: Fraction/Semimajor axis

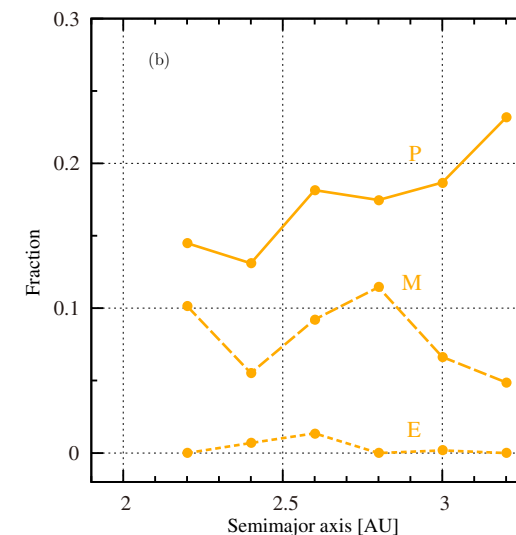
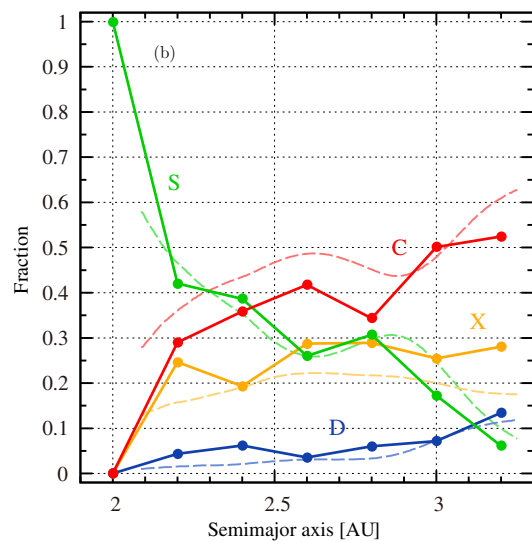
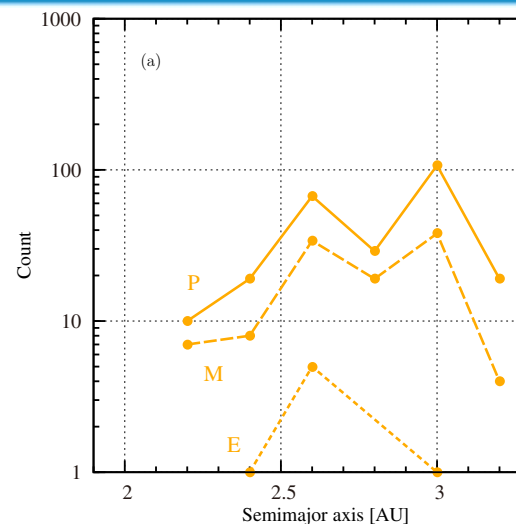
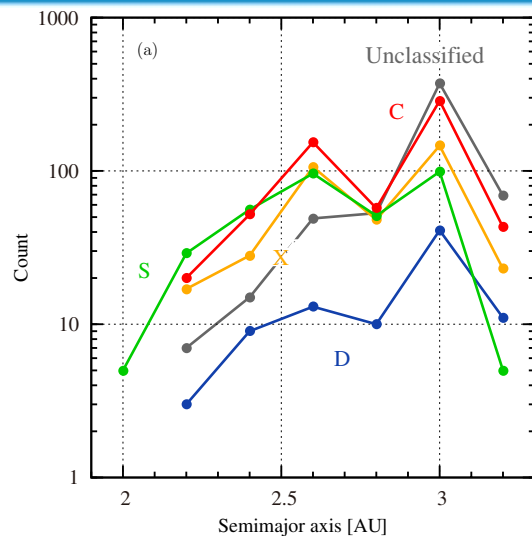
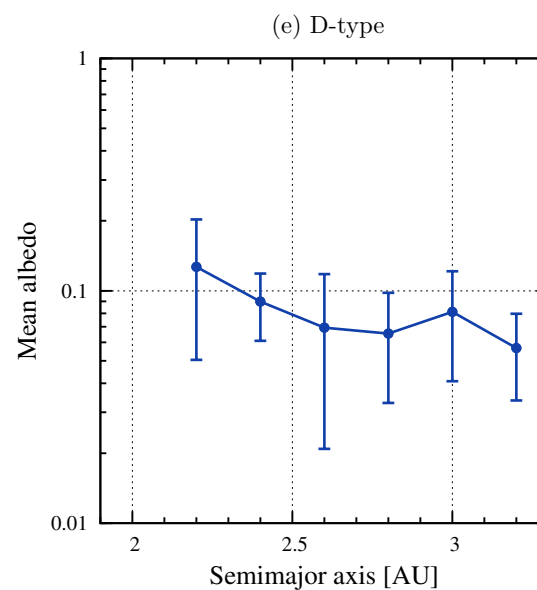
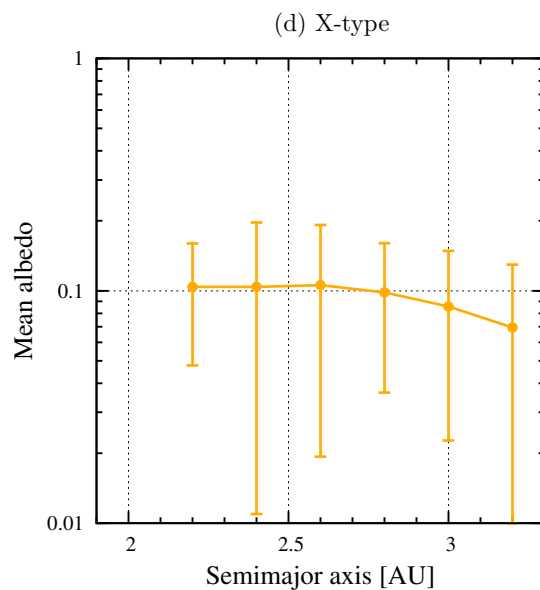
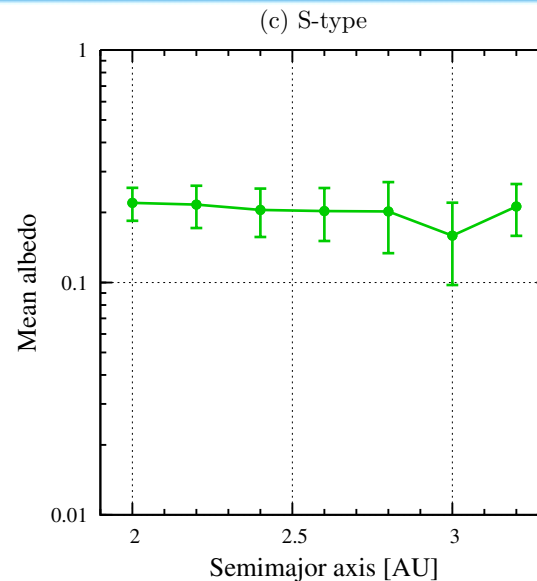
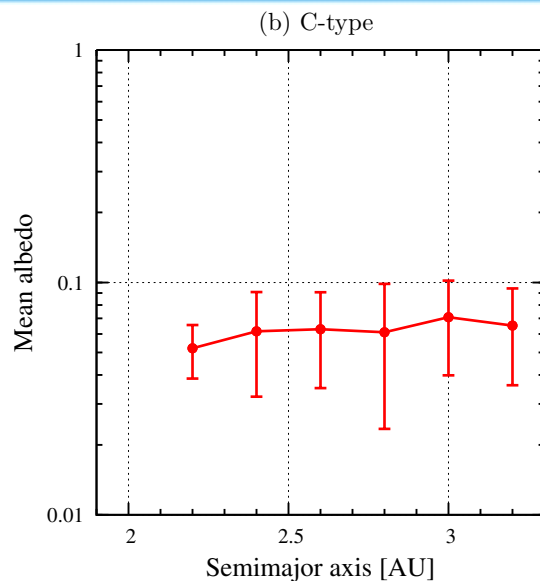


Figure 8. Histograms showing the numerical distribution (a) and fractional distribution (b) of MBAs with $d \geq 20$ km for each of the taxonomic types. Bold lines in (b) show AcuA data (this study) and dashed lines show data from Bus & Binzel (2002). Red, green, yellow, and blue denote C-, S-, X-, and D-type asteroids, respectively.

Figure 9. Histograms showing the numerical distribution (a) and fractional distribution (b) of X-type MBAs with $d \geq 20$ km. Dotted, dashed, and bold lines denote E-, M-, and P-type asteroids, respectively. (A color version of this figure is available in the online journal.)

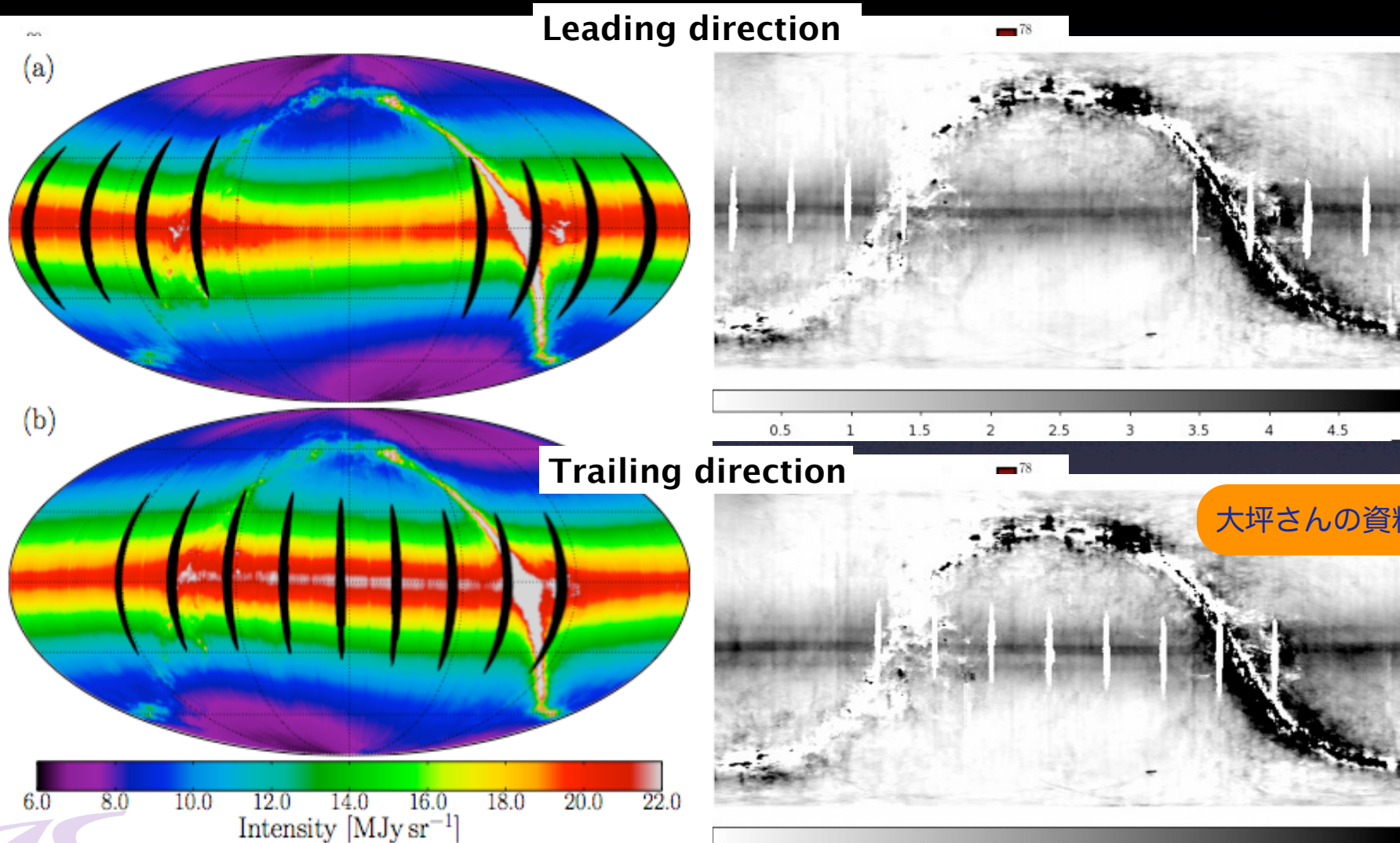


Asteroids: Mean albedo/Semimajor axis



IDP cloud の分光観測

The Sky Observed by AKARI 18 & 90 μ m-band



Comet observations



*18 comets, including both OCs and the JFCs, were spectroscopically observed
This is the largest homogeneous database of CO₂/H₂O production rate ratios in comets obtained so far.*

The prominent emission bands of the fundamental vibrational bands of H₂O at 2.7μm and CO₂ at 4.3μm can be seen in all of the comet spectra, except for the comet 29P/Schwassmann-Wachmann.

*The gas production rate ratios of CO₂, with respect to H₂O, in the 17 comets have been derived.
The present data set of the large samples confirms the range of ratios that previous measurements have obtained.
The CO₂/H₂O ratio in cometary ice spans from several to ~30% among the comets observed within 2.5 AU from the Sun, where H₂O effectively sublimates from the nucleus of the comet.
The range of the CO₂/H₂O ratios represented by the upper and lower quartile values is 11%–24% (the median value is 17%), and it is comparable with that of the high-mass protostellar ices (12%–22%),
while the mixing ratios of CO₂ in low-mass protostar envelopes is 22%–35% (Oberg et al. 2011).
CO₂ in cometary ice is more depleted with respect to water and more diverse than the low-mass protostellar ices.
If the cometary ice composition has not been significantly altered after the formation of cometary nuclei, then the ices incorporated into the comets should have been altered in the early solar nebula.
Based on our observations, the CO/CO₂ ratio in comets seems to be smaller than unity. This may indicate that there is a highly oxidized environment for the formation of molecules, or that CO has been exhausted in the vicinity of the surface of the cometary nuclei. However, it should be noted that we had the upper limits for CO in many of the comets, and CO was only detected in a few cases. We will require more samples of CO₂ and CO observations for further discussions.*

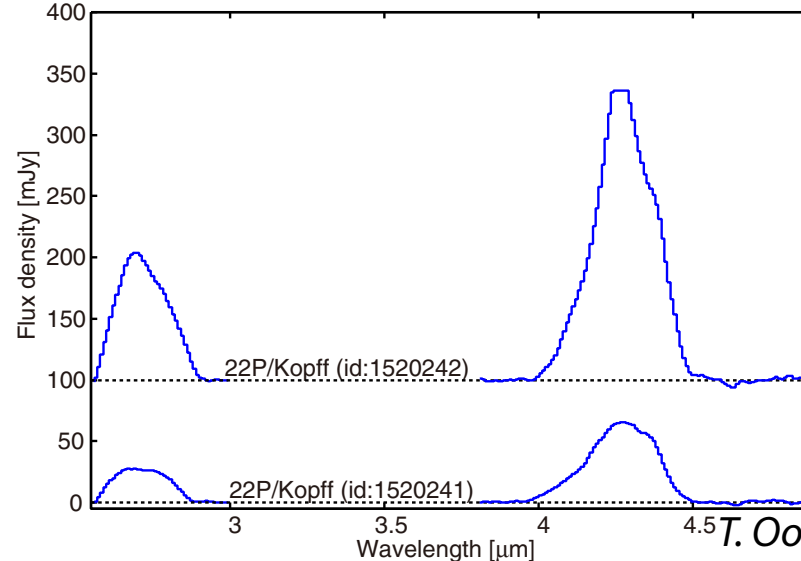
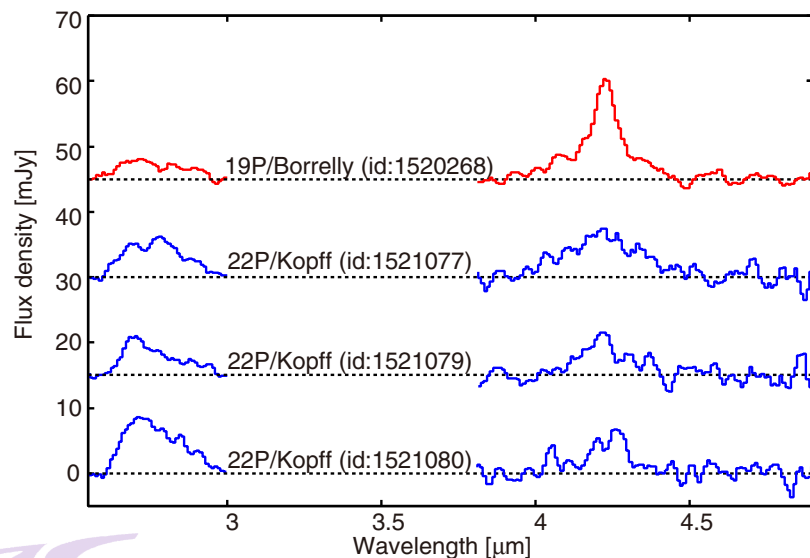
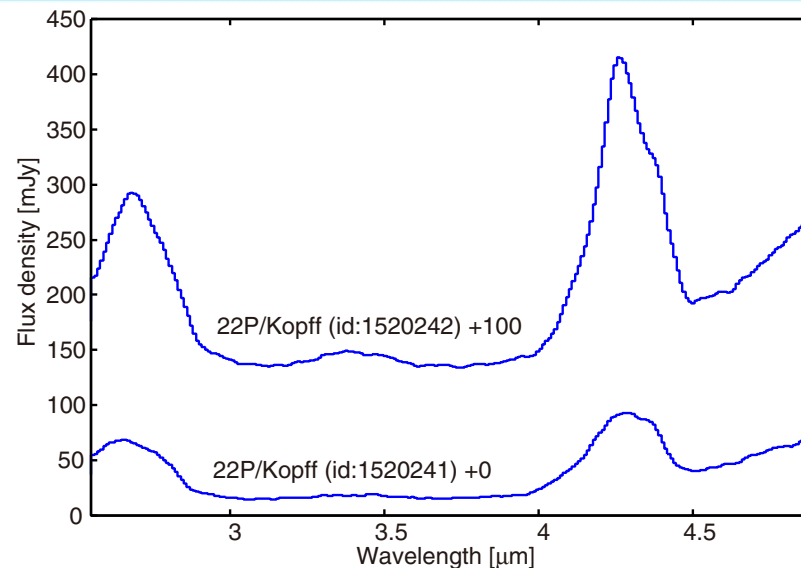
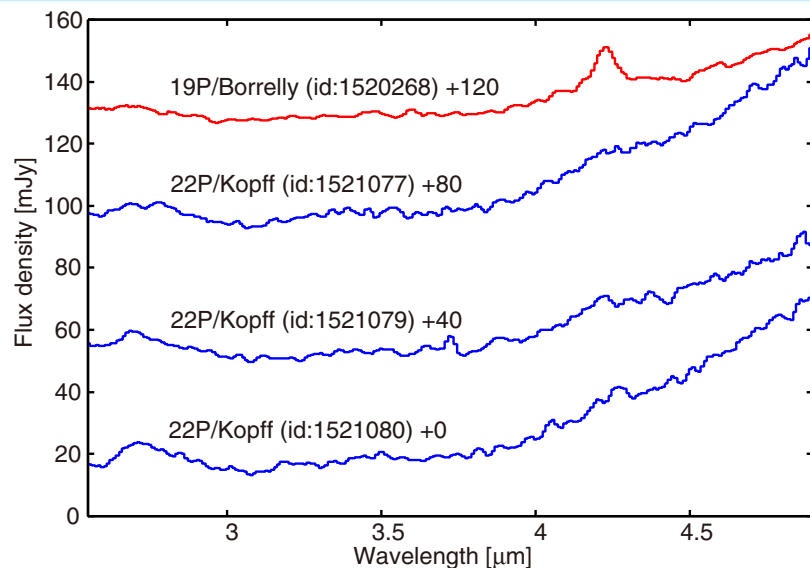


Comet observations



Object	UT Date	ObsID ^a	r_h^b (AU)	Δ^c (AU)	Aperture Width (arcsec)	Flux (H ₂ O) ^d ($\times 10^{-16}$ W m ⁻²)	Flux (CO ₂) ^e ($\times 10^{-16}$ W m ⁻²)	Flux (CO) ^f ($\times 10^{-16}$ W m ⁻²)
19P/Borrelly	2008 Dec 30.08	1520268	2.19	1.95	29.2	2.61 ± 0.08	3.80 ± 0.06	<0.27
22P/Kopff	2009 Apr 22.57	1520241	1.61	1.26	46.7	24.60 ± 0.20	29.06 ± 0.08	<0.45
22P/Kopff	2009 Apr 22.63	1520242	1.61	1.26	56.9	82.76 ± 0.44	90.50 ± 0.24	<1.05
22P/Kopff	2009 Dec 11.18	1521077	2.42	2.22	51.1	5.00 ± 0.13	3.23 ± 0.09	<0.49
22P/Kopff	2009 Dec 11.45	1521079	2.43	2.22	43.8	3.99 ± 0.13	1.64 ± 0.09	<0.46
22P/Kopff	2009 Dec 11.52	1521080	2.43	2.22	51.1	6.96 ± 0.12	1.69 ± 0.09	<0.46
29P/Schwassmann-Wachmann 1	2009 Nov 18.49	1521081	6.18	6.09	43.8	2.07 ± 0.13	<0.69	4.58 ± 0.14
29P/Schwassmann-Wachmann 1	2009 Nov 18.56	1521083	6.18	6.09	51.1	2.61 ± 0.14	<0.64	5.79 ± 0.15
64P/Swift-Gehrels	2009 Nov 23.09	1521099	2.27	2.05	36.5	2.17 ± 0.10	3.40 ± 0.08	<0.60
64P/Swift-Gehrels	2009 Nov 23.16	1521101	2.27	2.05	43.8	3.12 ± 0.11	4.05 ± 0.08	<0.62
67P/Churyumov-Gerasimenko	2008 Nov 02.38	1520244	1.84	1.56	58.4	5.77 ± 0.11	2.40 ± 0.09	<0.57
81P/Wild 2	2009 Dec 14.10	1521107	1.74	1.44	43.8	48.79 ± 0.43	49.11 ± 0.15	<0.69
81P/Wild 2	2009 Dec 14.16	1521109	1.74	1.44	43.8	71.31 ± 0.34	49.93 ± 0.17	<0.96
81P/Wild 2	2009 Dec 14.50	1521110	1.74	1.43	49.6	61.58 ± 0.40	52.16 ± 0.17	<1.03
88P/Howell	2009 Jul 03.06	5200913	1.74	1.41	29.2	25.57 ± 0.20	35.43 ± 0.10	<0.47
88P/Howell	2009 Jul 03.13	5200914	1.73	1.41	45.3	33.73 ± 0.24	51.09 ± 0.14	<1.22
116P/Wild 4	2009 May 15.60	1520245	2.22	1.98	43.8	5.53 ± 0.13	3.30 ± 0.08	<0.50
116P/Wild 4	2009 May 16.49	1520246	2.22	1.99	48.2	8.02 ± 0.13	2.64 ± 0.09	<0.51
118P/Shoemaker-Levy 4	2009 Sep 08.71	1520247	2.18	1.93	16.1	4.16 ± 0.08	3.59 ± 0.06	<0.33
118P/Shoemaker-Levy 4	2009 Sep 08.78	1520248	2.18	1.93	21.9	3.52 ± 0.09	5.99 ± 0.07	<0.37
144P/Kushida	2009 Apr 18.48	1520249	1.70	1.37	58.4	44.85 ± 0.30	39.51 ± 0.12	<0.62
144P/Kushida	2009 Apr 18.55	1520250	1.70	1.37	54.0	38.41 ± 0.28	35.15 ± 0.12	<0.75
157P/Tritton	2009 Dec 30.13	1521128	1.48	1.11	43.8	7.16 ± 0.13	2.90 ± 0.09	<0.47
157P/Tritton	2009 Dec 30.27	1521131	1.48	1.11	36.5	5.16 ± 0.12	2.97 ± 0.09	<0.53
C/2006 OF2 (Broughton)	2008 Sep 16.72	1520252	2.43	2.21	58.4	26.74 ± 0.24	36.02 ± 0.10	<0.50
C/2006 OF2 (Broughton)	2009 Mar 28.07	1520271	3.20	3.04	46.7	3.26 ± 0.15	11.01 ± 0.09	<0.38
C/2006 Q1 (McNaught)	2008 Jun 03.59	1520254	2.78	2.59	36.5	8.89 ± 0.14	22.82 ± 0.08	<0.39
C/2006 Q1 (McNaught)	2009 Feb 23.76	1520273	3.64	3.50	43.8	1.55 ± 0.11	4.60 ± 0.08	<0.32
C/2006 W3 (Christensen)	2008 Dec 21.07	1520256	3.66	3.52	51.1	11.82 ± 0.29	69.72 ± 0.16	20.95 ± 0.18
C/2006 W3 (Christensen)	2009 Jun 16.75	5200910	3.13	2.96	43.8	39.71 ± 0.49	96.65 ± 0.23	19.86 ± 0.23
C/2007 G1 (LINEAR)	2008 Aug 20.23	1520258	2.80	2.62	29.2	3.90 ± 0.09	5.06 ± 0.06	<0.29
C/2007 N3 (Lulin)	2009 Feb 05.57	1520260	1.28	0.80	43.8	1139.0 ± 6.87	782.10 ± 2.02	<10.6
C/2007 N3 (Lulin)	2009 Mar 30.67	5200708	1.70	1.36	56.9	266.50 ± 1.40	158.20 ± 0.34	<1.54
C/2007 Q3 (Siding Spring)	2009 Mar 03.27	1520261	3.29	3.14	43.8	6.89 ± 0.13	6.94 ± 0.08	<0.30
C/2008 Q3 (Garradd)	2009 Jul 05.60	5200917	1.81	1.48	24.8	73.17 ± 0.44	115.90 ± 0.25	10.90 ± 0.22
C/2008 Q3 (Garradd)	2009 Jul 06.49	5200916	1.81	1.50	26.3	79.73 ± 0.47	113.20 ± 0.24	10.48 ± 0.22
C/2008 Q3 (Garradd)	2010 Jan 03.14	1521055	2.96	2.78	36.5	1.45 ± 0.11	5.38 ± 0.09	<0.36

Observation results

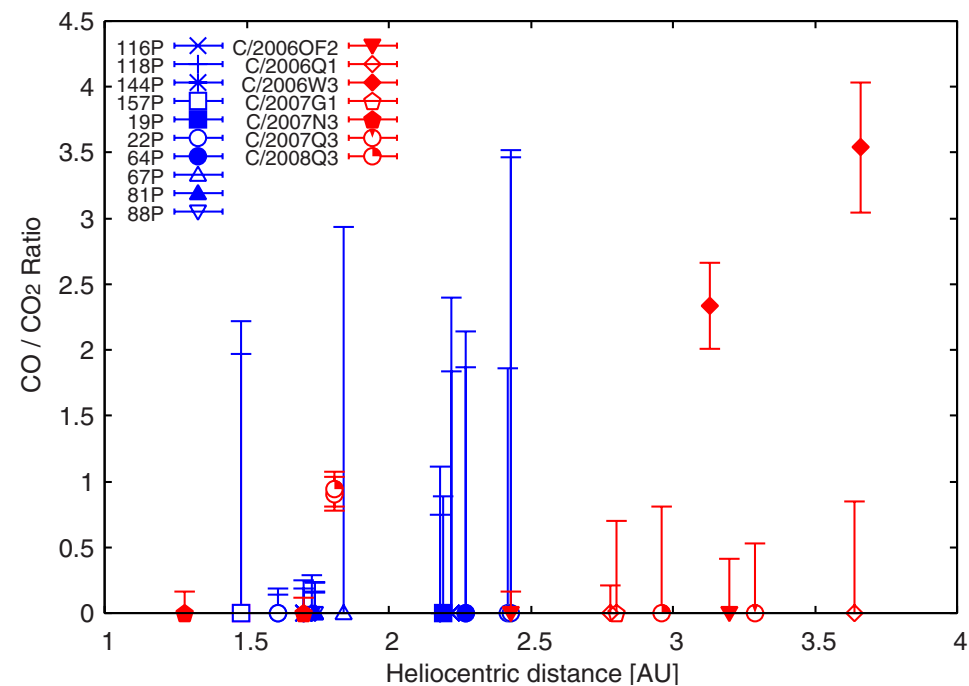
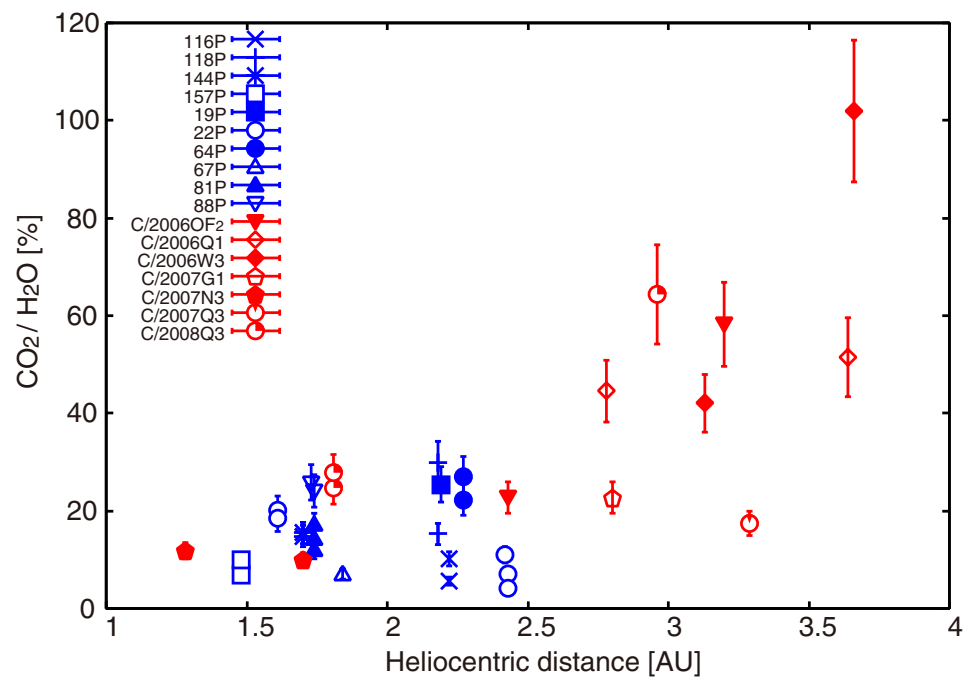


Derived gas production rate



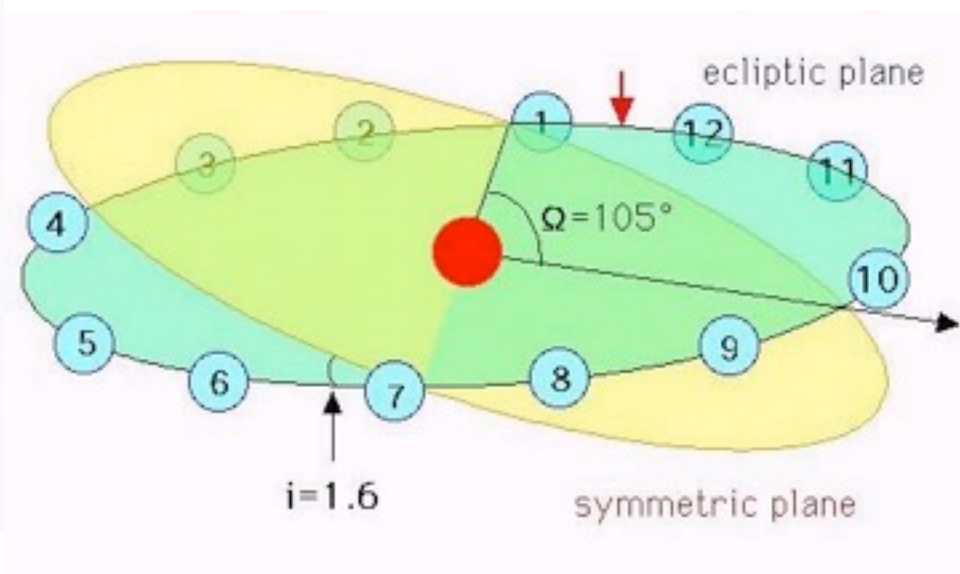
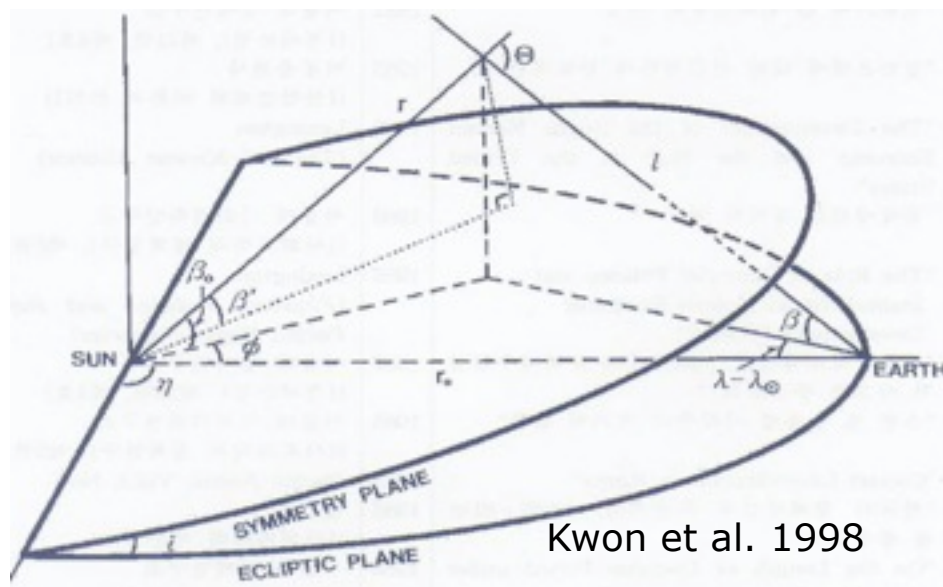
Object	ObsID ^a	r_h^b (AU)	$Q(\text{H}_2\text{O})$ ($\times 10^{26}$ molecules s^{-1}) ^c	$Q(\text{CO}_2)$ ($\times 10^{26}$ molecules s^{-1}) ^d	$Q(\text{CO})$ ($\times 10^{26}$ molecules s^{-1}) ^e
19P/Borrelly	1520268	2.19	6.38 ± 0.67	1.62 ± 0.16	<1.55
22P/Kopff	1520241	1.61	19.31 ± 1.94	3.89 ± 0.39	<0.79
22P/Kopff	1520242	1.61	59.39 ± 5.95	10.96 ± 1.10	<1.65
22P/Kopff	1521077	2.42	12.15 ± 1.26	1.34 ± 0.14	<2.66
22P/Kopff	1521079	2.43	10.48 ± 1.10	0.74 ± 0.08	<2.70
22P/Kopff	1521080	2.43	16.99 ± 1.72	0.70 ± 0.08	<2.53
29P/Schwassmann-Wachmann 1	1521081	6.18	57.79 ± 6.79	<3.77	269.1 ± 28.15
29P/Schwassmann-Wachmann 1	1521083	6.18	67.75 ± 7.63	<3.22	313.9 ± 32.42
64P/Swift-Gehrels	1521099	2.27	5.23 ± 0.58	1.41 ± 0.14	<3.25
64P/Swift-Gehrels	1521101	2.27	6.85 ± 0.72	1.52 ± 0.16	<3.07
67P/Churyumov-Gerasimenko	1520244	1.84	6.20 ± 0.63	0.43 ± 0.05	<1.35
81P/Wild 2	1521107	1.74	50.83 ± 5.10	8.73 ± 0.87	<1.60
81P/Wild 2	1521109	1.74	74.29 ± 7.44	8.87 ± 0.89	<2.25
81P/Wild 2	1521110	1.74	60.02 ± 6.01	8.63 ± 0.86	<2.24
88P/Howell	5200913	1.74	32.09 ± 3.22	7.73 ± 0.77	<1.35
88P/Howell	5200914	1.73	33.51 ± 3.36	8.65 ± 0.87	<2.72
116P/Wild 4	1520245	2.22	11.33 ± 1.17	1.16 ± 0.12	<2.28
116P/Wild 4	1520246	2.22	15.82 ± 1.60	0.89 ± 0.09	<2.26
118P/Shoemaker-Levy 4	1520247	2.18	14.25 ± 1.45	2.18 ± 0.22	<2.62
118P/Shoemaker-Levy 4	1520248	2.18	9.97 ± 1.03	2.99 ± 0.30	<2.42
144P/Kushida	1520249	1.70	37.55 ± 3.76	5.57 ± 0.56	<1.14
144P/Kushida	1520250	1.70	33.29 ± 3.34	5.15 ± 0.52	<1.43
157P/Tritton	1521128	1.48	4.50 ± 0.46	0.31 ± 0.03	<0.65
157P/Tritton	1521131	1.48	3.55 ± 0.36	0.35 ± 0.04	<0.82
C/2006 OF2 (Broughton)	1520252	2.43	61.22 ± 6.15	13.97 ± 1.40	<2.52
C/2006 OF2 (Broughton)	1520271	3.20	16.99 ± 1.86	9.90 ± 0.99	<4.46
C/2006 Q1 (McNaught)	1520254	2.78	36.33 ± 3.68	16.19 ± 1.62	<3.67
C/2006 Q1 (McNaught)	1520273	3.64	11.57 ± 1.40	5.96 ± 0.60	<5.48
C/2006 W3 (Christensen)	1520256	3.66	82.96 ± 8.55	84.59 ± 8.46	299.3 ± 30.0
C/2006 W3 (Christensen)	5200910	3.13	201.0 ± 20.3	84.66 ± 8.47	197.7 ± 19.9
C/2007 G1 (LINEAR)	1520258	2.80	18.37 ± 1.89	4.17 ± 0.42	<3.19
C/2007 N3 (Lulin)	1520260	1.28	409.1 ± 40.9	48.48 ± 4.85	<8.67
C/2007 N3 (Lulin)	5200708	1.70	223.8 ± 22.4	22.42 ± 2.24	<2.86
C/2007 Q3 (Siding Spring)	1520261	3.29	39.80 ± 4.05	6.95 ± 0.70	<3.97
C/2008 Q3 (Garradd)	5200917	1.81	112.0 ± 11.2	31.04 ± 3.11	29.30 ± 3.02
C/2008 Q3 (Garradd)	5200916	1.81	119.8 ± 12.0	29.66 ± 2.97	26.84 ± 2.77
C/2008 Q3 (Garradd)	1521055	2.96	6.99 ± 0.87	4.50 ± 0.46	<3.93

Derived gas production rate



Modeling the InterPlanetary Dust(IPD) Cloud

SYMMETRY PLANE \neq ECLIPTIC PLANE



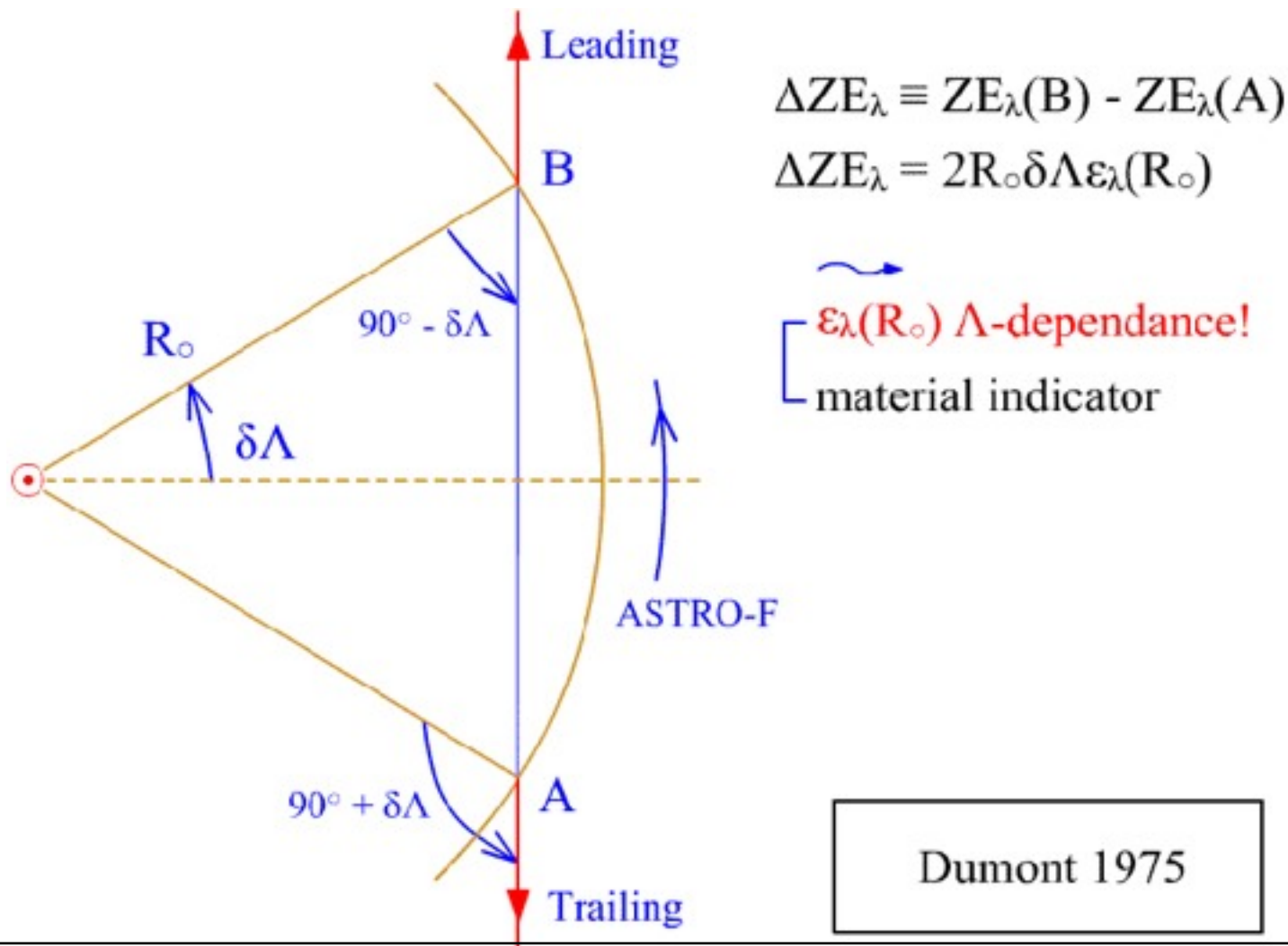
longitude of ascending node, Ω ; inclination angle, i

Sun \neq IPD cloud center, amount of off-centering ΔX and ΔY

(Kelsall et al. 1998)

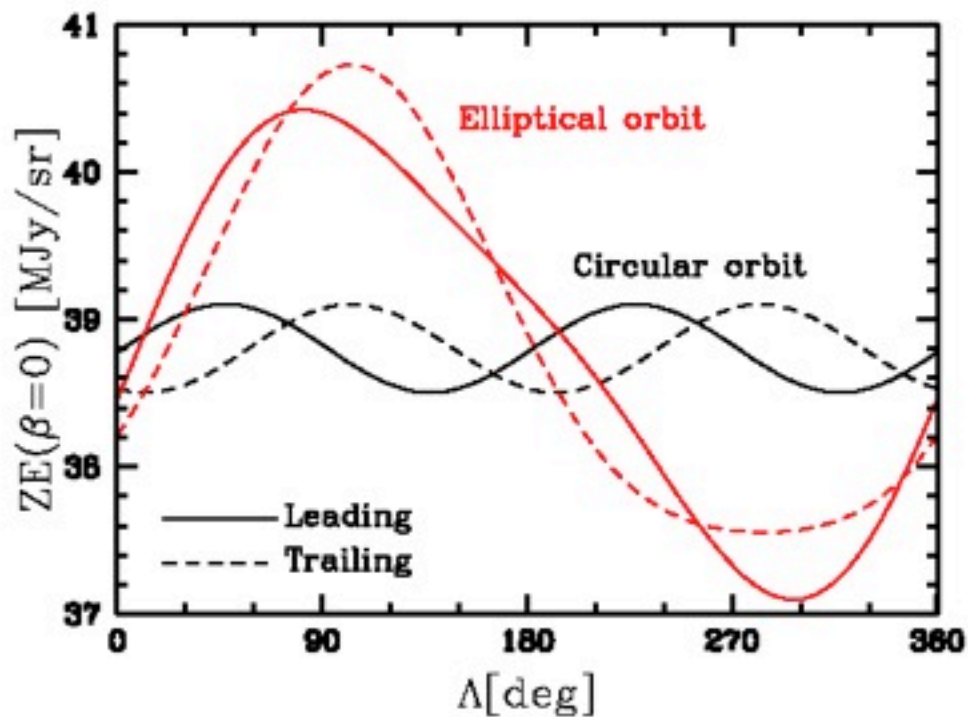


Mean Volume Emissivity Near the Earth's Orbit

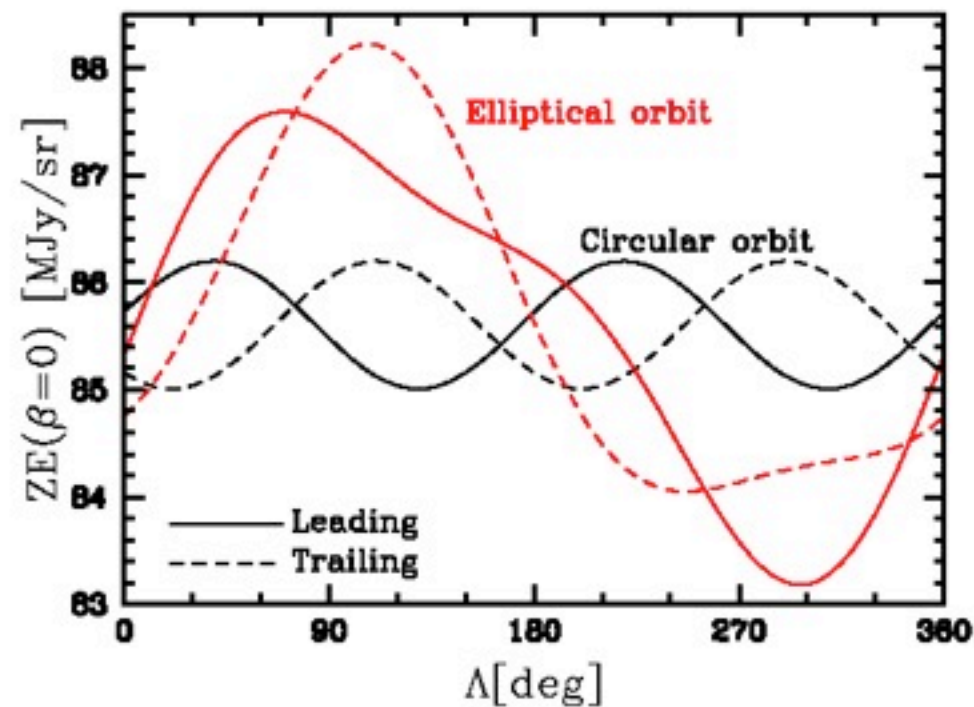


$\epsilon = 91^\circ, 89^\circ, 90^\circ$ 12+ α season \rightarrow 248 pointings

Seasonal modulation

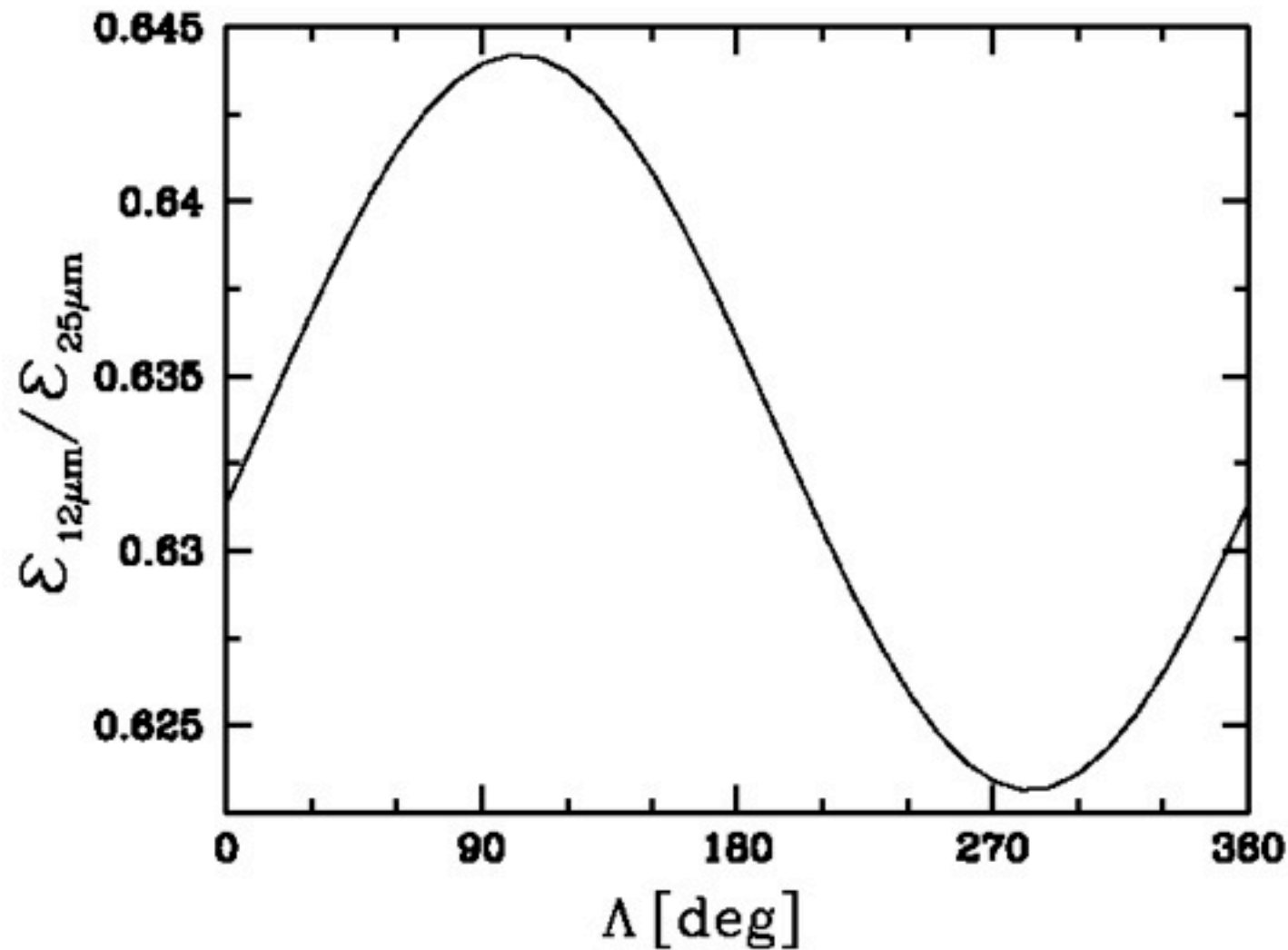


(a) wavelength $\lambda = 12 \mu\text{m}$



(b) wavelength $\lambda = 25 \mu\text{m}$

Seasonal modulation on 12/25 color



Modeling the InterPlanetary Dust(IPD) Cloud



From the AKARI mid-infrared All-Sky Survey, we have constructed the brightness maps of the zodiacal emission light over the entire sky.

Maps enable us to locate the maximum IPD density plane with respect to the ecliptic, and reveal new features from the diffuse, broken bands discovered earlier by IRAS.

In constructing the three-dimensional model of the IPD cloud, the mean volume cross-section and temperature of the local IPDs play a pivotal role; yet, these parameters are measured for the first time by the AKARI's pointing observations.

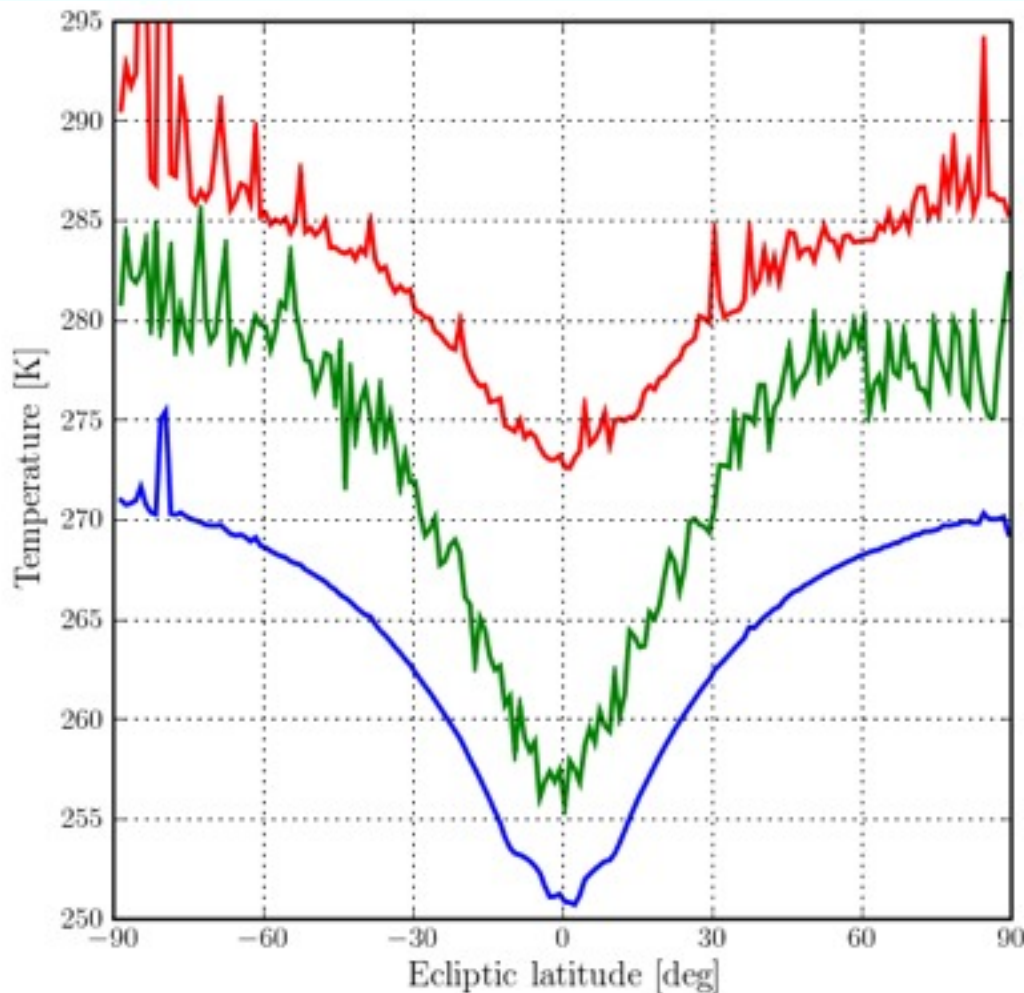
Constructed brightness maps of the zodiacal emission at 9 and 18 μm , from the AKARI All-Sky Survey, and applied the Fourier filtering to the maps. Although the original map has limited resolution, after having been filtered, they clearly confirm the dust bands already discovered by the IRAS and display new band features as well. As regards to the band pair lying around $\beta = \pm 17^\circ$, Espy et al. (2009) paid special attention to gaps appeared in the IRAS filtered maps in some longitude intervals and took the gaps as an evidence of the pair's genetic relation to Emilkowalski cluster of asteroids and its extremely youthfulness in dynamical evolution. An incomplete longitude coverage of the IRAS might have misled us to believe the gap as a real feature. In our filtered maps, however, the band pair extends over the whole longitude circle. The full longitude coverage of the AKARI survey is of great importance in future dynamical studies of diffuse, broken bands.

S.S.Hong et.al., ASPC 2009

J.H.Pyo et.al., ASPC 2009



COLOR PROFILE OF ZE OVER LATITUDE Beta



COBE/ DIRBE

4.9um - 12um

AKARI/ IRC

9um - 18um

COBE/ DIRBE

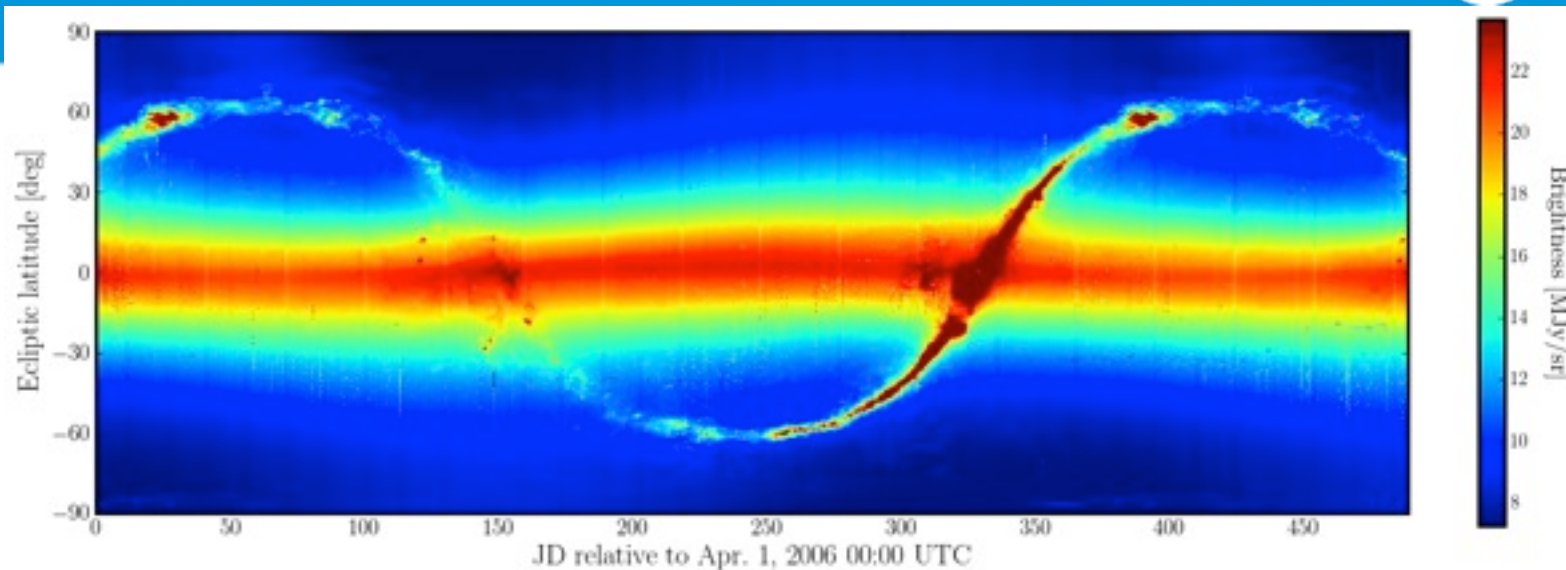
12um - 25um



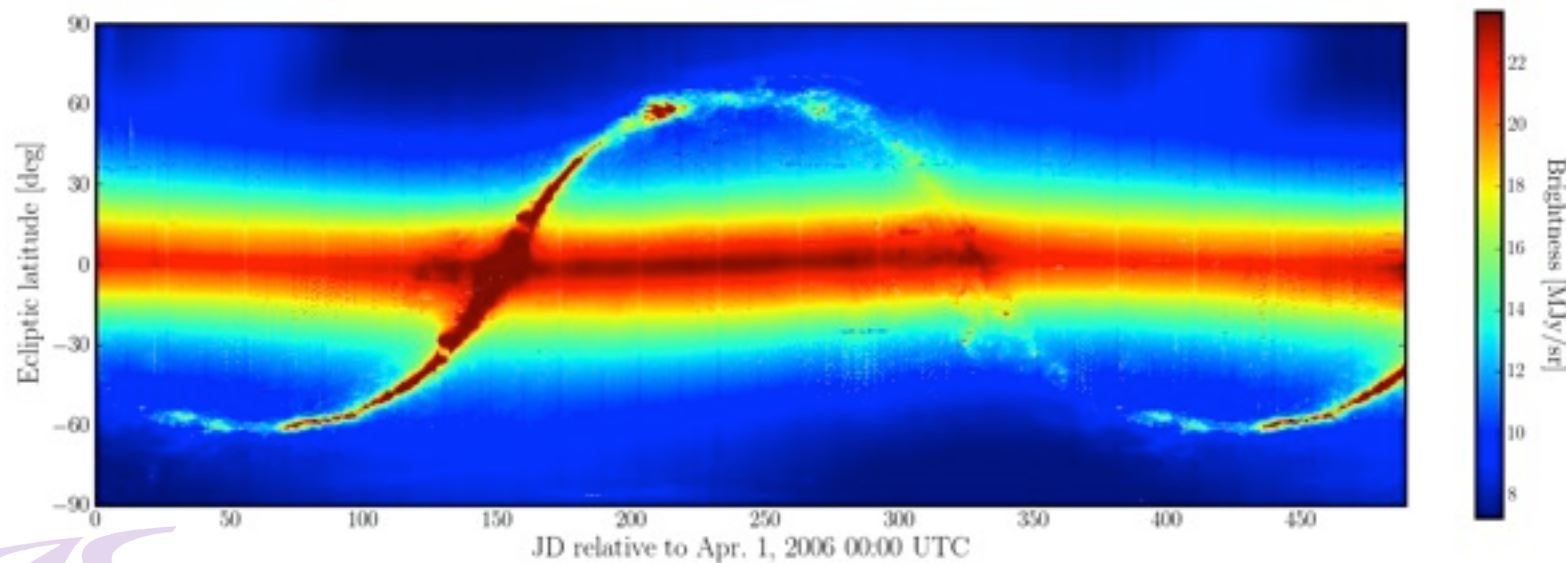
*Can we understand the beta-dependence of
color temperature with the single component model ?*



The Sky Observed by AKARI S9W-band



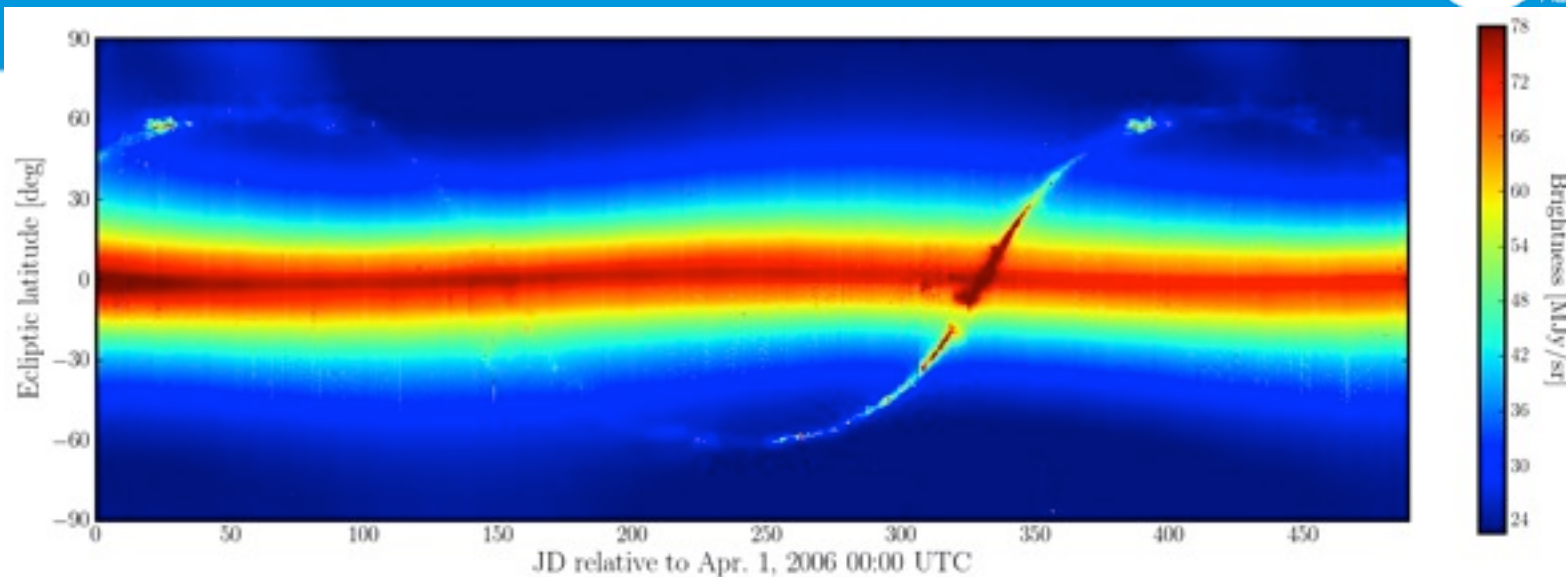
Leading direction



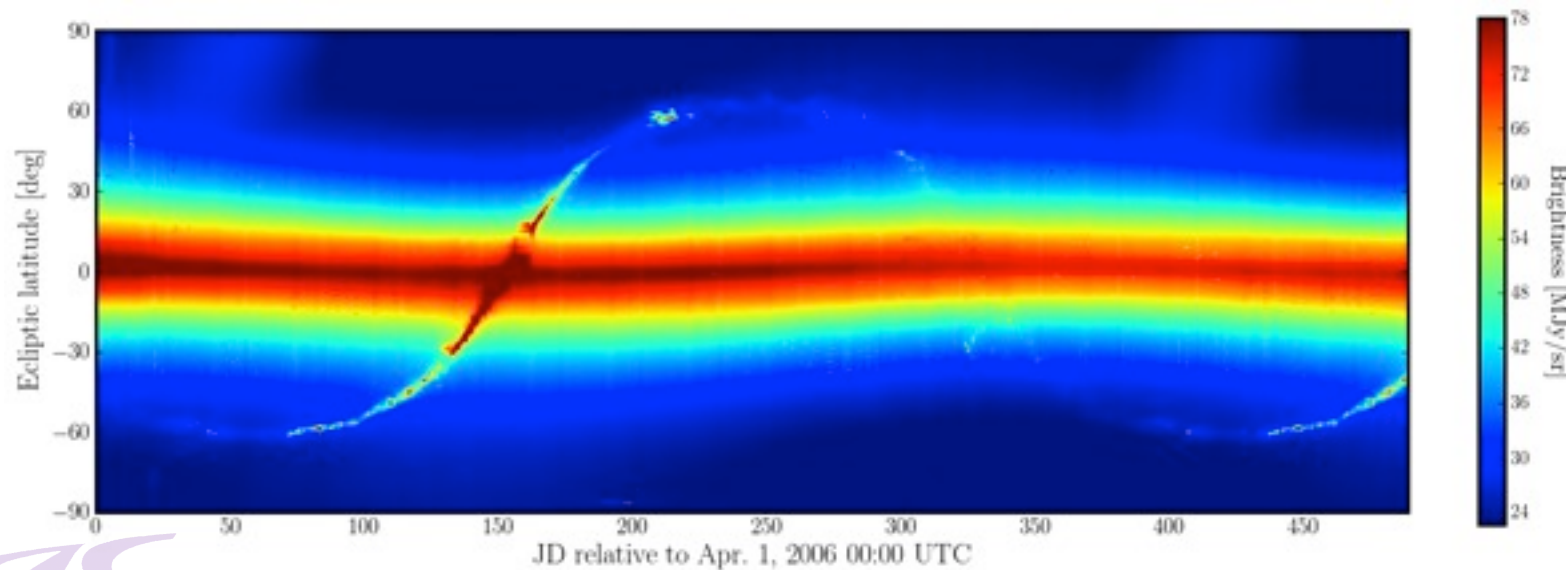
Trailing direction



The Sky Observed by AKARI L18W-band



Leading direction



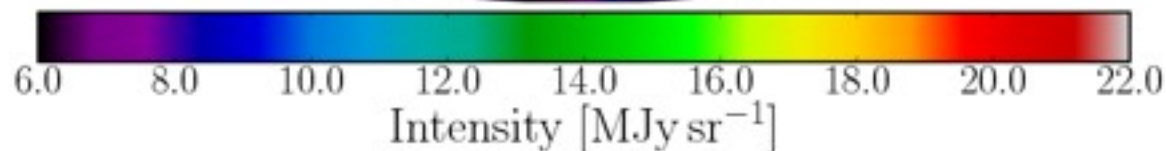
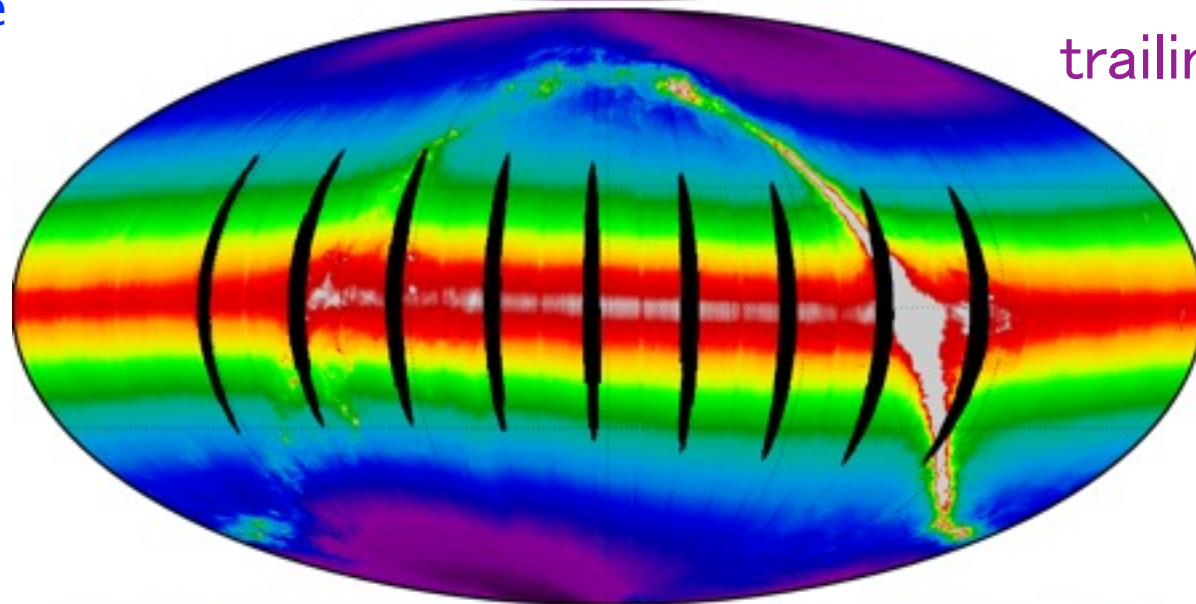
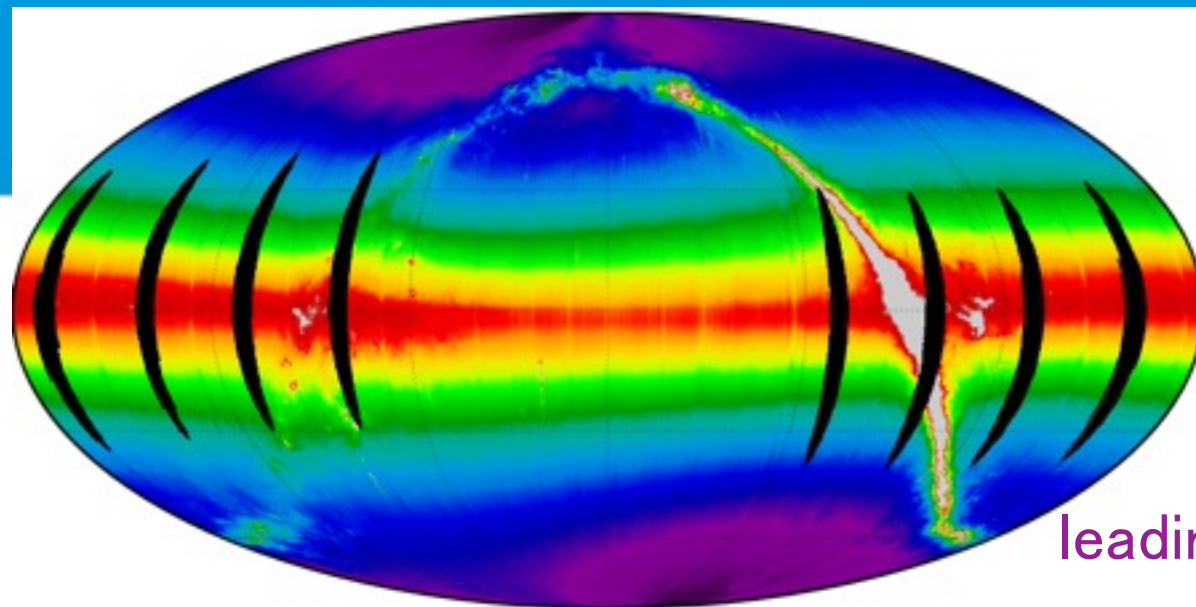
Trailing direction



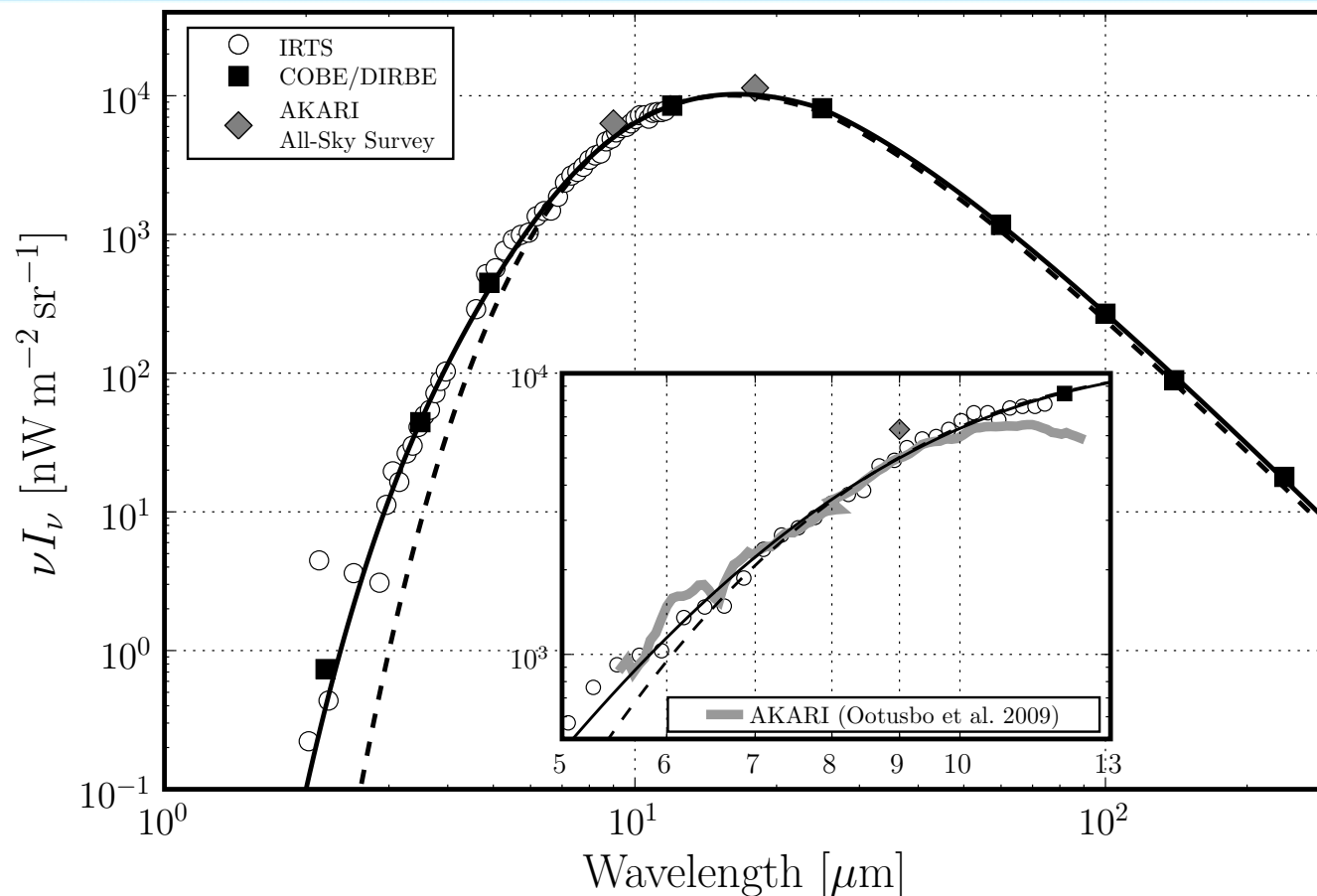
ZE brightness map at 9 μm

Max. brightness latitude is
fluctuating.

← Obliquity of symmetry plane
w.r.t. the ecliptic

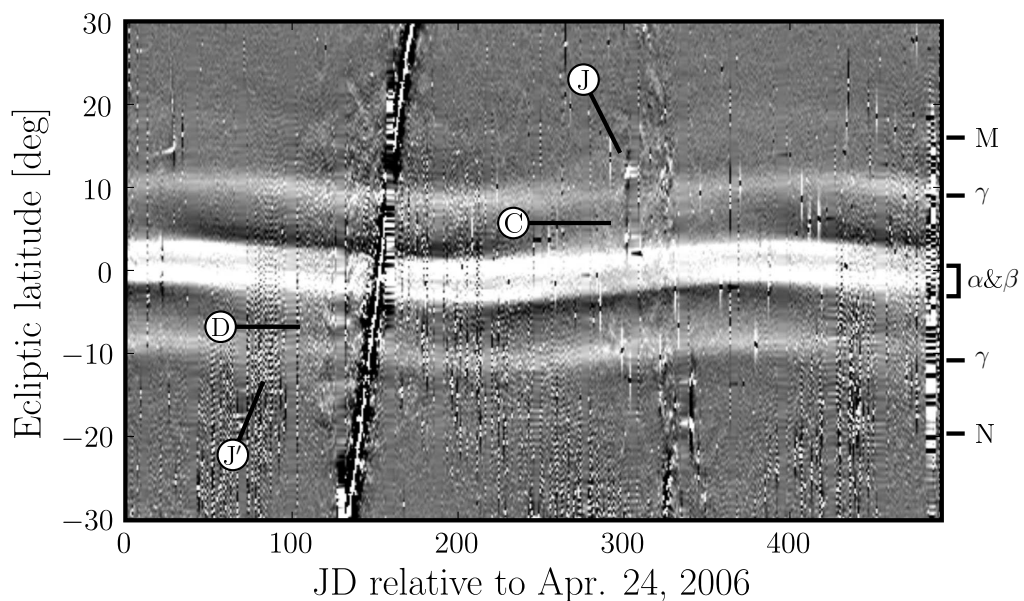
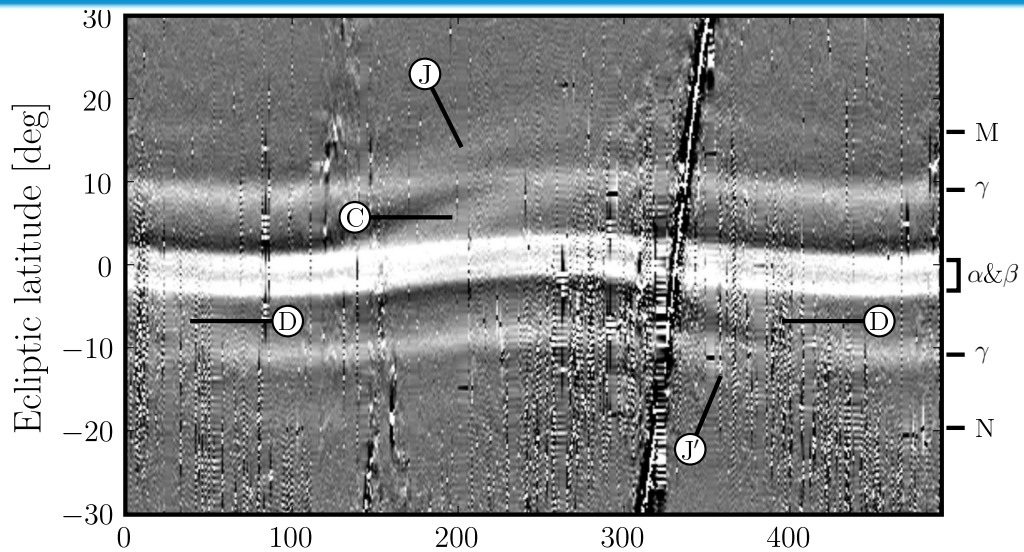


Observed SED of IPD cloud



The observed SED of ZE is compared with calculations of single (dashed line) and double (solid line) component model of IPDs. For both components of the IPDs, density and temperature exponents are kept the same, but the reference temperature is left as model parameter. Near infrared part of the SED is dominated by the hotter component of IPDs.

Asteroidal dust bands near the ecliptic plane



Brightness map of the zodiacal emission from the AKARI IRC All-Sky Survey



In the preprocessed data of the AKARI IRC All-Sky Survey, we have identified instrumental features that require further corrections to the data: detector's after-effect caused by exposure to bright Moon light and the Earthshine scattered into the telescope beam. The all-sky brightness maps exhibit smooth distribution of the ZE brightness with the wobbling of the symmetry plane and the leading-trailing asymmetry of the ecliptic plane brightness. The asymmetry between leading- and trailing-direction brightness is compared with the IPD cloud model of Kelsall et al. (1998) to derive the emissivity modification factors at $9\ \mu\text{m}$ for the smooth cloud, the dust bands, and the MMR components in the model. The factors for the cloud and band components are comparable to those at $12\ \mu\text{m}$, but one for the ring is about 20% higher than the values at $4.9\ \mu\text{m}$ and $12\ \mu\text{m}$. This implies that the contribution of the MMR component to the ZE brightness is underestimated in Kelsall's model. Furthermore, AKARI's monitoring of the brightness at the ecliptic poles has located the plane of maximum IPD density with respect to the ecliptic plane. We modified the plane's inclination and longitude of ascending node for the smooth cloud model of Kelsall et al. (1998) to best fit the observed variation of the pole ZE brightness difference. The resulting values are slightly different from the original model, which suggests a possible warping of the IPD cloud.



Residual brightness maps of IPD cloud

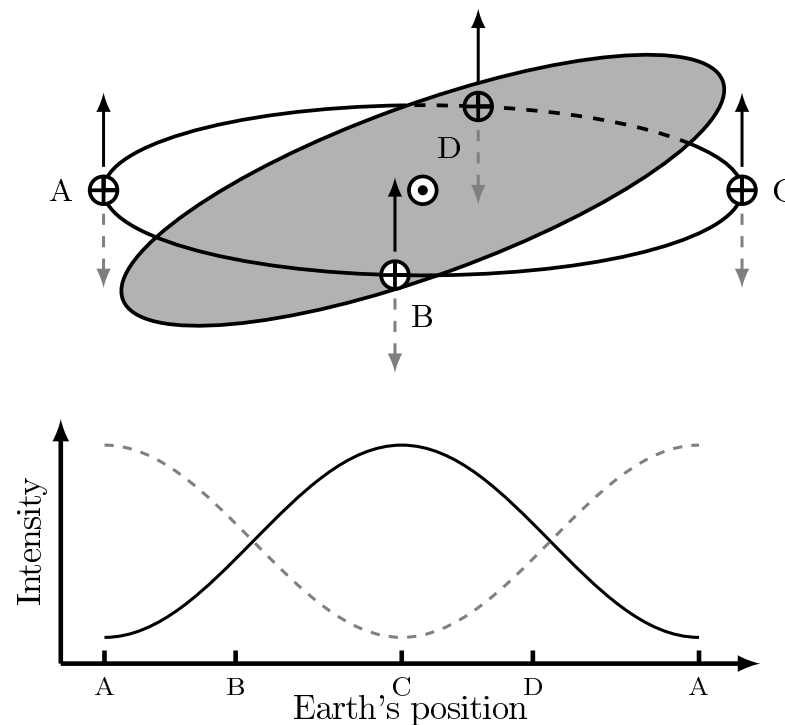
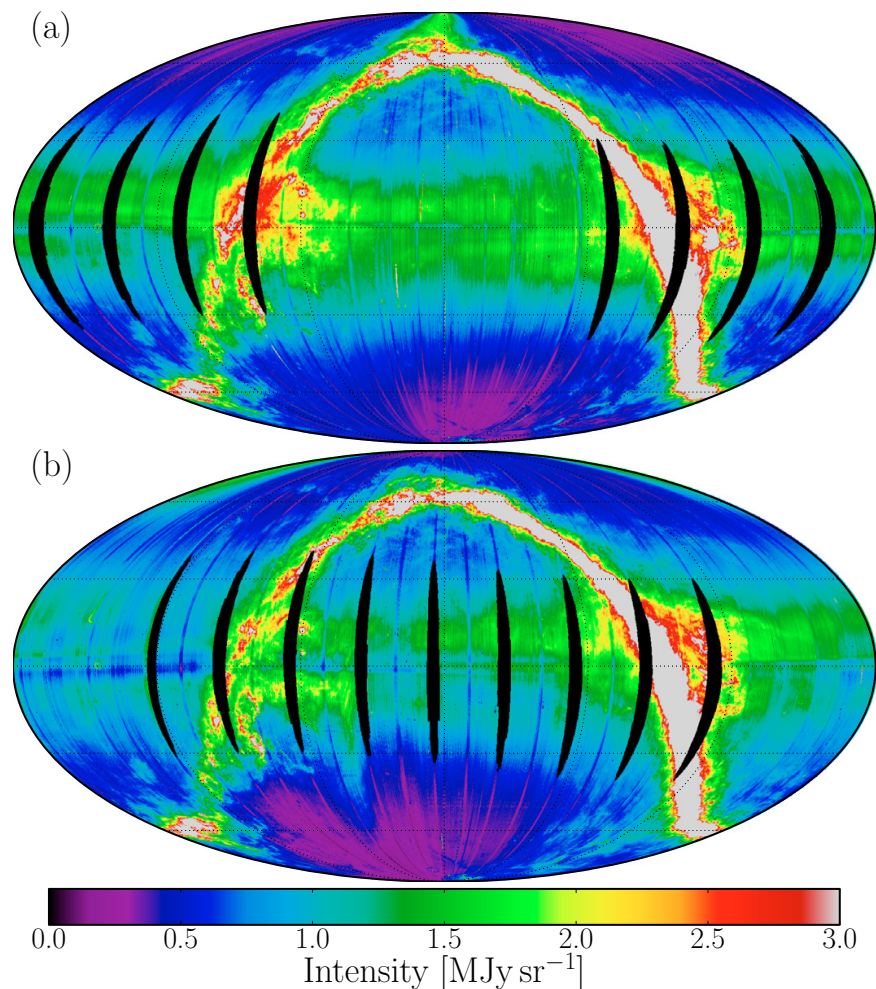


Fig. 5. Schematic diagram for the seasonal variation of NEP and SEP brightness due to tilt of the IPD cloud's symmetry plane. The Earth's positions marked by A, B, C, and D on the top frame correspond to the abscissas labeled by the same characters. In the top frame, the upward arrows point to the NEP while the downward ones point to the SEP. The NEP and SEP intensities are represented by a black, solid line and a gray, broken line, respectively, in the bottom frame.

Residual brightness maps in the leading a) and the trailing b) directions, after the brightness due to the Kelsall et al. (1998) IPD cloud model has been subtracted from the AKARI observation.

Derived parameters

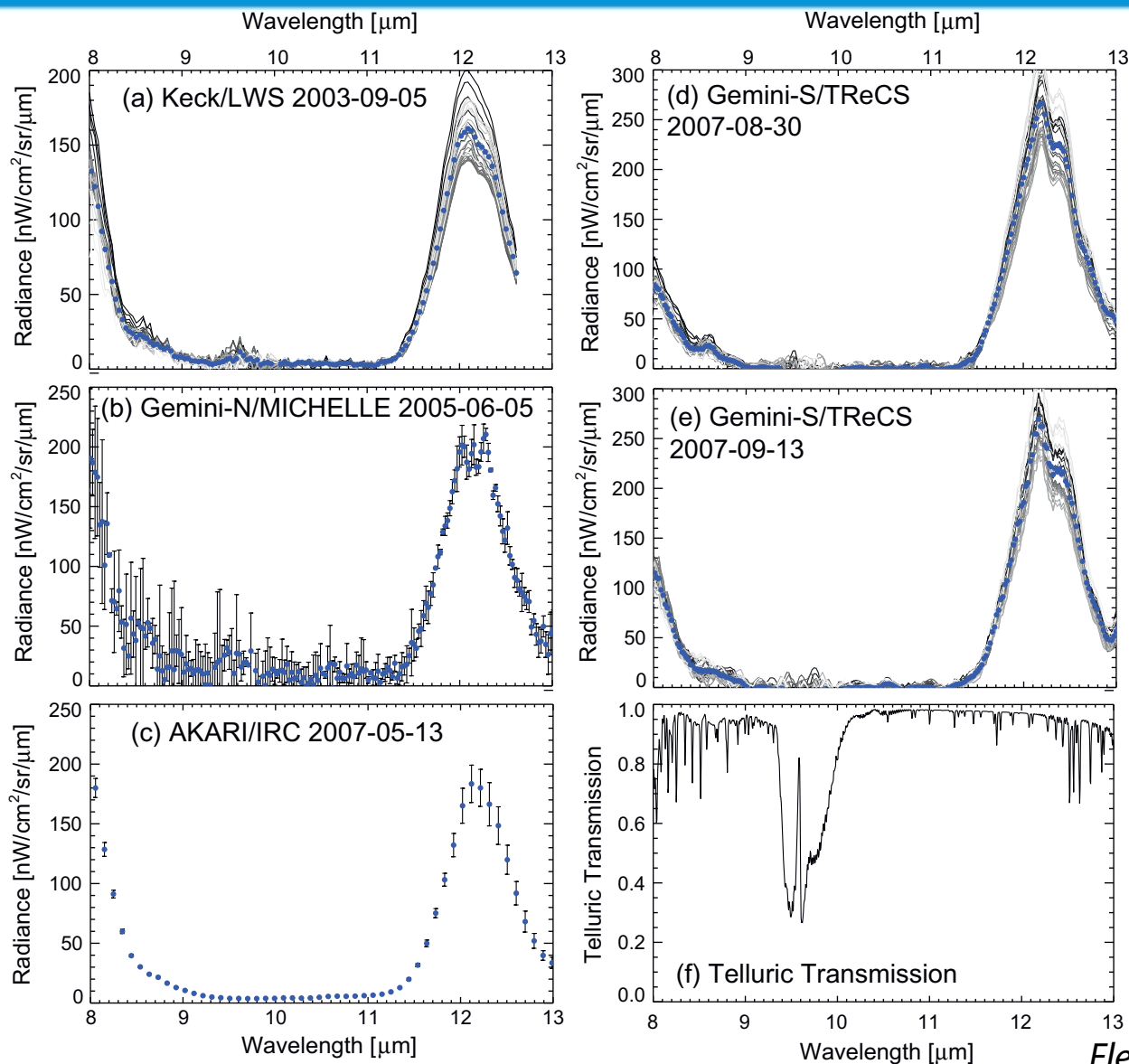
Table 2. Symmetry plane parameters.

Parameter	Kelsall et al. (1998)	This work
Inclination [°]	2.03 ± 0.017	2.29 ± 0.36
Ascending node [°]	77.7 ± 0.6	74.491 ± 0.012

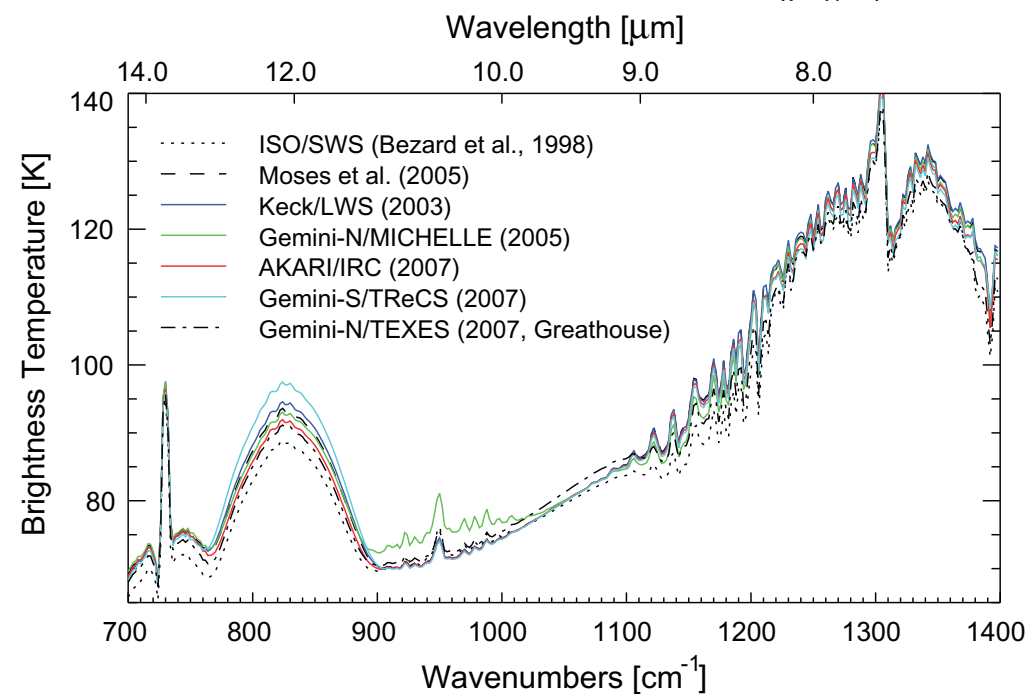
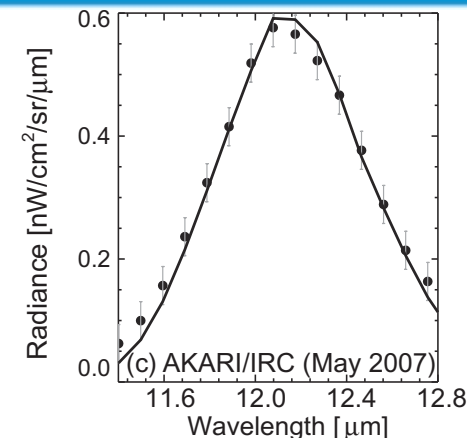
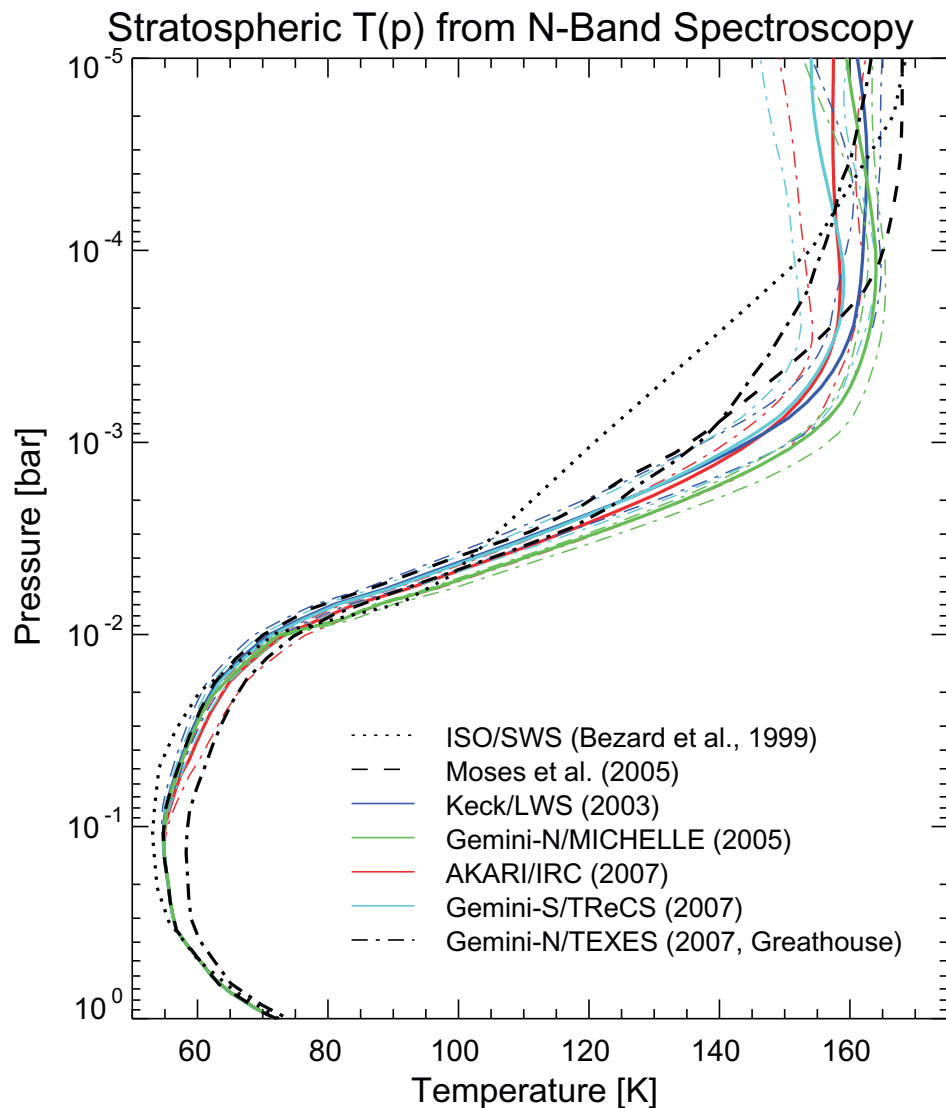
Table 3. Longitude of the maximum average pole brightness.

Observation	Wavelength	Longitude
IRAS ZOHF ^a	12 μm	116.4 ± 2.1
	25 μm	123.6 ± 2.6
COBE/DIRB ^b	12 μm	$\sim 44^\circ$
	25 μm	$\sim 44^\circ$
AKARI ^c	9 μm	65.2 ± 0.5
Model ^d	9 μm	93.5

Neptune at summer solstice: Zonal mean temperatures from ground-based observations, 2003–2007



Neptune at summer solstice: Zonal mean temperatures from ground-based observations, 2003–2007



あかりで目指したサイエンスは？



● 星形成領域の観測

● 原始惑星系円盤におけるダストディスク消失のタイムスケール

● 未だ、まとまった結果になっていない

● 課題：検出限界が、想定よりも悪かった。

● WTTS については、優位に存在頻度が低いことがこれまでの解析で見えている

● 解析体制の脆弱さ

● 現状のレベルでまとめておくべき

● あかり と WISE の結果を合わせて進めるべき

● 原始惑星系円盤における、ダストの進化

● もう少しひねり出せるでしょう

● 多様な星形成プロセスの観測的研究

● ほとんどのデータが隠れている(かなり生産性の高いデータ)：高品質アトラス

● WISE の観測結果と拮抗する部分が多い



あかりで目指したサイエンスは？



● 太陽系天体

● 惑星間塵

● 起源, 空間分布・構造, 軌道進化, Composition, COBE-DIRBE モデルからの脱却

● IRAS を凌駕する結果には到っていない

● 本質的には、IRAS よりも高感度・高空間分解能だったはず

● 惑星間塵の大局的構造に加えて、微細構造の観測では圧倒的に有利だったはず

● IRAS で見えていた物すら、未だ十分に見えていないものがある。 **なんでや!**

● 解析レベルの未熟さ

● 小惑星

● 含水鉱物という切り口で、将来につながる成果が見えてきている

● 彗星

● ダスト組成、Crystalline silicate はどこから？

● これも将来につながる成果が見えてきている



Number of Refereed Papers



Satellite	Objective	Start of Operation	End of Operation	Counting Period	Number
AKATSUKI	Venus Atmospheric Obs.	2010	operating	2011-2012	8
KAGUYA	Lunar Exploration	2007	2009	2008-2012	190
HINODE	Solar Obs.	2006	operating	2007-2012	844
AKARI	Infrared Astronomical Obs.	2006	2011	2007-2012	222
SUZAKU	X-ray Astronomical Obs.	2005	operating	2006-2012	681
HAYABUSA	Asteroid Sample Return	2003	2010	2004-2012	129
NOZOMI	Mars Scientific Obs.	1998	2003	1999-2012	26
HALCA	Space VLBI	1997	2005	1998-2012	44
ASCA	X-ray Astronomical Obs.	1993	2002	1994-2012	2287
GEOTAIL	Geo-Magnetospheric Obs.	1992	operating	1993-2012	1236
YOHKOH	Solar Obs.	1991	2000	1992-2012	1089
<reference>					
Subaru Telescope	The Ground based optical&infrared Observatory	1999	operating	2000-2012	1031

課題・反省事項



- 観測モードの多さ
 - 各観測モードの使用実績が相対的に少なくなる
 - 各モードのキャリブレーションやデータの取り扱いに関する知見蓄積が不足

- 打ち上げ前の装置の完成度の不十分さ
 - 長波長側で達成された感度は、ミッション提案時と比較すると大幅に低かった
 - 一部の機能の評価が不十分なままフライトに持ち込まざるを得なかった
 - (開発体制を超えたミッションであった)
 - 試験検証からハードウェアへのフィードバックができる余裕は無かった
- 望遠鏡を含めたシステムとしてのミッション部について、事前検討が不十分であった
 - 想定外の回折光 (打ち上げ時の想定外の事象もあったが)
 - 運用上の制限が打ち上げ前の想定よりも大きかった：IPD の一部の観測では厳しく



教訓



- 開発体制に対して最適なミッション規模・複雑さの見極めの重要性
 - やはりミッションはシンプルなものとするべし
 - 海外ミッション (例：IRAS, SST, WISE) と比較して、圧倒的に多機能、多モード
 - ミッションシナリオを含めた、ミッション検討の重要性
 - 科学ミッションは成果を大きく出して **なんぼ**
 - **成果の最大化に向けた、開発・運用性・データ解析・アーカイブ** の設計が必要
 - 『後の事は、打上げてから』の時代は終わっているのですよ
 - データ解析に対する体制の不十分さ
 - IRAS では 1000(人年)を超える体制が充てられた(IPACを設立)
 - あかりでは、上記の 1%オーダーレベルの極めて脆弱な体制
 - このため、プロジェクト外のメンバーの科学成果が限定的である



IRASでの解析

似たようなことは あかり でもある



● KNOWN PROCESSING ANOMALIES

- Processing of Extended ("Cirrus") Sources as Point Sources
- Instability and Lag of the Noise Estimator
- Frequency Dependence of Responsivity with Amplitude
- Errors in Cross-Scan Uncertainties Related to Failed Detectors
- Photon-Induced Responsivity Enhancement
- Artifacts in the Digital Image Data Base
- Photometric Processing
- Insufficient Specification of HCON Coverage
- Position Uncertainties
- Overestimated Weak Fluxes
- Minor Problems



あかりミッションを受けて今後の展開



太陽系天体

●惑星間塵

- 起源, 空間分布・構造, 軌道進化, Composition, COBE-DIRBE モデルからの脱却
- このテーマを目指す場合、大きなミッションである必要は無い
 - 口径 10~数10cm の望遠鏡でも観測可能な事はある(地上では難しい)
- 太陽系科学全体での重要性の評価が必要：宇宙論的な立場では意外と重要

●小惑星

- 含水鉱物という切り口で、小惑星を系統的に調べる
- 近赤外線は、ほとんどのテーマが地上と競合するが、大気中に abundant な物質を対象とした観測だけが難しい：含水鉱物などもその対象
 - あかりよりも小さなミッションで、単能の衛星でやる価値はある(可能性がある)

●彗星

- 高分散スペクトルに手を出したくなる分野であり、地上観測とも一部競合

